

Titre: Electro-Mechanical Manipulation of Mammalian Cells in Suspension
Title:

Auteur: Luke MacQueen
Author:

Date: 2010

Type: Mémoire ou thèse / Dissertation or Thesis

Référence: MacQueen, L. (2010). Electro-Mechanical Manipulation of Mammalian Cells in Suspension [Thèse de doctorat, École Polytechnique de Montréal]. PolyPublie.
Citation: <https://publications.polymtl.ca/446/>

 **Document en libre accès dans PolyPublie**
Open Access document in PolyPublie

URL de PolyPublie: <https://publications.polymtl.ca/446/>
PolyPublie URL:

Directeurs de recherche: Michael R. Wertheimer, & Michael D. Buschmann
Advisors:

Programme: Génie physique
Program:

UNIVERSITÉ DE MONTRÉAL

**ELECTRO-MECHANICAL MANIPULATION OF MAMMALIAN CELLS
IN SUSPENSION**

LUKE MACQUEEN

DÉPARTMENT DE GÉNIE PHYSIQUE

ÉCOLE POLYTECHNIQUE DE MONTRÉAL

THÈSE PRÉSENTÉE EN VUE DE L'OBTENTION

DU DIPLÔME DE PHILOSOPHIAE DOCTOR

(GÉNIE PHYSIQUE)

DÉCEMBRE 2010

UNIVERSITÉ DE MONTRÉAL

ÉCOLE POLYTECHNIQUE DE MONTRÉAL

Cette thèse intitulée:

ELECTRO-MECHANICAL MANIPULATION OF MAMMALIAN CELLS IN SUSPENSION

présentée par: MACQUEEN Luke

en vue de l'obtention du diplôme de: Philosophiae Doctor

a été dûment acceptée par le jury d'examen constitué de :

Mme. BOUDOUX Caroline, Ph. D., présidente

M. WERTHEIMER Michael, R., D. Sc. A., membre et directeur de recherche

M. BUSCHMANN Michael, Ph.D., membre et codirecteur de recherche

M. GERVAIS Thomas, Ph. D., membre

M. SIMMONS Craig, A., Ph. D., membre

DEDICATION

This thesis is dedicated to my family

ACKNOWLEDGMENTS

I would first like to thank Professor Michael Wertheimer, my Ph.D. supervisor, for his excellent guidance and encouragement throughout my time in the M.Sc. A. and Ph.D. programs at the École Polytechnique. Dr. Wertheimer introduced me to the exciting interdisciplinary research topic of biological cell- “electro-manipulation”, and he initiated meetings with Professor Michael Buschmann, thus forming the nucleus of my Ph. D program.

I also thank Professor Michael Buschmann, my Ph.D. co-supervisor, who welcomed me into his tissue-engineering laboratories, where I performed the majority of the experiments reported in this thesis. In addition to productive days in the labs, I will always remember with fondness the famous summer BBQs.

Professors Wertheimer and Buschmann have been ideal Ph. D. co-supervisors, and I have benefited greatly from their generosity and expertise.

Next, I would like to thank Dr. Mohamed Latreche, Dr. Grzegorz Czeremuszkina, and Dr. Gilles Dennler, for their help getting me started in the plasma laboratories and Mr. Yves Drolet for his outstanding technical support in the plasma laboratories.

I thank the staff at the microfabrication laboratories (LMF), in particular Dr. Souleymane Bah for training me within the LMF, often spending many hours in the process. With this training, I was able to fabricate devices, which continue to work reliably several years later.

I thank Dr. Marc Thibault for his help with the confocal imaging system and other related equipment, and for interesting scientific conversations and collaborations.

I thank Professor Olivier Guenat and Dr. Thomas Gervais for their interest in my research and for their encouragement.

I have also benefitted greatly from many other people at the École Polytechnique de Montréal during my M.Sc. and Ph.D. programs, and I am very grateful to them all.

RÉSUMÉ

Le but principal de cette thèse était de décrire le développement d'une plate-forme microfabriquée et son application pour la caractérisation mécanique des cellules mammifères vivantes. La technique emploie les forces de polarisation électriques pour emprisonner et étirer des cellules dans des champs électriques non-uniformes et variables dans le temps. Ce travail a été motivé par la sous-utilisation apparente des champs électriques pour la caractérisation mécanique des cellules; les méthodes décrites ici ont permis la caractérisation mécanique de cellules mammifères diverses et précédemment non étudiées.

La caractérisation mécanique de cellules vivantes est habituellement réalisée en sondant des structures locales près de la surface des cellules. Très peu de ces techniques appliquent des contraintes uniaxiales aux cellules entières et la comparaison des données de diverses techniques est donc difficile. Par contre, des champs électriques peuvent être employés pour exercer ces forces uniaxiales sur les cellules suspendues. La plupart des cellules mammifères adoptent une géométrie quasi-sphérique lorsque suspendues dans un milieu (aqueux) liquide; ceci simplifie à la fois la manipulation des cellules ainsi que l'interprétation des données mécaniques. Les champs électriques exercent des forces sans contact mécanique significatif entre les cellules et les structures du dispositif et peuvent donc être décrits comme un « rayon tracteur », qui peut déplacer, emprisonner, ou déformer électriquement les objets polarisables telles les cellules biologiques. En plus, les électrodes nécessaires sont facilement incorporées dans les dispositifs microfabriqués, ce qui suggère que les techniques basées sur des champs électriques seront de plus en plus utilisées.

La caractérisation mécanique des cellules par « électro-déformation » (ED) se place dans le contexte plus grand de l'électro-manipulation de cellules. Afin de mieux comprendre le comportement des cellules dans les champs électriques, nous avons commencé nos études en utilisant la diélectrophorèse (DEP) pour placer des monocytes humains (U937) dans un champ électrique non-uniforme, avant d'effectuer l'électroporation (EP) permettant la livraison de transgènes. Un ensemble d'électrodes planaires inertes microfabriquées sur un substrat de verre a été utilisé pour la DEP et l'EP. Les propriétés diélectriques des cellules ont été estimées et la modélisation (par éléments finis) des champs électriques nous a permis de prévoir le positionnement des cellules. Le point à partir duquel les impulsions électriques ont augmenté la perméabilité des membranes cellulaires aux molécules fluorescentes et aux plasmides d'ADN

dépend du positionnement antérieur par DEP. Pour un ensemble donné de paramètres d'impulsion, l'EP était soit irréversible (ayant pour résultat la cytolyse), réversible (menant à la livraison de gènes), ou non discernable, selon la position des cellules. Nos résultats démontrent clairement que l'EP des cellules dans un champ électrique non-uniforme peut être commandée par DEP.

Les mêmes microélectrodes planaires utilisées pour DEP et EP ont alors été employées pour mesurer les propriétés mécaniques de différents types de cellules mammifères en suspension, en déformant des cellules individuelles dans les champs électriques non-uniformes et variables dans le temps. Les contraintes électriques produits par ces microélectrodes planaires ont été employées pour emprisonner et étirer les cellules, alors que l'ED des cellules était observée et photo-documentée par microscopie optique. Deux types de cellule distincts ont été comparés après des données convenables à un modèle de contrainte à trois-paramètres (SLS) et à un de deux paramètres (PL). Les cellules de type « Chinese hamster ovary » (CHO) étaient approximativement deux fois plus rigides que les promonocytes humains (U937); les CHO avaient un comportement élastique avec le rétablissement de la forme initiale, alors que les U937 témoignent à la déformation plastique.

Nous avons alors ensuite exécuté des expériences d'électrodéformation avec deux types de cellules additionnelles (L929 et HEK293) où la microscopie confocal a été employée pour la visualisation et l'analyse semi-quantitative de la structure du cytosquelette (CSK) des cellules. Nous avons traité les cellules U937 avec de la latrunculin-A (Lat-A) ou de l'acrylamide (ACR) pour évaluer respectivement leurs effets sur les microfilaments (MF) et les filaments intermédiaires (IF) du CSK. Nous avons démontré que les propriétés viscoélastiques des cellules individuellement déformées sont dépendentes de l'épaisseur de l'actine corticale (AC) et ont été significativement affectées par des traitements de Lat-A. Les cellules U937 et HEK293 possèdent de minces AC et sont plus facilement déformées que les cellules CHO et L929, qui étaient plus rigides et possèdent des couches plus épaisses d'AC.

Les résultats présentés dans cette thèse démontrent que les champs électriques produit par des électrodes microfabriquées permettent la caractérisation mécanique de plusieurs types de cellules mammifères, et atteignent donc l'objectif principal de ce travail, du développement des microdispositifs pour la caractérisation mécanique de cellules individuelles.

ABSTRACT

The purpose of this study has been to describe the development and demonstration of a microfabricated platform for mechanical characterization of individual living mammalian cells in suspension. The technique uses electrical polarization forces to trap and stretch cells in time-varying, non-uniform fringing electric fields. This work was motivated by the apparent under-utilization of electrical stresses for the mechanical characterization of live cells, and the methods described here permitted mechanical characterization of diverse (previously uncharacterized) mammalian cell-types.

Mechanical characterization of cells is usually achieved by probing local structures near the cell-surface, and very few techniques apply uniaxial stresses to whole individual cells. Most mammalian cells adopt a relatively simple (spherical) geometry when they are suspended in a liquid (aqueous) medium. This simplifies cell-manipulation and permits relatively straightforward interpretation of mechanical data. Mammalian cells are increasingly being used outside of their natural environments, for example within microfluidic devices, which requires precise cell-manipulation protocols. Present miniaturization trends within experimental biotechnology are producing new tools for the precise manipulation of individual living cells, and electric fields feature prominently within this context. Electric fields exert forces on cells without the requirement of mechanical contact between cells and device structures and can therefore be described as “tractor beams”, which can move, trap, or deform electrically polarisable objects such as biological cells.

Mechanical characterization of cells by electro-deformation (ED) will be described within the larger context of cell electro-manipulations. To better understand the behaviour of cells in electric fields, we used dielectrophoresis (DEP) to position human monocytes (U937) within a non-uniform electric field prior to electro-poration (EP) for gene delivery. DEP positioning and EP pulsing were both accomplished using a common set of inert planar electrodes, micro-fabricated on a glass substrate. A single-shell model of the cell’s dielectric properties and finite-element modeling of the electric field distribution permitted us to predict the major features of experimentally observed cell positioning. The extent to which electric pulses increased the permeability of the cell-membranes to florescent molecules and to pEGFP-Luc DNA plasmids were found to depend on prior positioning. For a given set of pulse parameters, EP was either irreversible (resulting in cytolysis), reversible (leading to gene delivery), or not detectable,

depending on where cells were positioned. Our results clearly demonstrate that position-dependent EP of cells in a non-uniform electric field can be controlled by DEP.

The same planar microelectrodes used for DEP and EP were then used to measure mechanical properties of individual mammalian cells in suspension by deforming the cells in time-varying, non-uniform electric fields. Electrical stresses generated by the planar microelectrodes were used to trap and stretch cells, while (ED) was observed using optical microscopy. Two distinct cell-types were compared after fitting strain data with a three-parameter “standard linear solid” (SLS) model of viscoelasticity, and with a two-parameter power-law (PL) method. Chinese hamster ovary (CHO) cells were found to be approximately twice as stiff as U937 human promonocytes, and CHO cells displayed an elastic behaviour with full recovery of initial shape, while U937 strain data bore witness to plastic deformation.

We then extended these measurements to include two additional cell-types (L929 and HEK293); confocal immuno-fluorescent microscopy was used for visualization and semi-quantitative analysis of the cell-cytoskeleton (CSK) for all cell-types. We treated U937 cells with microfilament (MF)- and intermediate-filament (IF)- disrupting drugs, latrunculin-A (Lat-A), and acrylamide (ACR), respectively, to assess their effects on the CSK and on the mechanical properties of that cell-type. The measured viscoelastic properties of individually deformed cells depended on cortical actin (CA) thickness and were significantly affected by Lat-A treatments. U937 and HEK293 cells had thin CA and were more easily deformed than CHO and L929 cells, which were stiffer and had thicker CA layers.

The results presented in this thesis demonstrate that electrical stresses generated by micro-fabricated electrodes permit mechanical characterization of distinct mammalian cell-types, and therefore accomplish the main objective of this work.

CONDENSÉ EN FRANÇAIS

Les propriétés mécaniques du tissu vivant, y compris celles des cellules individuelles, ont des rôles essentiels dans les phénomènes biologiques. L'étude des propriétés mécaniques des cellules est devenue un sous-champ important de la biologie cellulaire. Par contre, leurs petites tailles et leur sensibilité aux contraintes mécaniques rendent les cellules difficiles à manœuvrer et leurs propriétés mécaniques sont donc difficiles à mesurer. Dans cette thèse, on présente un examen des méthodes utilisées pour la caractérisation mécanique des cellules, et on démontre le besoin de nouvelles méthodes qui peuvent déformer des cellules sans contact mécanique significatif entre les cellules et les structures du dispositif. L'utilisation des champs électriques pour l' "électro-déformation" (ED) de cellules est présentée comme un candidat potentiel pour la caractérisation mécanique des cellules. La méthode ED se fait en utilisant des électrodes microfabriquées, ce qui est de plus en plus favorisé pour les mesures biomécaniques sur de petits échantillons tels les cellules. Les avantages de l'ED comparée aux autres techniques qui sont également employées pour la caractérisation mécanique de cellules en suspension, sont les suivants: (i) L'ED élimine le besoin de pièces mobiles ou de microbilles dans la suspension de cellules; (ii) le contact mécanique entre les cellules et les structures de dispositif est réduit au minimum; (iii) les électrodes planaires pour l'ED sont facilement microfabriquées en parallèle, ce qui permet des mesures simultanées sur plusieurs cellules, et intégration simple dans des biopuces; (iv) les tensions électriques de valeurs programmables permettent l'étude des propriétés mécaniques sur plusieurs échelles de temps.

Récemment, des dispositifs microfabriqués telles les micropuces ont été utilisés pour analyser et manipuler des spécimens biologiques de plus en plus complexes pour des applications en sciences de la vie comme l'analyse génétique et le clonage. Les avantages d'utiliser des micropuces pour la bio-analyse incluent l'utilisation de plus petits échantillons et la possibilité d'exécuter beaucoup d'expériences simultanées et commandées par ordinateur. Bien qu'un progrès significatif ait été accompli, les plates-formes pour étudier la mechanobiologie de cellules vivantes sont à leur premier pas et la manipulation efficace des cellules biologiques demeure un défi important. L'objectif principal de cette thèse était donc de démontrer la caractérisation mécanique des cellules mammifères vivantes en utilisant des champs électriques. Pour atteindre cet objectif, des électrodes planaires ont été conçues pour produire des champs électriques non-

uniformes capables de piéger et déformer des cellules individuelles dans un système permettant l'observation et l'acquisition des images de déformation par microscopie optique.

La thèse commence (Chapitre 1) avec une revue des techniques employées pour étudier les propriétés mécaniques des cellules. Nous prêtons une attention particulière aux cellules en suspension et aux méthodes exigeant un contact mécanique minimal avec les cellules. Les méthodes actuellement utilisées pour mesurer les propriétés biomécaniques des cellules suspendues appliquent généralement des forces magnétiques, optiques, ou électriques pour manœuvrer et déformer les cellules. Les méthodes magnétiques et optiques exigent typiquement un attachement de particules métalliques ou autre aux cellules (dans les cellules ou sur leurs surfaces) afin de faire la couplage des forces. Les forces électriques agissent quant à elles directement sur la cellule et sont donc idéales pour l'application des forces sans l'addition de particules ou d'autres matériaux à la suspension. Bien que les forces électriques aient été employées précédemment par d'autres pour déformer des cellules, la plupart des études décrivent un type spécifique de cellules comme les érythrocytes (globules rouges) et la majorité des cellules mammifères n'ont pas été étudiés. Notre but devient alors plus clair et la question à savoir si les champs électriques provenant des microélectrodes sont suffisamment grands pour déformer plusieurs types de cellules mammifères autres que les globules rouges devient encore plus pertinente.

La deuxième partie de la thèse (Chapitre 2) présente notre démarche menant à la fabrication des outils nécessaires à l'ED de cellules suivie de nos résultats validant l'applicabilité de notre méthode d'ED pour la caractérisation mécanique de cellules. Ce chapitre constitue en fait une synthèse des trois articles en Annexes I-III déjà publiés. Pour faciliter les expériences d'ED pendant l'observation par microscopie optique, des microélectrodes ont été fabriquées sur des lames de microscope en verre standard. Pour augmenter la compatibilité de ces substrats avec les procédures photolithographiques, des couches minces à base de silicium ont été déposées sur les substrats avant la fabrication d'électrodes. Ensuite, des électrodes en platine ont été évaporées sous vide sur lesquelles des couches minces électriquement isolantes ont été déposées afin de permettre leur utilisation dans les suspensions (aqueuses) liquides. Plusieurs géométries d'électrode ont été considérées et la géométrie idéale finalement choisie pour le piégeage et déformation de cellules, décrite dans cette thèse, est composée d'une rangée d'électrodes coniques de « piégeage » opposées à une contre-électrode centrale. Le champ électrique non-uniforme, E ,

produit par ces électrodes, a été simulé utilisant les méthodes d'éléments finis (FEM). Des cellules individuelles emprisonnées à chaque extrémité des électrodes sont électriquement polarisées avec des valeurs d'E plus élevées près des pôles, comparées aux valeurs inférieures près de l'équateur. Dans le cas (non-uniforme) actuel, E est plus élevé près du pôle qui fait face au bout de l'électrode de « piégeage » et les cellules sont donc emprisonnées dans cette région: Une fois piégées, les cellules sont déformées en augmentent E. Les champs électriques agissent donc en tant que « rayon tracteur » et sont capables de déplacer, d'emprisonner, et d'étirer les cellules biologiques, sans chauffer de manière significative la suspension ou endommager autrement les cellules.

Afin de réaliser le piégeage fiable des cellules, nous avons dû mesurer leurs propriétés diélectriques. Ceci a été réalisé en mesurant le mouvement des cellules sous l'influence d'un E non-uniforme et variable dans le temps (sinusoïdal). Ce phénomène s'appelle "diélectrophorèse" (DEP) a et été mesuré en fonction de plusieurs conditions expérimentales. Nous avons donc mesuré le spectre-DEP des cellules et, en comparant ensuite les données mesurées aux modèles théoriques de la structure cellulaire, le positionnement prévisible des cellules était possible. Ces expériences ont établi la gamme des conditions expérimentales qui sont employées par la suite pour l'ED de cellules.

Afin d'établir les conditions expérimentales préservant la viabilité cellulaire nous avons réalisé des essais de viabilité pendant les expériences de DEP. Nous avons aussi étudié les effets des champs électriques pulsés sur la viabilité de cellules. Les champs électriques pulsés augmentent la perméabilité de la membrane cellulaire (CM) par un phénomène d'électroporation (EP) et les effets d'EP sur la viabilité de cellules ont aussi été examinés sous plusieurs conditions expérimentales. Au cours de ces expériences, l'EP a été utilisée dans la transfection de gènes pour la modification génétique des monocytes (U937) humains et nous avons combiné des expériences de DEP et d'EP pour des applications originales. Le placement de cellules par DEP avant d'effectuer l'EP a démontré que les modifications génétiques peuvent se faire selon un protocole sélectif au type cellulaire. Ainsi, il semble possible de viser spécifiquement un type cellulaire parmi une population hétérogène pour une application donnée comme pour la modification génétique ou la destruction.

Après la présentation des résultats de DEP et EP, la caractérisation mécanique des cellules par ED en utilisant les mêmes microélectrodes planaires est présentée. Nous avons constaté que

les valeurs d'E produites par ces microélectrodes étaient en effet suffisamment fortes pour induire l'ED de divers type de cellules mammifères. Nous présentons nos premiers résultats ED avec deux types de cellules au Chapitre 2, et d'autres résultats sont présentés au Chapitre 3 où quatre types de cellules ont été employées et où leur structure a été analysée par microscopie confocale. Les propriétés mécaniques des U937s et des cellules épithéliales de type « Chinese hamster ovary » (CHO) ont d'abord été comparées. On a ensuite paramétrisé les propriétés mécaniques de ces deux types de cellules avec deux modèles simples qui sont fréquemment employés dans la littérature. Ces mesures forment notre introduction à l'ED comme technique de caractérisation mécanique de cellules mammifères.

Pour démontrer plus en profondeur l'utilité de l'ED, on présente (au Chapitre 3) la caractérisation structurale et mécanique de quatre types de cellules différents. Il est connu que les cellules biologiques vivantes s'adaptent à leur environnement en procédant à des ajustements structuraux parfois significatifs. Les géométries adaptatives des cellules sont permis en grande partie par la flexibilité d'organisation du cytosquelette (CSK), qui est composé principalement de 3 réseaux moléculaires distincts: les microfilaments d'actine (MF), les filaments intermédiaires (IF), et les microtubules (MT).

La membrane cellulaire (CM) peut être considérée comme la « peau » des cellules; très mince (épaisseur ~10 nanomètres) avec une contribution négligeable à la rigidité globale de la cellule par rapport au CSK. En conditions isotoniques ou les cellules n'est pas gonflée la CM n'est pas étirée au maximum et permet donc les contraintes en tension. Donc, la CM limite les valeurs maximales de contrainte d'une cellule mais, pour de petites contraintes, les MFs du CSK déterminent la plupart de la rigidité mesurée. Situé dans le cortex intracellulaire, une zone étroite juste sous la CM, la plupart des filaments d'actine sont arrangés dans un maillage qui exclut la plupart des organelles du cytoplasme. Les MFs sont associés à l'interaction mécanique des cellules avec leurs environnements externes, et ils ont des rôles importants dans la propagation, la division et la motilité cellulaire. L'ensemble et l'organisation de ces réseaux moléculaires sont réglés par des facteurs génétiques, épigénétiques, et environnementaux ; les morphologies de cellules sont donc diverses et dynamiques.

Afin d'interpréter correctement des mesures mécaniques, il est utile de considérer les cas où la géométrie cellulaire est simple; c.à.d. quasi-sphérique, comme en suspension. Les propriétés mécaniques des cellules en suspension influencent de nombreuses fonctions biologiques dans

plusieurs contextes *in vivo* et *ex vivo*: Par exemple, les cellules du système circulatoire ont été intensivement étudiées d'une perspective mécanique et il est connu que leur rigidité accrue limite leur passage à travers de petits capillaires, limitant leur migration trans-endothélial. Les mesures de la rigidité cellulaire ont donc été essentielles pour déterminer les effets biomécaniques de diverses drogues et de traitements concernant des cellules dans la circulation. La géométrie sphérique des cellules suspendues a également comme conséquence la modélisation plus simple, et permet l'analyse claire des structures sous-cellulaires telles que les MFs. Pour les cellules en suspension, la plupart des MFs forment une coquille d'actine corticale (CA), dont l'épaisseur dépend du type cellulaire. Nous avons mesuré l'épaisseur du CA dans chacun des quatre types afin d'étudier son influence sur les propriétés mécaniques mesurées. L'influence d'agents qui perturbent le CSK a également été examinée, tels la latrunculin-A (Lat-A) et l'acrylamide (ACR), pour perturber les MFs et IFs, respectivement. En comparant les propriétés mécaniques mesurées des cellules traitées ou non, nous pouvons déduire l'influence de ces divers éléments structuraux du CSK.

Des quatre types de cellules examinées ici, les fibroblastes L929 étaient les plus rigides, suivis de CHO, HEK293, et U937, respectivement. Ces différences entre les propriétés mécaniques mesurées ont été attribuées à leur CSK différent et nous avons observé un rapport inverse entre l'épaisseur du CA et la déformation maximale des cellules avec les L929 ayant avec le CA le plus épais, suivi de CHO, HEK293, et finalement d'U937. L'épaisseur du CA des types de cellules examinées ici varie considérablement. Par exemple, pour les cellules L929, l'épaisseur du CA était de ~ 25% du rayon de cellules, tandis que pour les cellules U937 c'était de ~ 10 %. Les U937 sont des monocytes humains dérivés du lymphome histiocytique et sont cultivés en suspension; ils proviennent donc du système circulatoire et le fait qu'ils soient moins rigides par rapport aux autres types mentionnés ici est donc logique. Les cellules HEK293s ont également été facilement déformées avec un CA mince. Bien que les HEK293s aient été dérivées d'une source humaine embryonnaire de rein, elles ont été récemment liées aux cellules neurales, et leur lignée vraie n'est pas connue. Nous concluons donc que l'épaisseur du CA est une cause déterminante des propriétés mécaniques au niveau de la cellule entière et que ces propriétés peuvent être mesurées par ED.

En perturbant le CSK par des traitements de Lat-A ou ACR nous pouvions réduire la rigidité des cellules. Le CA a été distinctement perturbé par Lat-A mais les effets d'ACR étaient

moins clairs. La réduction d'élasticité des cellules était une fonction de temps de traitement et nous pourrions donc commander l'élasticité des cellules par le choix appropriés des temps de traitement. A partir des traitements de Lat-A, nous avons constaté que la rigidité des cellules pouvait être réduite par un facteur de ~ 2 avant que la viabilité des cellules ne soit affectée. En utilisant de plus longs temps de traitement, l'élasticité des cellules a été encore réduite et les cellules ne sont pas revenues à leurs formes sphériques originales après l'étirement, indicatif d'un effet sur la santé cellulaire. Les traitements de Lat-A ont eu comme conséquence un CA plus mince et ont mené aux trous dans le CA, ce qui était clairement mis en évidence par les observations au microscope confocal. Les traitements avec ACR à basses concentrations ont quant à eux affecté les réseaux IF, mais de longs temps de traitement étaient exigés pour causer des changements mesurables de l'élasticité, ayant comme conséquence la rupture concomitante des IFs et des MFs. Le rôle de l'ACR est donc moins clair que le Lat-A car il n'est pas spécifique à un seul type de réseau du cytosquelette aux concentrations utilisées ici.

Nous avons également noté plusieurs résultats inattendus de ces traitements qui ont facilité la manipulation des structures sous-cellulaires. Ces résultats additionnels incluent l'électro-manipulation du noyau et de l'extrusion de matériaux du cytosol et sont présentés dans les sections finales du Chapitre 3. Ces résultats inattendus suivent donc les résultats principaux d'ED et sont présentés afin de donner au lecteur un sens du potentiel pour les futurs dispositifs en lesquels la chirurgie unicellulaire est exécutée utilisant des techniques semblables à ceux présentées ici. Par exemple, l'utilisation des champs électriques pour la fusion des cellules multiples est bien établie et employée couramment pour la production et le clonage d'hybridome. Notre démonstration que ces méthodes peuvent être accomplies avec les microélectrodes planaires est originale et importante pour le développement de futurs dispositifs.

Pour récapituler, nos résultats permettent d'affirmer que notre objectif principal a été atteint en démontrant clairement l'applicabilité de l'ED pour la caractérisation mécanique de diverses cellules mammifères (précédemment non caractérisées) en suspension. Une large variété de manipulations cellulaires et sous-cellulaires ont été effectuées: DEP, EP, et ED pour le positionnement de cellules, la modification génétique, et la déformation, respectivement, ont été tous accomplis utilisant les mêmes microélectrodes planaires. Bien que ces techniques aient été précédemment rapportées par d'autres, on a présenté des applications originales de chaque technique et les expériences d'ED présentées ici sont les premières qui ont comparé

systématiquement la biomécanique des cellules mammifères de divers types en fonction de leur structure cytosquelettique.

Les électrodes planaires décrites sont aisément incorporées dans les plates-formes de microtechnologie, et la technique du « rayon tracteur » peut déplacer ou déformer les objets polarisables électriquement tels que les cellules biologiques, tout en réduisant au minimum le contact mécanique entre ces objets et les structures du dispositif. Ceci réduit le collage de cellules et permet des analyses en continu, auxquelles différentes cellules individuelles sont déplacées avec précision entre les stations expérimentales dans le dispositif. En suivant les méthodes décrites ici pour la microfabrication à basse température (dépôts de couches assistés par plasma), nous avons fabriqué des dispositifs d'ED sur le verre ou les substrats en plastique transparent (de polymère), et nous nous attendons donc à de futures réalisations diverses basées sur les méthodes décrites dans cette thèse.

TABLE OF CONTENTS

DEDICATION	iii
ACKNOWLEDGMENTS.....	iv
RESUME.....	v
ABSTRACT.....	vii
CONDENSÉ EN FRANÇAIS	ix
TABLE OF CONTENTS	xvi
LIST OF TABLES	xviii
LIST OF FIGURES.....	xix
LIST OF SYMBOLS AND ABBREVIATIONS	xxi
LIST OF APPENDICES	xxiv
INTRODUCTION.....	1
CHAPTER 1. MECHANICAL PROPERTIES OF MAMMALIAN CELLS.....	5
1.1 Introduction to mammalian cells.....	5
1.1.1 Structural properties	5
1.1.2 Mammalian cells in suspension.....	7
1.1.3 Measured mechanical properties.....	8
1.2 Microtechnology platforms for life-science applications.....	11
1.3 Electro-manipulation of cells	12
1.3.1 Dielectrophoresis.....	12
1.3.2 Electroporation	14
1.3.3 Combined dielectrophoresis and electroporation.....	15
1.3.4 Electrodeformation.....	16
CHAPTER 2. METHODS AND RESULTS	18
2.1 Methods.....	18
2.1.1 Theory	18
2.1.1.1 Calculation of applied electrical stresses.....	19
2.1.1.2 Viscoelastic properties (SLS model).....	25
2.1.1.3 Power-law model.....	26

2.1.2 Finite element methods	27
2.1.3 Microfabrication of electrodes	29
2.1.4 Cell culture	31
2.1.5 Cell-viability tests	32
2.1.6 Cell-suspension medium	32
2.1.7 Electro-manipulation of cells	33
2.1.7.1 Dielectrophoresis.....	33
2.1.7.1 Electroporation	36
2.1.7.1 Electrodeformation.....	36
2.1.8 Disruption of the U937-cytoskeleton	38
2.1.9 Confocal microscopy.....	38
2.2 Results	41
2.2.1 Dielectrophoresis.....	41
2.2.2 Electroporation	44
2.2.3 Electrodeformation.....	48
CHAPTER 3. SUPPLEMENTARY RESULTS	51
3.1 Dielectrophoresis in gels	51
3.2 Electrofusion	51
3.3 Electrodeformation.....	53
3.3.1 Electrodeformation of several mammalian cell-types.....	53
3.3.2 Cortical actin thickness	55
3.3.3 Modification of the U937 cytoskeleton.....	58
3.4 Electro-manipulation of sub-cellular structures	62
CHAPTER 4. GENERAL DISCUSSION	64
CONCLUSION	67
BIBLIOGRAPHY	68
APPENDICES.....	74

LIST OF TABLES

Table 1.1	Methods used to characterize the passive mechanical properties of cells.....	9
Table 2.1	Mechanical properties of cells derived using the SLS model.....	50
Table 2.2	Model parameters for the “power-law solid” (PL).....	50
Table 3.1	Viscoelastic (SLS) parameters of several cell-types.....	54
Table 3.2	Cortical thickness and maximal strain-values.....	57
Table 4.1	Physical and viscoelastic (SLS) properties of several cell-types.....	65

LIST OF FIGURES

Figure 1.1 Structural features of mammalian cells.....	6
Figure 1.2 Methods used to measure mechanical properties of cells.....	9
Figure 1.3 Depiction of the typical length-scales and elastic modulus values for several materials.....	11
Figure 1.4 Increased use of dielectrophoresis (DEP) in the last decade.....	14
Figure 1.5 Several effects of pulsed electric fields applied to cells.....	14
Figure 1.6 Electro-deformation of an erythrocyte (red-blood-cell, RBC).....	16
Figure 2.1 Simplified dielectric model of a suspended mammalian cell.....	20
Figure 2.2 The real part of the (dipole) polarization factor.....	21
Figure 2.3 Frequency-dependent plots of the complex polarization factor.....	22
Figure 2.4 Simplified model of cell-deformation.....	24
Figure 2.5 Finite-element simulations of E.....	27
Figure 2.6 Finite-element simulations of E, magnified view.....	28
Figure 2.7 Ti/Pt electrodes deposited on a glass microscope slide.....	30
Figure 2.8 Microscopy system used for ED.....	34
Figure 2.9 Cell-viability during DEP.....	35
Figure 2.10 Trapping and stretching of U937 cells.....	37
Figure 2.11 Fluorescence intensity of actin labeled with Alexa-488-phalloidin.....	39
Figure 2.12 Positioning of U-937 monocytes by DEP.....	42
Figure 2.13 The crossover frequency, f_0 , versus conductivity of the extracellular medium, for U-937 monocytes.....	43
Figure 2.14 Position-dependent EP of U-937 monocytes.	45
Figure 2.15 Calculated position-dependence of EP of U-937 monocytes, for different values of U.....	46
Figure 2.16 Position-dependent transfection of U937 cells.....	47
Figure 2.17 CHO stretching and recovery.....	48
Figure 2.18 U937 stretching and recovery.....	49
Figure 2.19 Strain and relaxation data for U937and CHO cells, fit using the “standard linear solid” (SLS) or power-law (PL) models.....	50
Figure 3.1 Electro-fusion of U937 monocytes.....	52

Figure 3.2 Trapping and deformation of cells.....	53
Figure 3.3 Time-dependent strain-data, $\gamma(t)$, of four cell-types.....	54
Figure 3.4 Cortical actin in four differing cell-types.....	57
Figure 3.5 Linear correlation between maximum strain and cortical actin thickness.....	58
Figure 3.6 Time-dependent effects of 10 μM latrunculin-A treatment in U937 cells.....	59
Figure 3.7 Time-dependent effects of 10 mM acrylamide treatment in U937 cells.....	60
Figure 3.8 Strain data for U937 cells following treatment with 10 μM latrunculin-A or 10 mM acrylamide.....	61
Figure 3.9 Electromanipulation of a cell-nucleus.....	62
Figure 3.10 Electromanipulation of blebs and nanoparticles.....	63
Figure 3.11 Electromanipulation of cell-ghosts.....	63
Figure 4.1 Planar electrode array micro-fabricated on a transparent insulating (flexible) polymer substrate.....	65

LIST OF SYMBOLS AND ABBREVIATIONS

U	electric potential	V
E	electric field strength	V/m
E_{rms}	electric fields strength (root-mean-squared)	V/m
f	frequency	Hz
f_0	crossover frequency (DEP)	Hz
J	material compliance	1/Pa
C	cell compliance factor	m^2/V^2
k	elastic constant	Pa
E_0	initial elastic modulus	Pa
E_R	relaxed elastic modulus	Pa
G_0	initial shear modulus	Pa
G_R	relaxed shear modulus	Pa
a	position of maximum pixel intensity	(m)
A	power-law prefactor	$\text{s}^{-\alpha}/\text{Pa}$
r_c	cell radius	(m)
d	distance (minimal gap between electrodes)	(m)
d_{CM}	cell-membrane thickness	(m)
d_{exp}	cortical actin thickness	(m)
$d_{\%}$	cortical actin thickness (percent of cell-radius)	(dimensionless)
F	force	N
I_a	pixel intensity	(dimensionless)
I_{max}	maximum pixel intensity	(dimensionless)
k_{out}	exponential decay-factor outside the cell	(1/m)
k_{in}	exponential decay-factor inside the cell	(1/m)
K	Clausius-Mosotti factor	dimensionless
L	length	m
L_0	initial length	m
L_x	length of ellipsoid major-axis	m
L_y	length of ellipsoid minor-axis	m

N_T	number of transfected cells	(dimensionless)
r_c	cell radius	m
α	power-law exponent	dimensionless
γ	strain	dimensionless
γ_x	strain of ellipsoid major-axis	dimensionless
γ_y	strain of ellipsoid minor-axis	dimensionless
ε	dielectric permittivity	F/m
η	viscosity	Pa·s
ν	Poisson's ratio	dimensionless
σ	electric conductivity	S/m
τ	time constant (or "relaxation time")	s
ω	angular frequency	rad/s
ζ	stress	Pa

ACR	Acrylamide
AFM	Atomic force microscopy
CA	Cortical actin
CM	Cell-membrane
CSK	Cell-cytoskeleton
DEP	Dielectrophoresis
nDEP	Negative dielectrophoresis
pDEP	Positive dielectrophoresis
DS	Dielectric spectroscopy
ED	Electro-deformation
EF	Electro-fusion
EP	Electro-poration
ER	Electro-rotation
IF	Intermediate filament
Lat-A	Latrunculin-A
LOC	Lab On a Chip

MEMS	Micro-electro-mechanical systems
MF	Microfilament
MFS	Minimum feature size
MPA	Micropipette aspiration
MSC	Mesenchymal stem cell
MT	Microtubule
MTC	Magnetic twisting cytometry
OT	Optical trapping
PECVD	Plasma-enhanced chemical vapour deposition
RBC	Red-blood-cell

LIST OF APPENDICES

APPENDIX I. PECVD of nanocrystalline Si layers on high- T_g polymer substrates	74
APPENDIX II. Gene delivery by electroporation after dielectrophoretic positioning of cells in a non-uniform electric field.....	86
APPENDIX III. Mechanical properties of mammalian cells in suspension measured by electro-deformation.....	104

INTRODUCTION

The mechanical properties of living tissue, including individual cells, play a key role in the understanding of biological phenomena. Therefore, the study of cell-mechanics has become an important sub-field of cell biology. In recent years, microtechnology platforms have been used to analyse and manipulate increasingly complex biological specimens for life-science applications. Although significant progress has been made towards the goal of manipulating individual biological cells, many basic questions remain unanswered and improved technology-platforms are required to achieve reliable manipulation and characterization of individual mammalian cells. Structural and mechanical properties are among the measurable characteristics, which are fundamental to the forms and functions of cells, and have therefore been studied using a large variety of techniques. However, few of these techniques are readily microfabricated and very few can handle individual cells without requiring significant mechanical contact between cells and device structures. Non-contact methods for mechanical manipulation of cells use either magnetic, optical, or electrical forces, but the former two typically require the attachment of beads to the cells, in order to provide adequate force-coupling. Electrical forces act directly on the cell without requiring the addition of beads or other materials to the cell suspension, and are therefore more suitable for non-contact cell manipulations. Electric fields act as “tractor beams” and are capable of moving, trapping, and stretching biological cells, without significantly heating the cell-suspension or otherwise damaging the cells. It therefore seems likely that electric fields are underutilized for the study of cell mechanics.

The first part (Chapter 1) of this thesis introduces the basic structural components of mammalian cells, which determine the cell’s mechanical properties. A review of experimental techniques that have been used to measure the cell’s mechanical properties is then provided. This literature review includes recently developed miniaturized systems, and highlights the need for new methods to characterize cells in suspension. The use of applied electric fields for various cell-manipulations will be reviewed, and their potential use for mechanical characterization of cells in suspension will be presented. The second part (Chapter 2) summarizes three published articles, which are included in Appendices I-III. Chapter 2 is divided into two parts: A methods section (2.1) and a results section (2.2). The experimental methodology includes theory, modelling, micro-fabrication, and cell-manipulation protocols. Simplified models of the cell were

used to predict cell-positioning and to estimate the mechanical properties of deformed cells, and the fringing electric field generated by the electrodes was simulated using finite element methods (FEM). I used standard microfabrication procedures to produce planar (Ti/Pt) electrodes on glass or plastic substrates. Lastly, I describe the use of this microdevice for cell manipulations, during observation by optical microscopy. Chapter 3 contains supplementary results, which have not yet been published.

The main objective of this work was the development and demonstration of a microtechnology platform for the mechanical characterization of individual mammalian cells in suspension. Although electrical forces have been used previously by others to deform cells, most reports describe erythrocytes (red blood-cells) and the majority of mammalian cell-types have not been studied. We hypothesized that cell-deformation in strong electric fields can be used to characterize the mechanical properties of a wide variety of previously uncharacterized mammalian cells. I therefore designed novel planar electrode structures for generating spatially non-uniform fringing electric fields, and used them to trap and deform several (previously uncharacterized) mammalian cell-types in suspension, during observation by optical microscopy. The planar electrodes are readily incorporated within array-based microtechnology platforms, and the “tractor beam” technique can displace or deform electrically polarisable objects such as biological cells, with minimal mechanical contact between these objects and the device structures. This reduces cell-sticking and permits assembly-line assays, in which individual cells are precisely moved between experimental stations within the device.

To accomplish the main objective of individual cell deformation, the following three specific challenges were addressed: (i) low-temperature deposition of thin film “barrier” materials to protect electrodes within liquid (aqueous) solutions; (ii) design and testing of electrode geometries, which permit the capture and deformation of individual cells; and (iii) dielectric characterization of cells to increase the reliability and versatility of cell-manipulation using electric fields.

To facilitate ED experiments during observation by optical microscopy, electrodes were microfabricated using standard glass microscope slides as substrates. Electrode structures were then patterned using photolithography and Pt/Ti electrodes were evaporated under vacuum. Electrically insulating thin films were also deposited over the electrodes in order to permit their

use within liquid (aqueous) suspensions. To ensure that these thin film fabrication procedures were compatible with emerging soft-lithographic procedures, I developed methods for silicon-based thin film deposition at low temperatures ($T < 150\text{ }^{\circ}\text{C}$), using plasma-enhanced chemical vapour deposition (PECVD).

Several electrode geometries were considered for the purposes of this work, and the ideal geometry for cell-trapping and -deformation is described; it consisted of an array of tapered “cell-trapping” electrodes, which are opposed by a central counter electrode. The non-uniform E , which is generated by these electrodes, was simulated using finite-element-methods (FEM). Individual cells, which are trapped at each electrode tip, become electrically polarized, with higher E -values near the cell-poles compared with lower E -values near the equator. In the present (non-uniform) case, E is highest near the cell-pole that faces the electrode tip and cells are therefore trapped in this region. I defined positions within $50\text{ }\mu\text{m}$ of the electrode edges as strong- E regions, and otherwise as weak- E . The values of E averaged over the strong and weak regions differed by a factor of approximately three. For example, when the applied voltage was $U = 10\text{ V}$, the maximum value of $E = U/l$, where l is the inter-electrode distance, was 200 kV m^{-1} . The E values averaged over the strong- and weak- E regions were $\sim 180\text{ kV m}^{-1}$ and $\sim 60\text{ kV m}^{-1}$, respectively. These values are consistent with previous reports of dielectrophoresis (DEP) and electro-deformation (ED). DEP results were used to validate cell-positioning capabilities and to determine proper operating conditions for ED.

Cells were patterned according to the electric field distribution, E , which was predicted by FEM simulations. Cells were moved either towards or away from the strong- E regions, depending on experimental conditions. Cell-positioning by DEP prior to the delivery of electric pulses for EP, demonstrated position-dependent EP of the cell-membrane. These results showed that the outcome of EP could be controlled by DEP and, suggested that cell-type dependence of these results was possible. Thus, it seems possible that cells of a particular type, which form part of a heterogeneous cell-suspension, may be specifically targeted for genetic modification or destruction.

Mechanical characterisation of cells by ED is then presented: We found that planar microelectrodes did indeed generate (non-uniform) E of sufficient magnitude to induce substantial deformation of individual (L929, CHO, HEK293, and U937) cells in suspension.

Mechanical properties of these cells were parameterized using two simple models, which are frequently encountered in the literature. In the three-parameter “standard linear solid” (SLS) model, a single relaxation process characterizes the cell’s strain relaxation, whereas, in the two-parameter power-law (PL) model, a continuum of relaxation processes is assumed. The main objective of this thesis was therefore achieved and cell-deformations, observed by optical microscopy, enabled the fitting of measured strain data with well-known mechanical models of cell behaviour. These results constitute the first systematic study of ED with several different mammalian cell-types.

The most important contribution of this work is the experimental development and demonstration of microfabricated ED platforms. Some advantages of ED over other techniques used for mechanical characterization of individual cells in suspension are the following: (i) ED obviates the need for moving parts or for micro-beads in the cell suspension; (ii) mechanical contact between cells and device structures is minimized; (iii) planar electrodes for ED are easily micro-fabricated as arrays, which enables simultaneous measurements on several cells, and simple integration within biochips; and (iv) programmable ranges of U values enable the study of mechanical properties over multiple timescales.

CHAPTER 1. MECHANICAL PROPERTIES OF MAMMALIAN CELLS

This chapter introduces the basic structural components of mammalian cells, which determine the cell's mechanical properties; it also reviews experimental techniques, which have been used to measure the mechanical properties of cells and cell-structures. Emphasis is placed on suspended cells; following a brief introduction to microtechnology platforms for cell-based analysis and modification, cell-manipulation using electric fields is reviewed. The chapter concludes with an explanation of the motivation and the objectives of this thesis.

1.1 Introduction to mammalian cells

Biological cells are the smallest functionally autonomous units of living organisms, and are therefore referred to as the “building blocks” of life. Cells are defined structurally by a distinct boundary, the cell-membrane (CM), which separates the interior (the cytosol) from the external environment. Inside the cell is a complex dynamic arrangement of organelles and interacting molecular networks, which give life to the cell.

1.1.1 Structural properties

Living biological cells adapt to their environments continuously, often undergoing drastic structural adjustments. Adaptive cell-geometries are permitted by the organizational flexibility of the cytoskeleton (CSK), which consists of several distinct but interacting molecular networks (simplified in Fig. 1.1): These include actin-based microfilaments (MF), intermediate filaments (IF), and microtubules (MT) [1]. The assembly and organization of these CSK networks are regulated by genetic, epigenetic, and environmental factors, and cell morphologies are therefore diverse and dynamic [2]. In order to reliably interpret mechanical measurements performed on individual (whole) cells, it is therefore necessary to establish conditions in which the cell's major structural features can be regulated and their roles in determining the measured mechanical properties established [3].

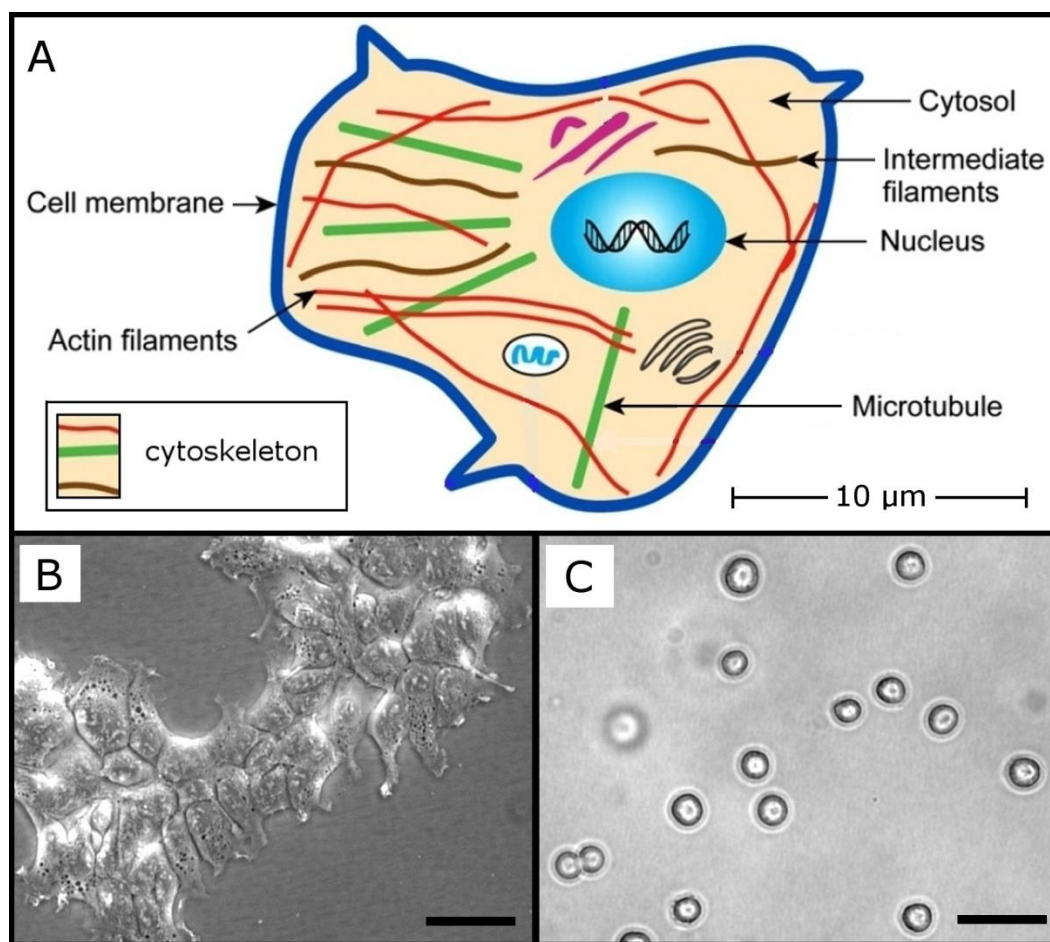


Figure 1.1 Structural features of mammalian cells. (A) Simplified model of a cell with major features labelled; adapted from [3]; (B) HEK293 cells in monolayer culture; scale bar = 30 μm (C) HEK293 cells in suspension; scale bar = 30 μm.

The CM can be thought of as the cell's "skin"; it is very thin ($d_{CM} \sim 10$ nm, [2]), and its contribution to the overall stiffness of the cell is small in comparison to the CSK [4]. In isotonic conditions, the CM is ruffled and therefore not maximally extended; for example, in hypotonic media, the expansion of chondrocytes to twice their isotonic volumes was observed [5]. The CM therefore limits maximal strain values of cells but, for small strains, the MF CSK mostly determines measured stiffness [4].

Located mostly in the cortex, a narrow zone just beneath the CM, most actin filaments are arranged into a meshwork that excludes most organelles from the cortical cytoplasm [6]. MFs are therefore closely associated with the mechanical interaction of cells with their external environments, and they have important roles in cell spreading and motility. Dramatic demonstrations of MF remodelling in response to mechanical cues has been achieved using micro-patterned substrates to define novel cell-geometries [7].

The mechanical microenvironment seen by cells *in vivo* depends on the type of tissue in which they are located. Solid tissues exhibit a range of stiffness values, as measured by the elastic modulus, E_0 (kPa) [8]: Brain (~1), muscle (~10), collagenous bone (~50). The microenvironment's stiffness has a strong impact on cell-phenotypes and is known to determine lineage specification of multipotent cells: For example, polyacrylamide gels of varying stiffnesses were found to be either neurogenic (0.1 – 1 kPa), myogenic (8 – 17 kPa), or osteogenic (25 – 40 kPa), when used as substrates for mesenchymal stem cell (MSC) differentiation and proliferation [8]. Measured mechanical properties of individual cells are therefore used to establish potential relationships between the stiffness of cells, their microenvironments, and their composite tissues.

1.1.2 Mammalian cells in suspension

The mechanical properties of mammalian cells in suspension are important determinants of biological functionality in several *in vivo* and *ex vivo* contexts. Cells of the circulatory system, for example, have been extensively studied from a mechanical perspective, and increased stiffness of diseased erythrocytes (red blood-cells, RBC) and leukocytes is known to restrict their flow through small capillaries [9-12]. Increased stiffness of both lymphoid and myeloid leukemia cells has been shown to result from some chemotherapy treatments [10], and cell-stiffness has been used as marker for various cancers [3]. Measurements of stiffness have therefore been essential for determining the biomechanical effects of various drugs and treatments relevant to cells in circulation.

Mammalian cells are increasingly being used for the production of recombinant proteins and related products in large-scale bioreactors [13], and suspension culture permits mammalian cells to grow in bioreactors by methods similar to those used in microbial systems that enable scale-up [14]. The range of available culture conditions is, however,

limited by shear and extensional forces, which are present in several types of bioreactors [15-17]. To reduce the harmful effects of mechanical stresses, shear-stress modifiers are often added to cell suspensions, although some of these additives can enter through the cell-membrane, with unknown consequences to the health and function of the cultured cells [19]. Methods to quantify mechanical properties of suspended cells can therefore be used to improve the design of new cell-types, bioreactors, and micro-fluidic devices, by predicting the cellular elastic and viscoelastic responses to various forces.

In contrast with the diversity of adherent cell geometries, mammalian cells often assume a roughly spherical geometry when they are suspended in a liquid (aqueous) medium. With the notable exception of RBCs [20], cell-types for which spherical geometries have been observed in suspension include the following: Fibroblasts [4], articular chondrocytes [5], adipose derived adult stem (ADAS) cells [22], bone marrow-derived adult mesenchymal stem cells (MSCs) [22], and others examined in later sections (Chapters 2 and 3) of this thesis. Thus, a rounded (suspended) geometry is common to many cell-types from diverse mammalian tissue sources. In suspended cells, cortical actin (CA) forms a semi-rigid shell, which is clearly visible using fluorescence microscopy [5]. Although interior structural elements such as the cell-nucleus contribute to the cell's exact shape via their loose coupling to the cortex, the CA (and its thickness) mainly determines the cell's structural response [4].

1.1.3 Measured mechanical properties

The mechanical properties of cells have been studied in detail using a large variety of experimental techniques (Fig. 1.2), which generally involve the application of external mechanical stresses, followed by observation of the cell's structural responses. These techniques are classified according to the several criteria (Table 1.1), including the amplitude and distribution of stresses applied to the cell. The majority of these techniques probe small regions on or within the cells and therefore measure local mechanical properties. At these sub-cellular length-scales, mechanical properties are heterogeneous and differing measurement protocols have therefore resulted in a large range of reported cell-elasticity values (Fig. 1.3: $100 \text{ Pa} < E_0 < 10,000 \text{ Pa}$) [3].

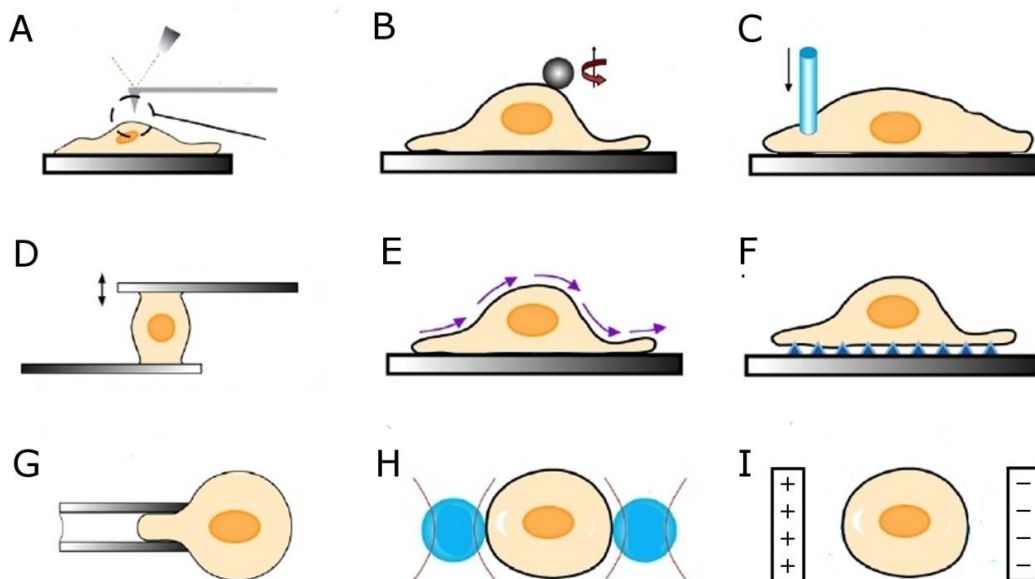


Figure 1.2 Methods used to measure mechanical properties of cells. (A) atomic force microscopy; (B) magnetic twisting cytometry; (C) cyto-indentation; (D) micro-plate stretching; (E) fluid flow rheometry; (F) substrate deformation; (G) micro-pipette aspiration; (H) optical trapping; (I) electro-deformation. Adapted from [3].

Table 1.1 Methods used to characterize the passive mechanical properties of cells

Method	Force range (nN)	Cell morphology*	Probe area [§]	References
AFM	0.01 – 100	Spread	Local	[22]
MTC	0.01 – 100	Spread	Local	[33]
Indentation	0.01 – 100	Spread	Local	[40]
MPA	0.01 – 100	Rounded	Local	[9]
OT	0.01 – 1	Rounded	Local	[3]
ED	0.01 – 10	Rounded	Global	Present work

*Cell morphologies typically used; exceptions are discussed in the main text.
[§] Probe area: “Global” if the whole cell is stretched without requiring mechanical contact between the testing device and a localized region of the cell.

Very few techniques are available for the mechanical characterization of whole suspended cells. Although traditional techniques such as AFM have been adapted for use with suspended cells [22], they are nevertheless limited to probing local structures. This limitation is partially overcome by the following four techniques: (i) micropipette aspiration (MPA: Fig. 1.2 G) [9];

(ii) magnetic twisting cytometry (MTC: Fig. 1.2 B) [30-33]; (iii) optical traps (OT: Fig. 1.2 H), [21, 34, 35]; and (iv) electro-deformation (ED: Fig. 1.2 I) [36-39]. In the next three paragraphs (following Fig. 1.2 and Table 1.1), I will discuss these four techniques (MPA, MTC, OT, and ED) separately.

Measurement of the apparent membrane tension of sea urchin eggs ($r_c \sim 50 \mu\text{m}$), by partial aspiration of cells into narrow ($\sim 10 \mu\text{m}$) pipette capillaries, was reported in 1954 [23]. This technique was soon named “micropipette aspiration”, and was applied to RBCs [24-26] and other cells of the circulatory system such as granulocytes [29]. MPA has also been applied to adherent cell-types, such as articular chondrocytes [5], which are not traditionally cultured in suspension. Only a portion of the cell is aspirated during MPA experiments, and pipettes possessing several differing diameters are often used to characterize cells. Furthermore, significant mechanical contact between cells and pipettes complicates the interpretation of mechanical deformation data.

Magnetic fields have been used to study cell rheology since the 1940s [30, 31]. Magnetic fields exert forces on small particles, which are either injected into the cell [30], or attached to the cell-surface [33]. Magnetic-twisting-cytometry (MTC) therefore probes local structures and different transmembrane receptors were found to differ in their ability to mediate force transfer across the cell surface [32].

Radiation pressure resulting from differing optical properties (refractive indices) of suspension media and suspended bodies has been used to manipulate a wide variety of particles and objects by “optical trapping” (OT) [34, 35, 41]. Optical radiation can, however, easily damage cells [42], and stresses are therefore usually coupled indirectly, for example by attaching beads to the cells (Fig 1.2 H).

Electrical stresses and electro-deformation (ED) result from differing dielectric properties of suspension media and suspended bodies. Like OT, ED is generally applicable to suspended bodies such as drops of liquid [43] or membrane-bound vesicles [44]. Although ED of biological cells has been sporadically reported since the 1970s, including ED of amoebae [45], murine Sp2 myeloma cells [46], and non-mammalian protoplasts [39], RBCs remain the only cell-type to have been studied in detail, by multiple independent researchers [36-38, 47, 48]. ED will be discussed in greater detail (in Sect. 1.3.4), after microtechnology platforms and electro-manipulation techniques have been introduced.

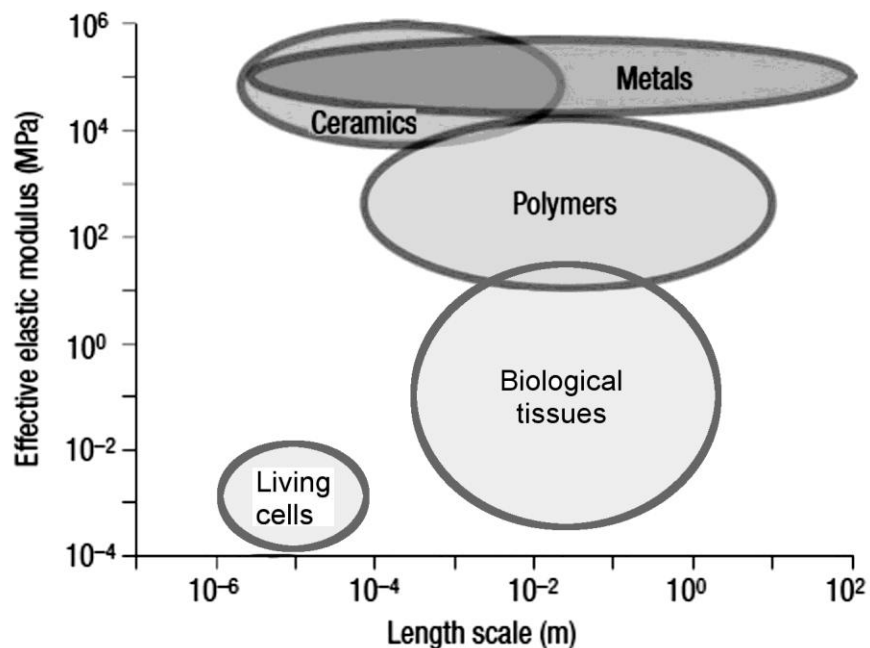


Figure 1.3 Depiction of the typical length-scales and elastic modulus values for several materials. Adapted from [49].

1.2 Microtechnology platforms for life-science applications

As discussed in the previous section of this thesis, the diameter of a typical suspended mammalian cell is on the order of $\sim 10 \mu\text{m}$. Modern semiconductor manufacturing processes are capable of producing electronic devices with minimum feature sizes (MFS) well below 100 nm [50]. Many semiconductor foundries are finding new opportunities in the life-sciences, where MFS-requirements are less stringent than they are for most electronic applications. Life-science applications do, however, present new challenges associated with the handling of complex biological objects within aqueous environments [51]. The need to fabricate on-chip channels and chambers to handle aqueous suspensions has resulted in the emerging fields of soft-lithography [52], and microfluidics [53].

Many of these efforts have benefited from existing micro-electro-mechanical systems (MEMS) technologies, which have been developed for a wide variety of applications [54]. Integration of MEMS-based micromanipulation tools within microfluidic platforms permits precise manipulation of individual biological cells [51, 55].

As tools for bio-analysis continue to be miniaturized, with the goal of integrating multiple laboratory functions within small, electronically controlled devices, these “Labs On Chips” (LOCs) will replace traditional laboratory assays with ever-decreasing on-chip footprints [56]. Commercial LOC platforms for the analysis of molecules, such as DNA or proteins, are available, and several LOC platforms have been recently developed to handle cells [57, 58] and tissue constructs [59, 60]. The potential advantages of increased parallelism, smaller sample sizes, and computer-controlled automation of experiments motivates our search for effective micromanipulation techniques, which can be included in LOC platforms. Efforts made in this thesis to develop low-temperature, plasma-based fabrication methods for use with typical soft-lithography materials are represented by our first published article (Appendix I).

1.3 Electro-manipulation of cells

From early dielectric spectroscopy (DS) experiments, the dielectric properties of individual cells were originally inferred by varying their concentrations in suspension and by measuring the dielectric properties of the suspensions [61, 62]. Subsequent observations revealed diverse types of interactions between electrically polarised cells in an externally applied electric field, E : In a spatially non-uniform E , displacement of cells toward either stronger- or weaker- E -regions was observed to depend on the cells’ dielectric properties [63], and application of pulsed E disrupted cell-structures such as the CM [64]. In combination, pulsed and oscillating E have been used to fuse two or more cells into new hybrid cell-types [65]. Transient cell-deformation occurs in sufficiently strong pulsed- [38] or oscillating- [36] E .

1.3.1 Dielectrophoresis

Biological cells of various types can be distinguished from one-another and displaced within a liquid medium using dielectrophoresis (DEP) [63, 66, 67]. In a spatially non-uniform

E, the differential electric polarizability of cells and their suspending medium produces the DEP force, which can be either attractive (towards the strong-E regions) or repulsive (towards the weak-E regions), depending on experimental conditions. Attractive or repulsive DEP forces are usually referred to as “positive” (pDEP) or “negative” (nDEP), respectively. Measurement of the DEP force as a function of experimental variables produces DEP “spectra” which are characteristic of each cell-type; DEP has therefore been used to identify and select rare cells from heterogeneous populations [68, 69]. DEP forces are significantly larger than other forces arising from gravity (sedimentation) or fluid flow under normal conditions [70, 72], and DEP has therefore been widely used to trap and hold cells in precise locations [71, 72]. In microfluidic devices, DEP has been used to transport and position cells with sufficient precision to enable single-cell manipulation [73]. Increased use of microtechnology platforms for life-science applications, which demand efficient methods to manipulate living cells on an individual basis, has therefore resulted in a growing interest in DEP (Fig. 1.4) [74].

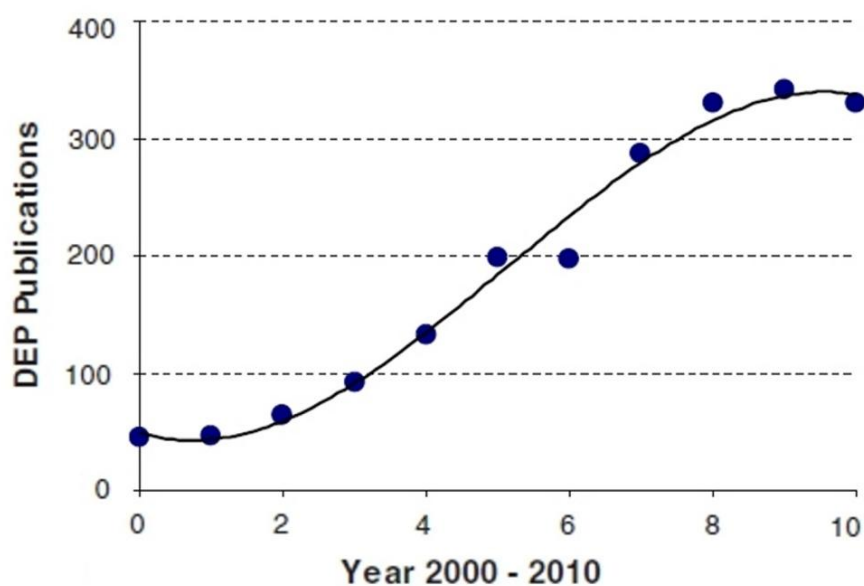


Figure 1.4 Increased use of dielectrophoresis (DEP) in the last decade. The number of DEP publications is plotted against time (in years), over the last decade (years 2000-2010). Reproduced from [74].

1.3.2 Electro-poration

Electro-poration or electro-permeabilization (EP) results from the application of an intense electric field to bring about structural changes of the cell membrane that increase its permeability. It is well known that irreversible EP leads to cytolysis [75], while reversible EP can be used to transfer molecules such as DNA into the cells while maintaining high rates of cell survival [64]. Generally, pulsed electric fields are used and the extent of EP is determined by parameters such as the strength, duration, and repetition rate of the electric pulses. Critical values of the electric field strength, which determine whether cell-membrane EP is reversible or irreversible, are specific to each cell-type and are usually determined by performing experiments at different E-values [76, 77].

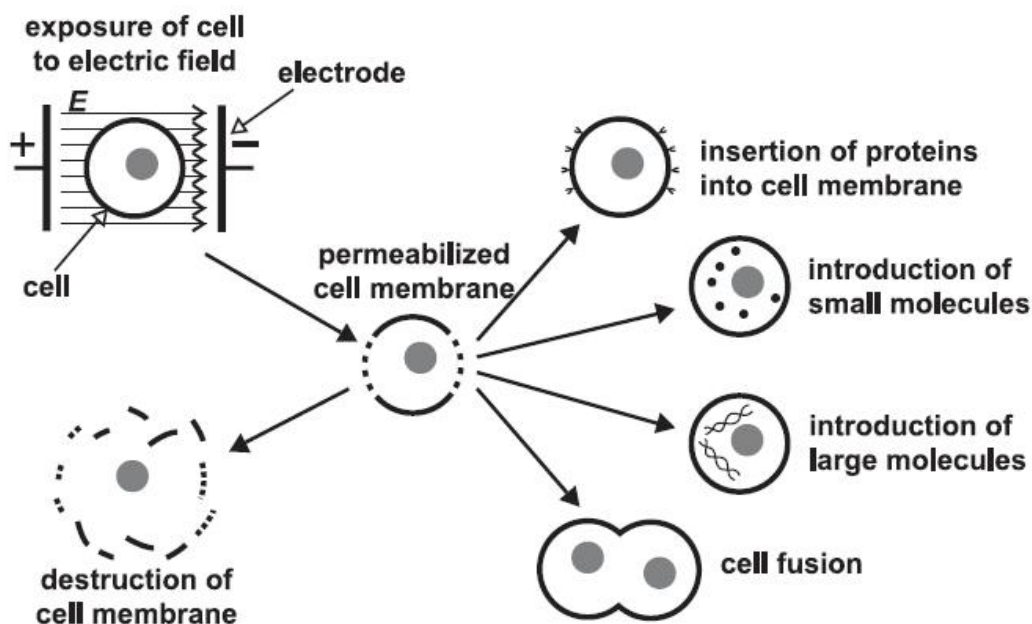


Figure 1.5 Several effects of pulsed electric fields applied to cells. Increased permeability of the CM, which results from the application of a pulsed electric field, has been used to insert molecules into the cell, to fuse two or more cells together, or to destroy cells; image is from [77].

Traditionally, *in vitro* EP has been accomplished using electrodes with mm spacing, and the position of individual cells within the electrode chamber did not need to be considered [78]. In contrast, micro-fabricated devices for EP accommodate relatively small numbers of cells and their smaller (sub-mm) electrode dimensions require consideration of spatial non-uniformities in E and of cell-positioning with respect to the electrodes [79-83]. Cell-positioning by DEP is known to complement EP experiments. For example, the alignment of cells by DEP after EP has been used for cell-cell fusion [65], and EP of DEP-trapped cells increased the sensitivity of impedance-based cell-detection [84]. In a spatially non-uniform E , the dependence of EP on the field's amplitude results in position-dependent EP, and therefore leads to regions within the chamber where either reversible or irreversible EP may prevail [85, 86].

1.3.3 Combined dielectrophoresis (DEP) and electro-poration (EP)

The combined use of DEP and EP is dramatically demonstrated by “electro-fusion” (EF) of cells: In this procedure, DEP is used to align cells in pearl-chain formations and subsequent EP results in fusion of two or more cells [65]. DEP has also been used to trap cells prior to impedance measurements and cell-destruction by EP [84]. The cell-type selectivity of DEP permits ED-based genetic modifications or cell-destruction to be performed with cell-type selectivity. Having judged this topic worthy of further research, and in order to demonstrate predictable cell-positioning by DEP, we explored the extent to which reversible or irreversible EP of cells could be controlled by DEP. This combined DEP/EP work is represented by our second published article (Appendix II).

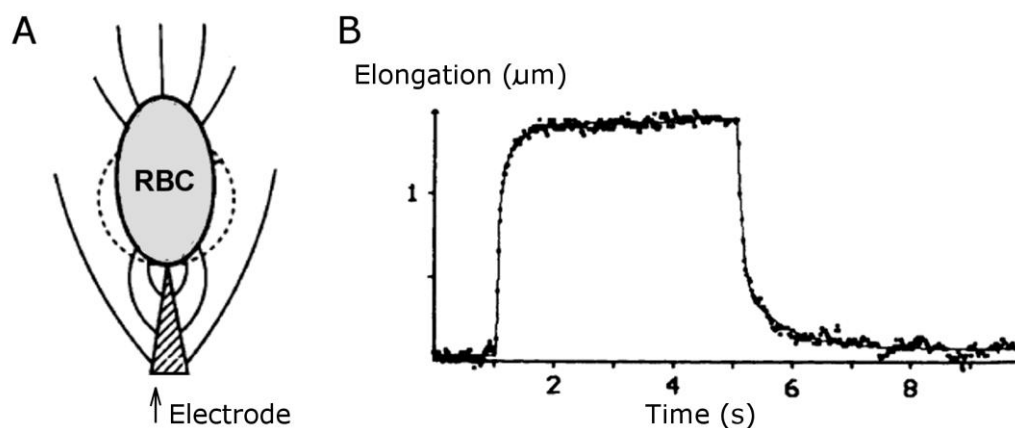


Figure 1.6 Electro-deformation of an erythrocyte (red-blood-cell, RBC). (A) schematic view of a cell (RBC) in an inhomogeneous electric field, E (solid lines); the dotted-line represents the unstained RBC-shape, prior to application of E ; (B) transient elongation of an RBC in response to a step-wise increase in the amplitude of E ; adapted from [47].

1.3.4 Electro-deformation (ED) of cells

Detailed studies of ED were first reported by Engelhardt et al., using RBCs: [36, 47, 87]. In their system, cells were trapped at the edges of “razor”-shaped electrodes by DEP, permitting improved optical observation when compared with circular wires (Fig. 1.6 A). The measured time-dependent strain and relaxation properties of RBCs (Fig. 1.6 B), permitted mechanical characterisation of these cells using simplified mechanical models, which were previously used to describe materials such as polymers [88]. They developed several differing experimental protocols, in which the patterns of applied electrical stresses were varied in amplitude and time using programmable waveforms, thereby demonstrating the versatility of ED.

Work with RBCs was extended by Krueger and Thom (1997) to subzero temperatures ($-15^{\circ}\text{C} < T < 25^{\circ}\text{C}$): They discovered that RBCs could be stretched to nearly twice their original lengths, even at temperatures below 0°C without destruction. This work has been continued recently by some of the same authors [48]. ED has also been reported, on several occasions, by U. Zimmermann and co-workers, among their very extensive electro-

manipulation literature, which includes such topics as: DEP and ER [89], the effects of ED on EP [38], and the effects of ultra-short pulses [90]. They have also reported ED of non-RBC mammalian (murine Sp2 myeloma) cells [46].

More recently, the use of microfabricated electrodes for ED of individual cabbage protoplasts was reported [39]. Surprisingly, most recent review articles that describe methods for mechanical characterization of individual cells did not discuss ED [9, 40], in spite of several important advantages of this technique mentioned in the introduction of this thesis. Furthermore, erythrocytes (RBCs) appear to be the only cell-type for which multiple independent ED measurements have been reported [91]. *ED therefore appears to be underutilized, and the vast majority of mammalian cell-types have not been studied using the ED method.*

Although ED of fluid droplets, vesicles, and RBCs has been well-demonstrated, the potential for mechanical characterisation of diverse mammalian cell-types clearly requires demonstration.

CHAPTER 2. METHODS AND RESULTS

This chapter synthesizes the methods and results, which were presented in three published articles (Appendices I-III); it is divided into a methods section (2.1), and a results section (2.2). A description of the theoretical methods is first provided, in which simplified models of cell-structure were used to predict the major features of cell-positioning by DEP and cell-deformation by ED; this included the use of “Finite Element Methods” (FEM) to simulate the electric field, E . Planar microelectrodes are then described, including their use for generating a fringing, spatially non-uniform E , along with experimental DEP, EP, and ED protocols. Results which are presented in this chapter include combined DEP and EP for cell-type specific genetic modification of cells, and mechanical characterization of two model cell-types by ED (U937 and CHO).

2.1 Methods

2.1.1 Theory

Considerable theoretical work has been developed by others to describe electro-manipulation of cells, using simple cell-geometries such as the roughly spherical one of suspended cells [61, 92-94]. The DEP literature, for example, deals almost exclusively with suspended cells [74], and the basic (dielectric) description of a cell as a spheroid comprising an electrically conductive (aqueous) interior, surrounded by a thin insulating membrane (Fig. 2.1.1 B) is often sufficient to explain DEP phenomena [95].

I will therefore begin the present theoretical description by stating a well-known equation for the DEP force, F_{DEP} , which is exerted on a spherical cell in a non-uniform E . I will then describe the dependence of estimated F_{DEP} -values on experimentally variable parameters. The ED force, F_{ED} , will be derived from a special case of F_{DEP} , in which the dielectric description of the cell can be further simplified to that of a spherical conductor (Fig. 2.1.1 C). A derivation of F_{ED} , based on the Maxwell stress-tensor, will be presented for comparison.

Mechanical properties of cells will be parameterized using two simple models, which are frequently used in the literature. In the three-parameter “standard linear solid” (SLS) model, a single relaxation process characterizes the cell’s strain relaxation, whereas in the two-parameter power-law (PL) model a continuum of relaxation processes is assumed.

2.1.1.1 Calculation of applied electrical stresses

The electrical polarization phenomena described here act on the cell as a whole, and a macroscopic description of polarization and conduction processes is therefore justified. In this framework, a spherical cell of radius r_c has a complex effective electrical permittivity, $\varepsilon_c^* = \varepsilon_c - i\sigma_c/\omega$, where ε_c and σ_c are the electrical permittivity and conductivity of the cell, respectively, $i = \sqrt{-1}$, and $\omega = 2\pi f$ is the angular frequency of the applied potential, U .

In order to represent the basic (dielectric) description of a cell as a spheroid comprising an electrically conductive (aqueous) interior, surrounded by a thin insulating membrane (the CM), “single shell” models have been extensively reported [93-95]. In these models, the internal cytosol and CM are represented by ε_i^* and ε_{CM}^* , respectively, and ε_c^* is evaluated using an adaption of Maxwell’s mixture formula [95]:

$$\varepsilon_c^* = \varepsilon_{CM}^* \frac{\left(\frac{r_c}{r_c - d_{CM}}\right)^3 + 2 \frac{\varepsilon_i^* - \varepsilon_{CM}^*}{\varepsilon_i^* + 2\varepsilon_{CM}^*}}{\left(\frac{r_c}{r_c - d_{CM}}\right)^3 - \frac{\varepsilon_i^* - \varepsilon_{CM}^*}{\varepsilon_i^* + 2\varepsilon_{CM}^*}}, \quad (1)$$

where d_{CM} is the CM-thickness.

When cells are suspended within an aqueous medium, which has a complex electrical permittivity: $\varepsilon_m^* = \varepsilon_m - i\sigma_m/\omega$, differing values of ε_c^* and ε_m^* result in polarization forces. When E is spatially non-uniform, the polarization forces are not balanced spatially, and movement of (unobstructed) cells is observed (Eq. 2, $F_{DEP} \neq 0$). The sign and magnitude of F_{DEP} depend on the relative values of ε_c^* and ε_m^* (Eq. 3), and can therefore be controlled by the experimental variables: f (Fig. 2.2) and σ_m (Fig. 2.3).

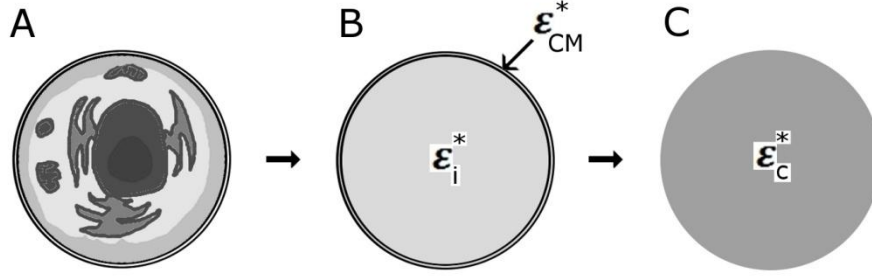


Figure 2.1 Simplified dielectric model of a suspended mammalian cell. (A) Depiction of cell, with various internal structures; (B) complex dielectric permittivities of the internal cytosol, ϵ_i^* , and CM, ϵ_{CM}^* , which are used in the single-shell model; (C) effective permittivity of a cell, ϵ_c , which is used to calculate ED stresses.

The DEP-force acting on a spherical cell of radius r_c in a spatially non-uniform, sinusoidal (time-varying) electric field, E , is given by [95]:

$$\langle F_{DEP}(t) \rangle = \pi r_c^3 K \epsilon_m \nabla |E|^2 \quad (2)$$

where $K = \text{Re}\{K^*\}$ is the real part of the complex (dipole) polarization factor:

$$K^* = \frac{\epsilon_c^* - \epsilon_m^*}{\epsilon_c^* + 2\epsilon_m^*} \quad (3)$$

Values of K are bounded by $-0.5 < K < 1$, and $K < 0$ or $K > 0$ corresponds to observed nDEP or pDEP of cells, respectively (Fig. 2.2). A single “cross-over” frequency, f_0 , defined by $K(f_0) = 0$ and $F_{DEP}(f_0) = 0$, was seen in DEP experiments (described below) when $f < 10^7$ Hz; f_0 can be given by [95]:

$$f_0 = \frac{1}{2\pi} \left[\frac{(\sigma_m - \sigma_c)(\sigma_c + 2\sigma_m)}{(\epsilon_c - \epsilon_m)(\epsilon_c + 2\epsilon_m)} \right]^{\frac{1}{2}} \quad (4)$$

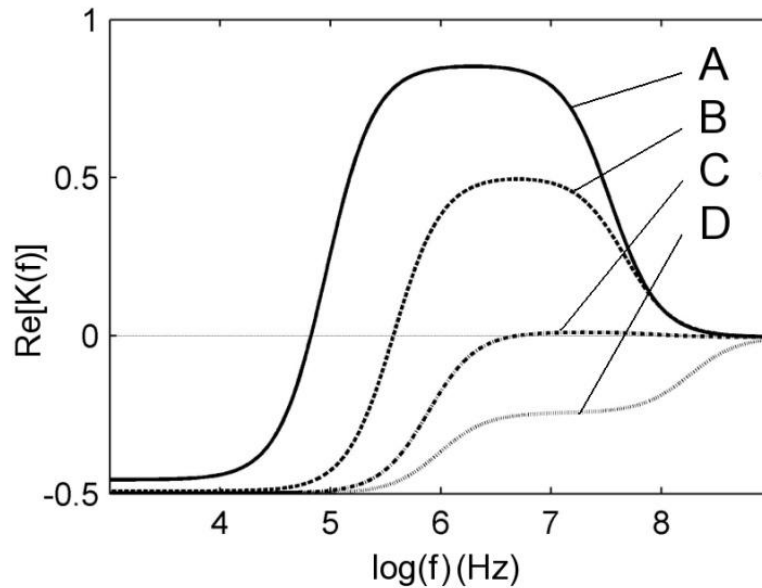


Figure 2.2 The real part of the (dipole) polarization factor for U937 monocytes. $\text{Re}[K(f)]$ in Eq. 3, versus frequency, f , for model parameters corresponding to U937 monocytes and at different values of σ_m (S/m), A: 0.02; B: 0.1; C: 0.4; and D: 1.0; image is from Appendix II.

To fit measured f_0 -values with those estimated using Eq. (3), the differences between measured and calculated values of f_0 were minimized using a least-squares algorithm (lsqcurvefit, Matlab v. 7.2, The Mathworks, Natick, MA). By measuring f_0 -values as a function of σ_m , the dielectric properties of U937 monocytes were estimated, which permitted theoretical plots of $K(f)$ corresponding to these cells (Fig. 2.2). In order to estimate ϵ_{CM} and σ_i , f_0 data were fit using both Eq. (3) (with the condition $K(f_0) = 0$) and Eq. (4), by varying ϵ_m and σ_i , with the other parameters fixed at $r_c = 7.5 \mu\text{m}$, $d_{CM} = 7.0 \text{ nm}$, $\sigma_{CM} = 10^{-6} \text{ S m}^{-1}$ and $\epsilon_i = \epsilon_m = 80\epsilon_0$, where $\epsilon_0 = 8.85 \times 10^{-12} \text{ F/m}$ is the vacuum permittivity. Our estimation of these values facilitated the proper choice of $\sigma_m = 10 \text{ mS/m}$ and $f = 5 \times 10^6 \text{ Hz}$, for effective pDEP and maximal ED forces.

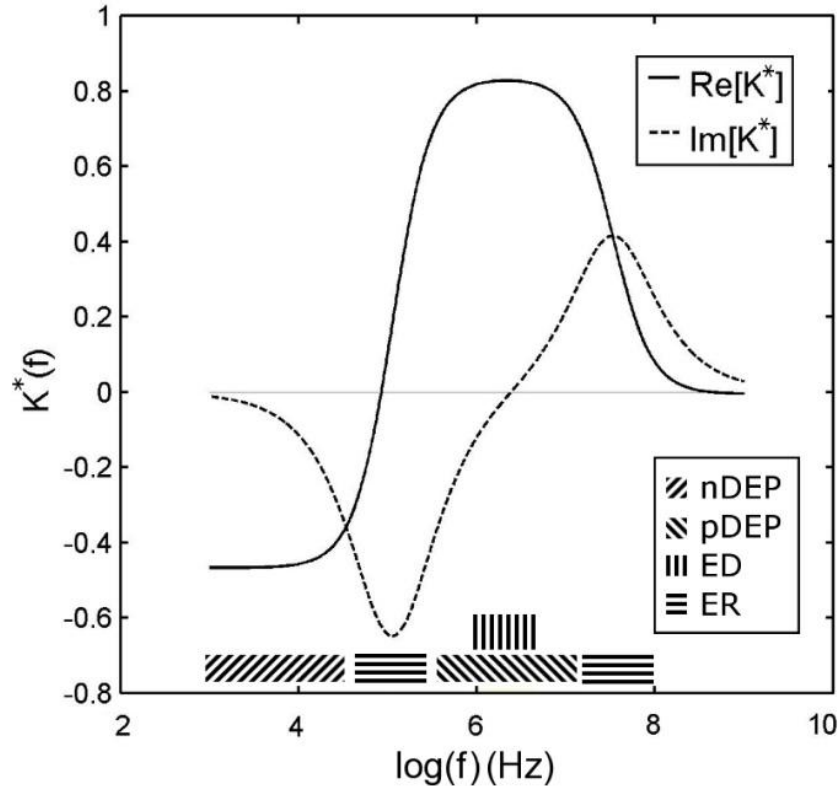


Figure 2.3 Frequency-dependent plots of the complex polarization factor for **U937 monocytes**. The real and imaginary parts of K^* , $\text{Re}[K^*]$ (solid line) and $\text{Im}[K^*]$ (dotted line), respectively, are plotted as a function of the frequency, f , of the applied electric potential, U . Various ranges of f -values, in which nDEP, pDEP, ED, or ER of cells are observed, are indicated by hatched areas above the f -axis; $\sigma_m = 10$ mS/m was assumed.

Using low-conductivity media ($\sigma_m = 10$ mS/m), three distinct f -regimes were observed: (i) At low f ($f < \sim 10^5$ Hz, in the present cases), nDEP of cells was observed; (ii) at intermediate f (10^6 Hz $< f < 10^7$ Hz), σ_i was dominant compared with σ_m , and pDEP (and ED) were observed; at high f ($f > \sim 10^7$ Hz), similar ϵ -values of the cytosol and the suspension medium (both aqueous) resulted in negligible force. The three operating regimes outlined above have been previously described in detail by others [38, 70].

For ED experiments, in which $\sigma_m = 10$ mS/m and $f = 5 \times 10^6$ Hz, the σ_i -term is dominant in Eq. (3), and the electrical stresses can be calculated in the quasi-electrostatic regime [47]. Equation (2) can be written in one dimension as:

$$\langle F_{DEP}(x, t) \rangle_t = 4\pi r_c^3 K \varepsilon_m |E_{rms}(x)| \frac{d}{dx} |E_{rms}(x)|, \quad (5)$$

and the following approximation for $E(x)$ used:

$$\langle |E_{rms}(x)| \rangle = 0.7E, \quad (6a)$$

$$\langle \frac{d}{dx} |E_{rms}(x)| \rangle = n \frac{E}{r_c}, \quad (6b)$$

where $E = U/d$ is the peak magnitude of the electric field, with U being the applied potential and $d = 50$ μm , the electrode gap; n is a geometry- and material property-dependent factor, and r_c is the cell radius. Good estimates of E during ED are $E = 4 \times 10^4$ V/m during trapping ($U = 2$ V), and $E = 2 \times 10^5$ V/m during stretching ($U = 10$ V). The approximations in Eq. (6) result in the following expression for the force on each half-sphere:

$$F = \pm 2\pi r_c^2 n K \varepsilon_m E^2, \quad (7)$$

The average value of stress, ζ , on the surface of the sphere can then be found by dividing Eq. (7) by the half-cell area:

$$\langle \zeta \rangle = n K \varepsilon_m E^2. \quad (8)$$

The non-uniformity of E near the “trapping” electrode tip (discussed below in Sect. 2.1.2) was found to be of the same order of magnitude as that induced around a typical cell: $d/dx(E) \sim 1.5E/r_c$ ($n \sim 1.5$ in Eq. 6b). Assuming a maximum value of $K = 1$ (Fig. 2.3) and $r_c = 7.0$ μm (measured optically), Eq. (8) yields $\langle \zeta \rangle = 0.85$ Pa during trapping ($U = 2$ V), and $\langle \zeta \rangle = 21.2$ Pa during stretching ($U = 10$ V).

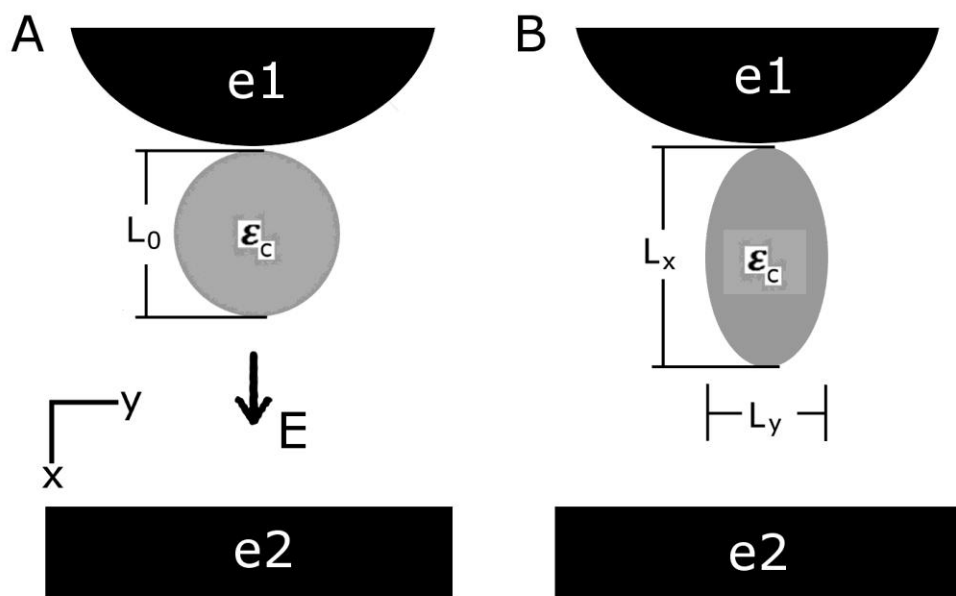


Figure 2.4 Simplified model of cell-deformation. (A) Spherical cell of length, L_0 , and electric permittivity, ϵ_c , trapped between two electrodes, e_1 and e_2 , which have differing curvatures; x - y coordinates and the direction of the electric field, E , are shown; (B) deformed cell with lengths, L_x and L_y .

Mechanical strain, γ , in the directions parallel or perpendicular to E (γ_x and γ_y , respectively) are both calculated as:

$$\gamma(t) = \frac{L(t) - L_0}{L_0}, \quad (9)$$

where $L(t)$ is the length of the cell at time, t , and L_0 was the original length. The apparent Poisson's ratio of the cell is then given by: $\nu = -\gamma_y/\gamma_x$.

Mechanical behaviour of “simple” solids, for example viscoelasticity, involves the (linear) relationship between an applied stress, ζ , and the resulting strain, γ ; the material-specific property linking the two is known as the solid's compliance, J [88]:

$$\gamma = \zeta J \quad (10)$$

In other words, J is the strain per unit stress, and it is a measure of the solid's “stiffness”.

2.1.1.2 Viscoelastic properties (SLS model)

The simplest “lumped-parameter” viscoelastic model, which fits our ED-data reasonably well, is the three-parameter standard linear solid (SLS) model, characterized by two elastic constants, k_1 and k_2 , and one viscous constant, η . In a well-known mechanical analog, the so-called Zener model, these correspond to a parallel combination of a spring (k_1) with a series combination of a second spring (k_2) and a dashpot (η). The compliance function, $J(t)$, now describes the time-dependent response of the material to an applied time-varying ζ , in terms of these model parameters. For the SLS, $J(t)$ is given by [103]:

$$J(t) = \frac{1}{k_1} \left[1 - \left(\frac{k_2}{k_1 + k_2} \right) e^{-t/\tau_\zeta} \right] \mathbf{1}(t), \quad (11)$$

where $\mathbf{1}(t)$ is the unit step function and τ_ζ is the time-constant (or “relaxation time”) at constant stress:

$$\tau_\zeta = \eta \frac{(k_1 + k_2)}{k_1 k_2}. \quad (12)$$

In response to a step-wise (either increasing or decreasing) change in ζ , the SLS model predicts (i) an instantaneous change in J , $J(t = 0) = J_0 = 1/(k_1 + k_2) = 1/E_0$, where E_0 is the initial elastic modulus; (ii) a limiting value of J , $J(t = \infty) = J_\infty = 1/k_1 = 1/E_R$, where E_R is the relaxed elastic modulus; and (iii) a single time-constant, τ_ζ , given by Eq. (12), which determines the relaxation time.

2.1.1.3 Power-law model

A power-law can also be used to model $J(t)$, as was done previously by others for uniaxial stretching of single C2-7 cells, derived from skeletal muscle of adult CH3 mice [96]:

$$J(t) = At^\alpha, \quad (13)$$

where A and α are constants. The power-law has been proposed as a general fitting procedure, which considers the cell to be a material with a continuum of relaxation times. The parameters, α and A , can be related to the low-frequency storage modulus, $G'(\omega)$, using the following equation [96]:

$$G'(\omega) = \left(\frac{\cos(\alpha\pi/2)}{A\Gamma(1+\alpha)} \right) (2\pi f)^\alpha, \quad (14)$$

where Γ is the gamma function and f is the frequency.

Strain data were fit using Eq. (10), with the stress ζ given by Eq. (8), and the material's compliance function $J(t)$ given by either Eq. (11) or Eq. (13). The differences between measured and calculated values of γ were minimized using a non-linear least-squares algorithm (lsqnonlin, Matlab v. 7.2).

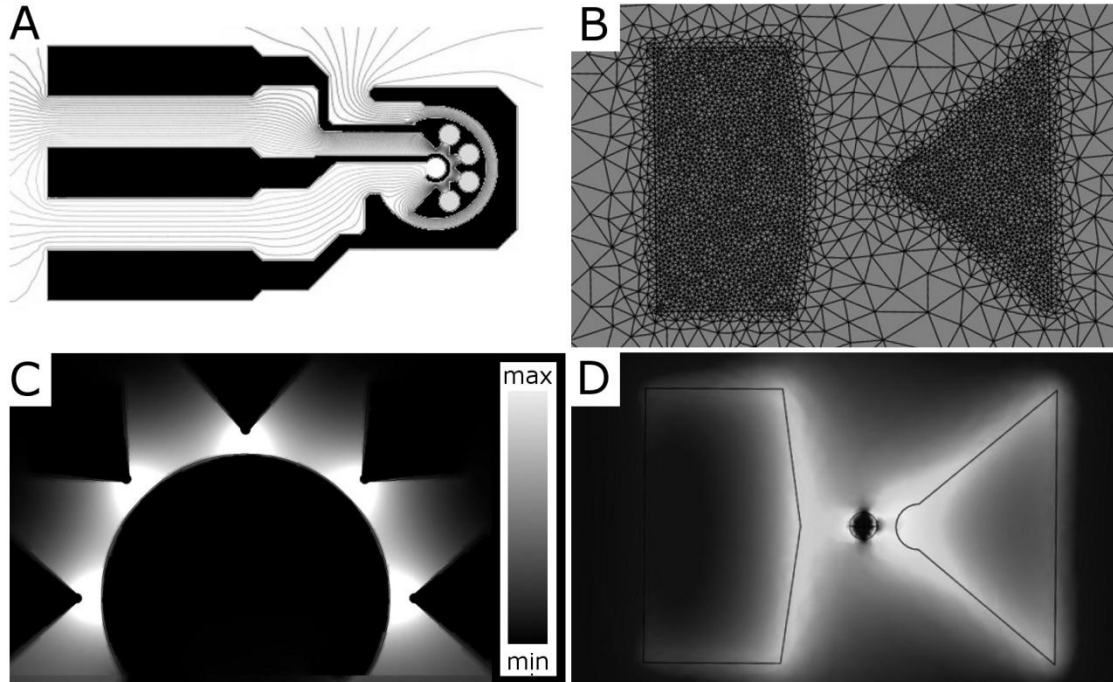


Figure 2.5 Finite-element simulations of E. (A) A 3-lead electrode set, with simulated equipotential lines shown in grey; (B) Simplified structure used for 3D simulations; course mesh setting is shown; (C) periodic variation of E, resulting from periodic variation of inter-electrode distance; electrodes are shown in black; arbitrary scales of length and E; (D) simulated strength of E in the presence of a spherical polarisable object, using the simplified geometry shown in (B).

2.1.2 Finite element methods (FEM)

Estimates of E were accomplished with Comsol Multiphysics v3.2 software (Comsol, Stockholm, Sweden) using the conductive media mode with the electric potential assigned at boundaries (Dirichlet-type of boundary conditions), and assuming a homogeneous medium in which the presence of cells was neglected.

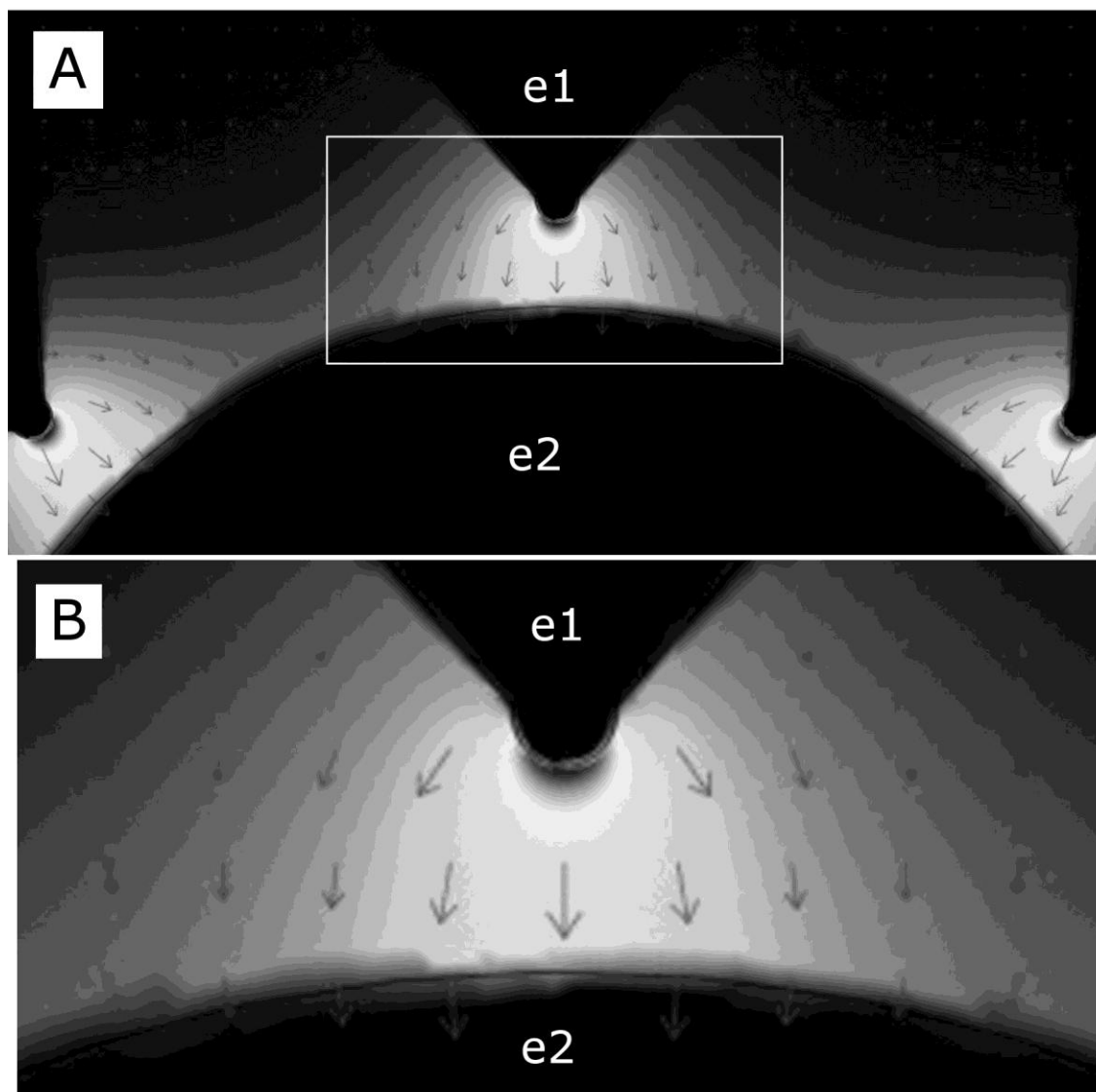


Figure 2.6 Finite-element simulations of E, magnified view. (A) Strong E-values (white) were designed to attract cells by pDEP; electrodes, e1 and e2, are shown in black; the outlined area in (A) is magnified in (B); (B) near the rounded tip of the “trapping” electrode, e1, uniaxial cell-stretching is predicted; length and direction of arrows indicate strength and direction of E.

The non-uniform E (Figs. 2.5, 2.6) was designed to capture individual cells at each electrode tip. In this region (Fig. 2.5 D) values of E surrounding a polarized cell are high near the cell-poles and low near the equator. For the case of a uniform applied E, the radial component of the induced dipole field has an angular dependence that is proportional to $\cos\theta$ (see Appendix

III). In the present (non-uniform) case, E is highest near the cell-pole that faces the electrode tip, and cells are therefore trapped in this region. We define positions within $50\ \mu\text{m}$ of the electrode edges as strong- E regions, and otherwise as weak- E . The values of E averaged over the strong and weak regions differ by a factor of approximately three. For example, when the applied voltage was $U = 10\ \text{V}$, the maximum value of $E = U/l$, where l is the inter-electrode distance, is $200\ \text{kV m}^{-1}$. The E values averaged over the strong- and weak- E regions are $\sim 180\ \text{kV m}^{-1}$ and $\sim 60\ \text{kV m}^{-1}$, respectively, as already pointed out above.

2.1.3 Microfabrication of electrodes

Planar Ti/Pt electrodes were fabricated on glass substrates using standard lift-off processes [50]: Chromium masks were fabricated on glass (Bandwidth Foundry, Sydney, NSW, Australia) and photolithography was carried out by spin-coating an adhesion promoter, AP300 (Silicon Resources, Chandler, AZ), a lift-off resist LOR5A (MicroChem, Newton, MA) and a final, positive, resist S1813 (Shipley, now part of Rohm & Haas, Philadelphia, PA). UV exposure was done using a Karl Süss MA-4 mask aligner (Süss Microtec, Waterbury Center, VT). The electrodes were deposited by electron beam evaporation (Ti adhesion layer, $10\ \text{nm}$) and sputtering (Pt layer, $70\ \text{nm}$), the former under ultra-high-vacuum and the latter in Argon at $2.4\ \text{Pa}$. For each glass slide (dimensions: $76.2 \times 25.4 \times 1.5\ \text{mm}$), the lift-off procedure produced 12 sets of electrodes, each with three leads (Fig. 2a) to which electrical connectors were bonded using a combination of conductive silver epoxy (MG Chemicals, Surrey, BC, Canada) and a standard two-phase epoxy (LePage, Toronto, ON, Canada).

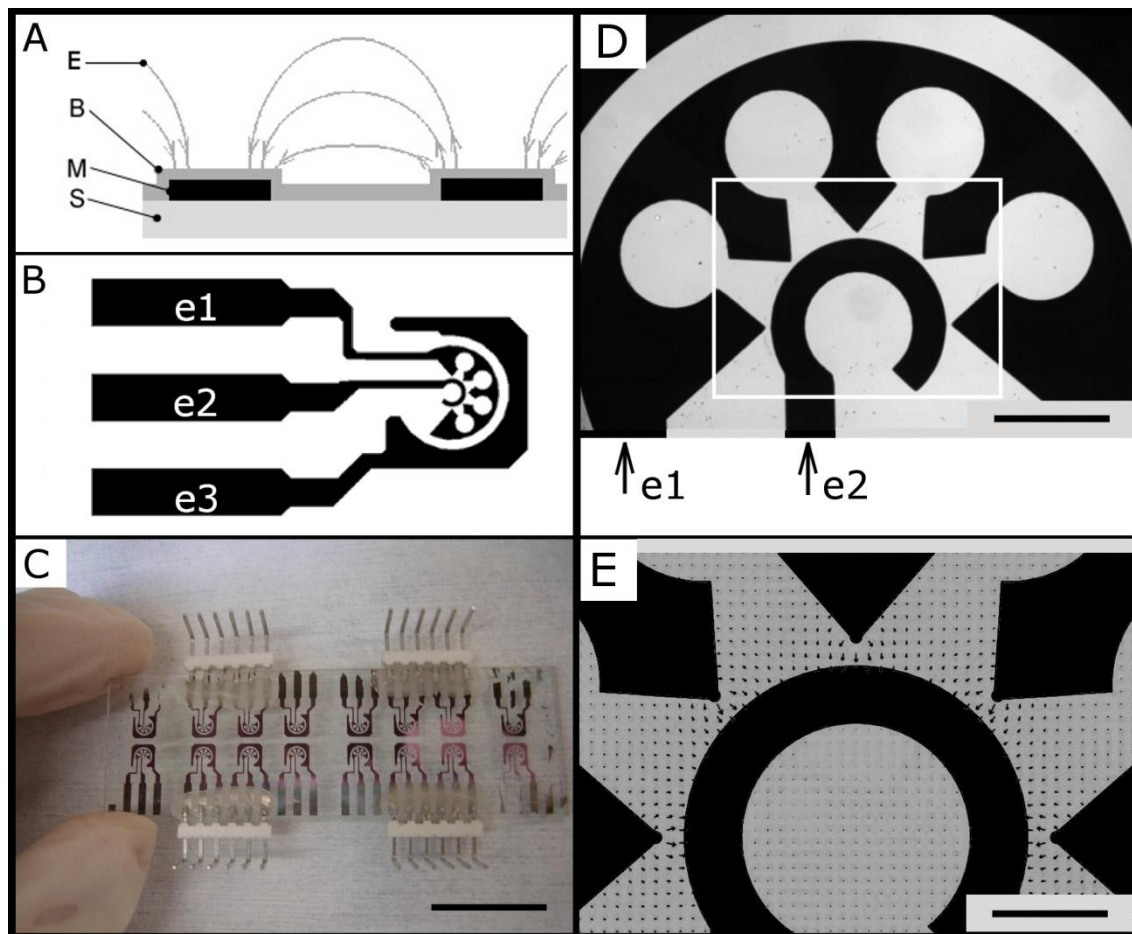


Figure 2.7 Ti/Pt electrodes deposited on a glass microscope slide. (A) Fringing electric field, E, barrier, B, metallic conductor, M, and substrate, S; (B) One 3-lead electrode set with electrodes labelled e1, e2, and e3. The inner two electrodes, e1 and e2, are driven at opposite polarity, while the outermost electrode, e3, is grounded; (C) microscope slide with multiple 3-lead electrode sets; scale bar = 2.5 cm; (D) Magnified view of the inner two electrodes, e1 and e2; scale bar = 500 μm ; the rectangular trace represents the region used for DEP and is magnified in (E); (E) the strength and direction of the simulated E, indicated by the lengths and directions of arrows: Strong- and weak- E regions occur where e1 approaches and recedes from e2, respectively; scale bar = 200 μm .

Thin films (~ 550 nm) of hydrogenated silicon nitride (SiN_xH , a clear, transparent dielectric) were deposited over the electrodes by plasma-enhanced chemical vapor deposition (PECVD), to prevent electrolysis of the suspension medium during ED, and to enable multiple reuses of the devices. For this, the slides were placed on the grounded electrode of a “Reinberg”-type parallel plate radio-frequency (RF, 13.56 MHz) PECVD reactor, in a flowing gaseous mixture of silane (SiH_4) and ammonia (NH_3): The flow-rates and partial pressures were (SiH_4 : 2.5 sccm, 12 mTorr) and (NH_3 : 25 sccm, 43 mTorr), and the total pressure was maintained at 55 mTorr. The power delivered to the plasma was 50 W (the power density at the surface of the grounded electrode was ~ 150 mW/cm²), and the substrate temperature was maintained at 125 °C. The deposition time was 45 minutes and film-thickness, measured by variable-angle spectroscopic ellipsometry (VASE, J. A. Woollam & Co., Lincoln, NE), was 550 ± 25 nm. We have previously described the operation of this PECVD system in more detail, albeit for the case of depositing thin films of a semi-conductor, nano-crystalline silicon (Appendix I).

2.1.4 Cell culture

Murine fibroblasts (L929), Chinese hamster ovary- (CHO), human embryonic kidney- (HEK293), and human monocytic- (U937) cells were obtained from ATCC (Manassas, VA). L929 were cultured in DMEM (Sigma, St. Louis, MO), CHO in HAM-F12 (Sigma), HEK293 in DMEM (Sigma), and U937 in RPMI 1640 (Sigma), all supplemented with 10% fetal bovine serum (FBS; Atlanta Biologicals, GA). All cell types were incubated at 37°C, in an atmosphere supplemented with 5% CO_2 . U937 were cultured in suspension, and the other three cell-types were cultured in monolayers. Adherent cell-types (L929, CHO, and HEK293) were detached prior to ED by replacing the culture medium with ED buffer (described in Sect. 2.1.6) + 0.5% trypsin. All cells used for ED were selected during the third and fourth weeks of culture, namely passage Nos. 8-12 for the U937 cells and Nos. 6-8 for CHO cells, to ensure that they were healthy and proliferating normally.

2.1.5 Cell-viability tests

We used a “Live(green)/Dead(red)” cytotoxicity kit (Invitrogen, Carlsbad, CA) to visualize the position-dependence of EP. The protocol consists of adding a mixture of two different fluorescent indicators, each at 1 μM concentration, to the cell suspension. The first indicator, Calcein AM, can enter through the cell membrane and then be cleaved by esterases in healthy cells to become fluorescent (green). The second indicator, Ethidium HD-1, is excluded from healthy cells with intact cell membranes, but traverses those that have been compromised; once inside the nucleus, it binds to nucleic acids, which greatly ($40\times$) increases its fluorescence (red). Thus, healthy cells appear green, irreversibly damaged cells red, and reversibly electro-porated cells appear orange due to the combined presence of both indicators.

2.1.6 Cell-suspension medium

The medium used for ED experiments (EDM) was an isotonic buffer with low electrical conductivity, $\sigma_m = 10 \text{ mS/m}$, (EDM: 3.4 mM NaCl, 0.115 mM KH_2PO_4 , 280 mM D-Glucose); pH was adjusted to 7.3 ± 0.1 with NaOH and the osmolality was 285 mOsm/kg. Low electrical conductivity was required to maximize ED stretching forces, as previously described by others [36-38]. Cell-viability tests (“Live/Dead”, see above) showed no observable differences for either CHO or U937 cells, which were suspended in EDM for up to 30 minutes, compared with tests performed in media with roughly physiological σ (PBS, $\sigma \sim 1.5 \text{ S/m}$). For ED experiments, exposure of cells to EDM was limited to 10 minutes. The use of low- σ media also reduces electrical conductivity-generated (“Joule”) heat, which scales with σ (see section 3.7 of [97]). In the present work, the maximum temperature increase of the suspension during ED was estimated to be less than 1 $^\circ\text{C}$. Prior to ED experiments, cells were centrifuged at 190g for five minutes at moderate cell densities ($\sim 10^6$ cells/mL) and re-suspended in EDM at low densities ($\sim 1.5 \times 10^4$ cells/mL), as measured by hemocytometer. Low densities were used for ED in order to facilitate the capture of individual cells and to minimize undesirable effects arising from too many neighbouring cells. However, cell density could readily be increased depending on the required number at each electrode tip (10^4 cells/mL led to ~ 1 cell/tip). Cells suspended in EDM were deposited over the electrode surface in 5 μL droplets (total cell number ~ 50 -250).

2.1.7 Electro-manipulation of cells

The electrodes were placed within the microscope slide-carrier of an inverted optical microscope (AxioVert S100TV, Carl Zeiss Microimaging, Thornwood, NY) and connected to a signal generator (Model 33220A, Agilent, Palo Alto, CA), which was used to generate both sine waves for DEP and square pulses for EP, without the requirement for any additional signal conditioning or amplification. During DEP manipulations, the central electrode was driven at opposite polarity to the surrounding structure (Fig. 2.7 D, e2 and e1, respectively).

2.1.7.1 Dielectrophoresis (DEP)

For f_0 measurements, cells were suspended in buffer at a density of $\sim 5 \times 10^5$ cells/mL, as measured by hemocytometer (VWR Scientific, Mississauga ON), and were transferred in 7.5 μ L volumes to the electrode surface using a micropipette. This produced a ~ 250 μ m deep liquid layer containing ~ 3750 cells, which covered an area of ~ 30 mm². The DEP signal applied to the electrodes was a sine wave with a peak voltage of $U = 3$ V, and a frequency sweep $10^4 < f$ (Hz) $< 10^7$ was performed for each value of σ_m . Cell behavior was monitored visually or with a CCD camera (Model QIC-F-/M2: QImaging, Burnaby, BC, Canada), and still images were captured for subsequent analysis. Under these conditions, the majority of cells attained equilibrium positions along the plane of the electrodes after about five minutes, by a combination of DEP and sedimentation, at which point the experiment was terminated. Cell-positioning statistics were then compiled from the image by counting the cells that had migrated to strong-E regions (where the distance between cells and electrode edges was < 50 μ m), versus weak-E regions (where the distance between cells and electrode edges was > 50 μ m).

Under certain conditions with appropriate choices of f and σ_m , F_{DEP} was found to be negligible, and cells remained randomly distributed over the electrode surfaces. As described above, the corresponding f values are the “cross-over” frequencies, f_0 , and a different value of f_0 was found for each value of σ_m . To determine f_0 , we repeated the positioning experiments at different f values, until random distributions of cells were observed, approaching f_0 from frequencies both above and below f_0 in order to minimize error. This procedure was repeated three times for each σ_m .

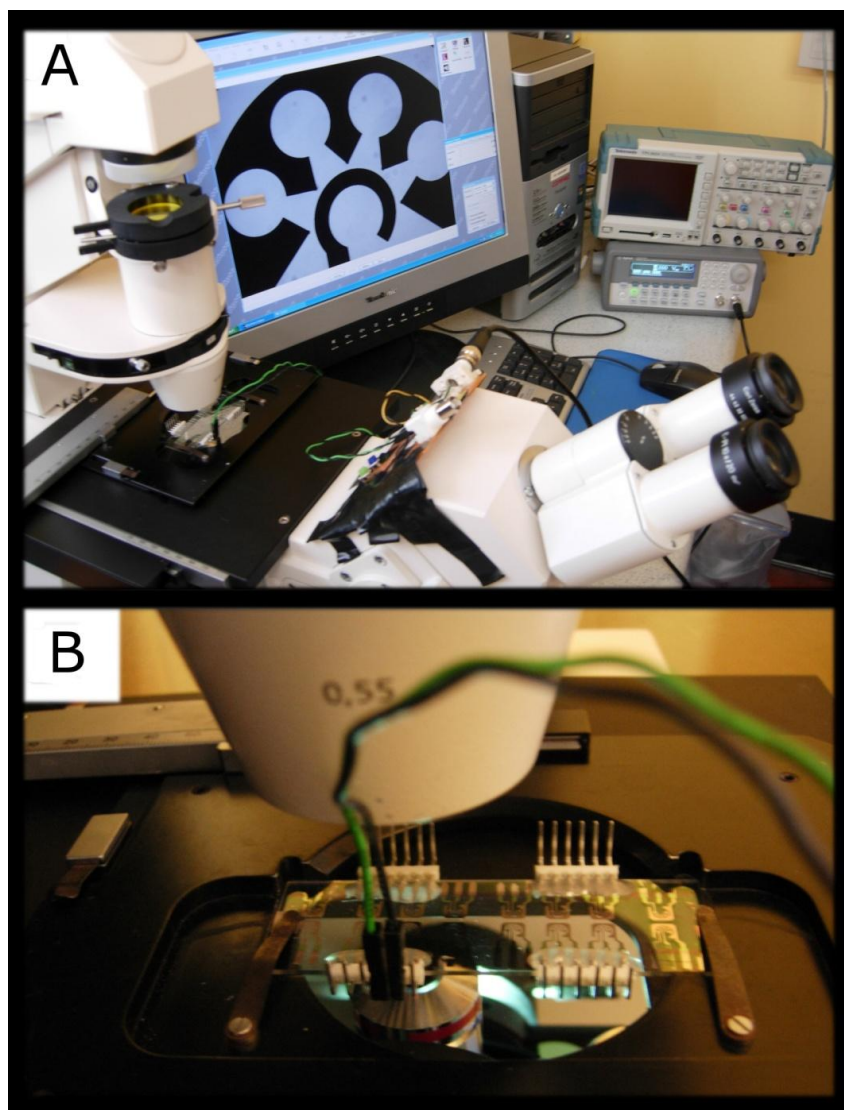


Figure 2.8 Microscopy system used for ED. (A) Inverted optical microscope with computer, oscilloscope, signal generator, and microelectrodes; (B) Magnified view of the microelectrode platform, which is loaded within a standard microscope slide-carrier.

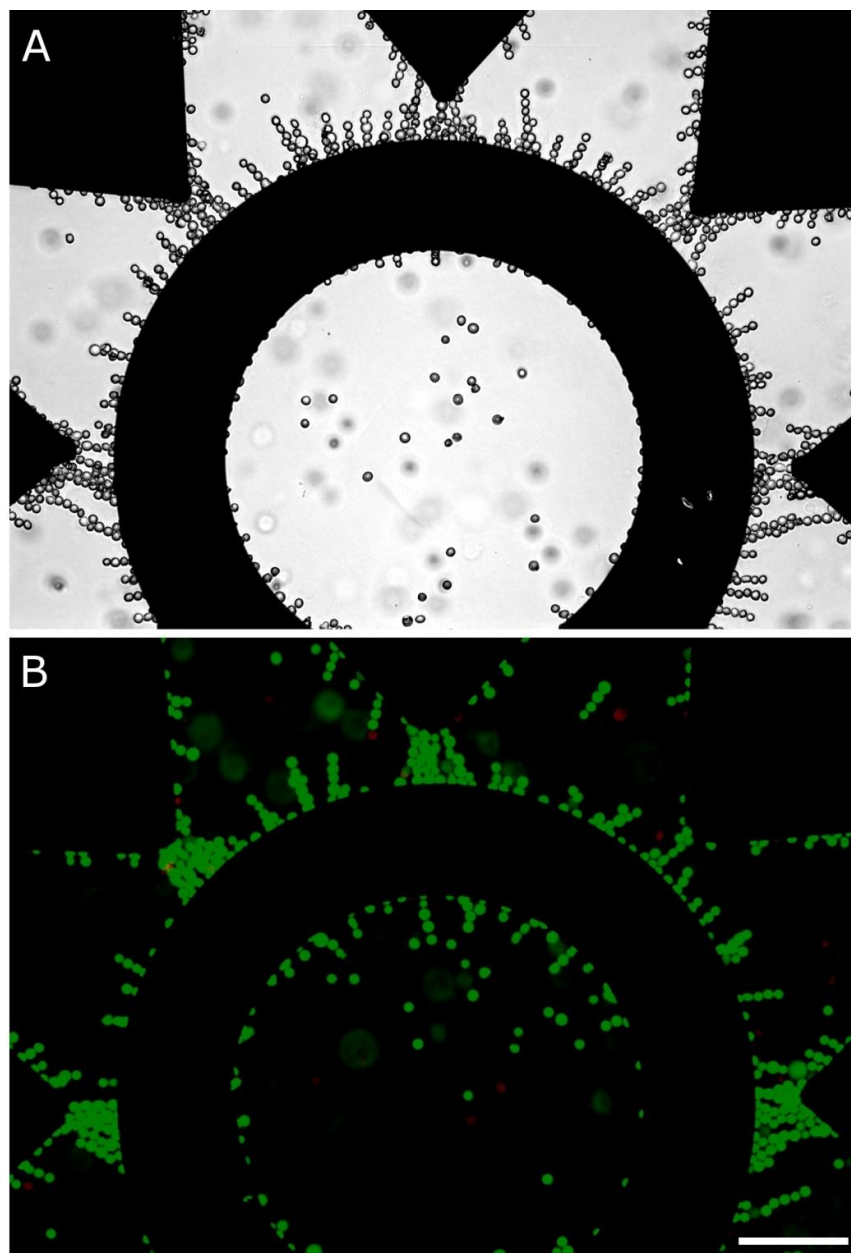


Figure 2.9 Cell-viability during DEP. (A) U937 monocytes trapped in the high-E regions by pDEP; (B) the same cell-type and pDEP conditions as in (A), all cells remain green during “Live/Dead (green/red)” viability tests; scale bar = 100 μm .

2.1.7.2 Electroporation (EP)

We used square-wave electric pulses for EP. For each experimental condition, a sequence of six pulses was applied: Pulse-widths were 20 μs , rise- and fall times were 5 ns, and the inter-pulse interval was 0.5 s. Peak applied voltages were $U = 7, 8, 9, \text{ and } 10 \text{ V}$. First, EP of randomly-distributed cells was examined in the presence of fluorescent probes, to visualize the spatial dependence of EP in the case of a non-uniform electric field. Cell-positioning by DEP was used to accentuate this position-dependence of EP and further influence gene-transfer. Expression of the transferred genes and cell viability (cell-survival) were quantified by determining the ratios N_T/N_{TOT} and N_S/N_{TOT} , N_T being the number of transfected cells, N_S the number of surviving cells, and N_{TOT} the total number of cells.

For gene-transfer we used a DNA plasmid expressing a fluorescent reporter, pEGFP_{Luc} (Clontech, Mountain View CA), at a concentration of 0.55 $\mu\text{g/mL}$. As above, 7.5 μL of buffer containing cells and DNA were placed over the electrodes at a cell density of $D = 5 \times 10^5$ cells/mL (total number of cells ~ 3750). The buffer was PBS diluted in DI- H_2O , with conductivity $\sigma_m = 50 \text{ mS/m}$, and osmolality = $200 \pm 25 \text{ mOsm/kg}$. Transfection experiments were performed at room temperature (27 $^\circ\text{C}$, or 300 K) under four sets of conditions: (i) EP pulses were applied after the cells had been positioned by pDEP for five minutes, using a 3 V, 1 MHz sinusoidal potential; (ii) EP pulses were applied after five minutes of nDEP positioning, using a 3 V, 40 kHz sinusoidal potential; (iii) EP pulses were applied after five minutes of sedimentation only (“no DEP”); and (iv) as a control with neither DEP nor EP pulses. Each condition (i) to (iv) was repeated four times. Following gene transfer, cells were incubated in FBS-supplemented RPMI growth medium at 37 $^\circ\text{C}$ with 5% CO_2 . The number of transfected cells, N_T , and surviving cells, N_S , were monitored by fluorescence microscopy.

2.1.7.3 Electrodeformation (ED)

For ED experiments, a sinusoidal potential, U , of frequency, $f = 5 \times 10^6 \text{ Hz}$, was applied and the amplitude was modulated during ED: $U = 2 \text{ V}$ (peak-to-peak) was used to capture and hold cells (Fig. 2.10 A-C), and $U = 10 \text{ V}$ (peak-to-peak) was used to deform cells at constant stress (Fig. 2.10 D-F). Images were captured with a CCD camera (Model QIC-F-/M2, QImaging, Burnaby, Canada) at a rate of approximately one frame per second, during ED experiments, and saved for subsequent analysis using commercial software (Northern Eclipse v.7, Empix Imaging,

Mississauga, Canada). For healthy (untreated) cells, $U = 10 \text{ V}$ was applied for 60 image-frames (total time $\sim 70 \text{ s}$) before being reduced to $U = 2 \text{ V}$. For damaged cells, which had been treated with CSK-disrupting toxins, $U = 10 \text{ V}$ was applied for only 30 frames ($\sim 35 \text{ s}$) before being reduced to $U = 2 \text{ V}$ in order to limit excessive damage to the cells.

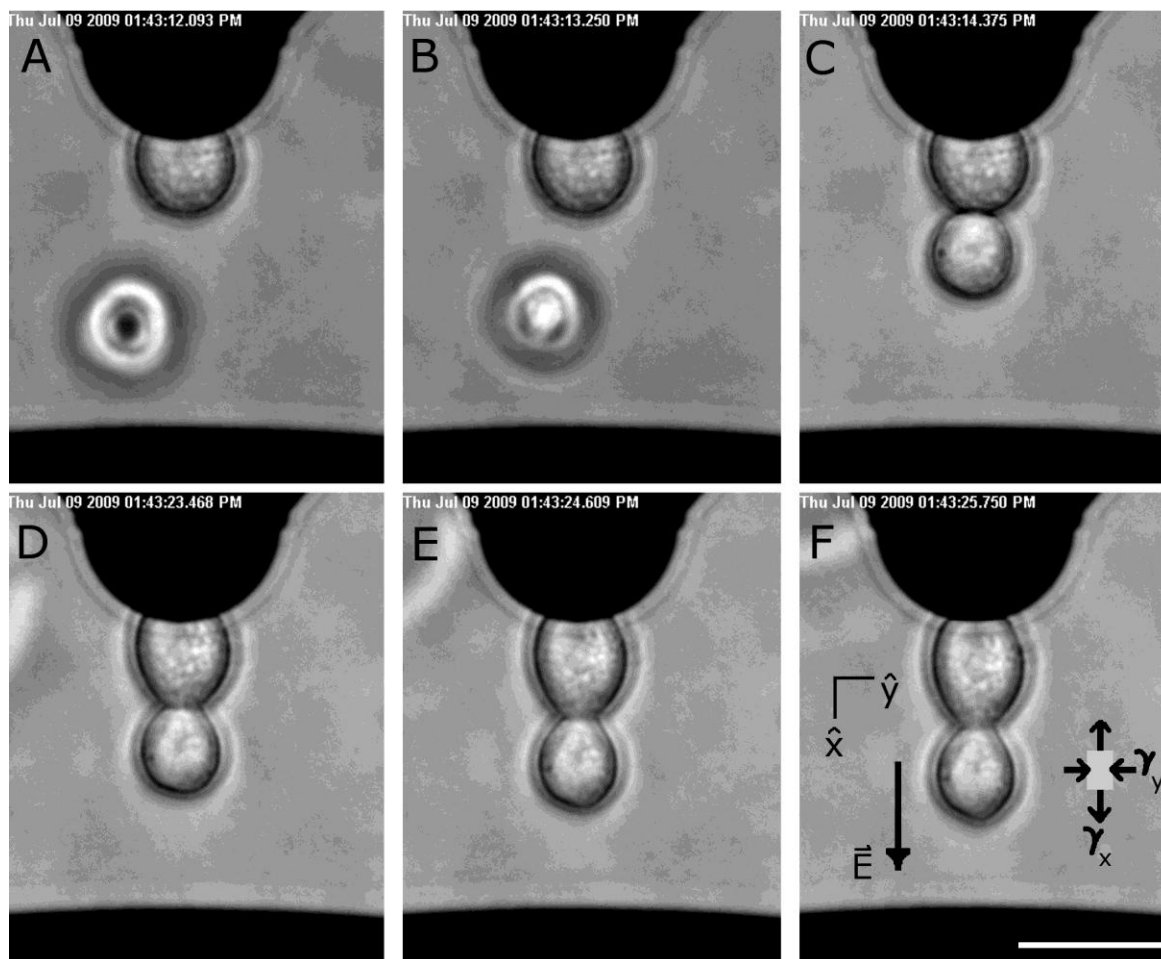


Figure 2.10 Trapping and stretching of U937 cells. The applied electric potential was $U = 2 \text{ V}$ for trapping (A-C), and $U = 10 \text{ V}$ for stretching (D-F). The time delay between each image frame was $\sim 1 \text{ s}$, and the scale bar is $25 \mu\text{m}$. The direction of the electric field, \vec{E} , and strain components, γ_x and γ_y , are indicated in (F).

2.1.8 Disruption of the U937-cytoskeleton

In order to more clearly assess the influence of MF and IF CSK structures on the measurable mechanical properties of individual mammalian cells, U937s were chosen as a model cell-type and their MFs and IFs were disrupted by latrunculin-A (Lat-A) or acrylamide (ACR) treatments, respectively. Mechanical properties of untreated (control) cells were then compared to Lat-A or ACR -treated cells.

Latrunculin-A inhibits actin polymerization by sequestering G-actin [99], which impairs the cell's ability to remodel and repair MFs and leads to degradation of the CA, in a time-dependent manner. We used 10 μ M Lat-A for 2, 3, and 4 h; these conditions showed the largest change in measured strain values attainable without causing significant loss in cell viability. Lat-A was dissolved in 100%-ethanol and diluted in RPMI to yield 20 μ M stock solutions. The stock and cell solutions were combined at equal volumes (0.5 mL each) for a total volume of 1 mL/well, and incubated at 37 °C for the indicated times; cell-density was 5×10^5 cells/mL.

The specific interaction mechanisms and effects of acrylamide (ACR) in cells are not as well documented as for Lat-A, but several reports have established ACR-induced disruption of vimentin-based IFs [100-102]. Higher concentrations of ACR were required, compared with Lat-A: Using 10 mM ACR for treatment times between 0 and 15 h, we observed changes to the ED-properties of cells that were similar to the Lat-A treatments (10 μ M Lat-A for 0-4 h). Exposure of cells to ACR at 10 mM for $t > 15$ h led to loss in cell-viability.

2.1.9 Confocal microscopy

Increased fragility of Lat-A- and ACR- treated cells required minimal cell-agitation during preparation for imaging; washing was therefore done by sedimentation rather than centrifugation. Cells were suspended in 1 mL volumes at the moderate density of $\sim 10^6$ /mL in 2 mL chambers (LabTek) and they were allowed to sediment for 5-10 minutes at 37 °C. The majority of the culture medium ($\sim 90\%$) was then aspirated and replaced by -20 °C acetone for simultaneous permeabilization and fixation of the cells. After 5 minutes, the acetone was aspirated and replaced by phosphate-buffered saline (PBS: 8.10 mM Na₂HPO₄, 1.47 mM KH₂PO₄, 137 mM NaCl, and 2.68 mM KCl, pH 7.4). Following washing and fixation, the cell density was $\sim 10^5$ /mL. We then incubated the cells with monoclonal anti-vimentin Cy3 (Sigma) and alexa-488-phalloidin (Invitrogen) for 45 min at 37 °C, followed by sedimentation-based

washing (three times), for a final cell density of $\sim 10^4$ /mL. Cells were then dispersed in 0.2 mL droplets (containing ~ 2000 cells) within glass-bottom chambers (Mattek) and fluorescence imaging was carried out using an LSM 510 META Axioplan 2 confocal laser scanning microscope with a C-Apochromat 40X/1.2 water immersion objective (Carl Zeiss, Jena, Germany).

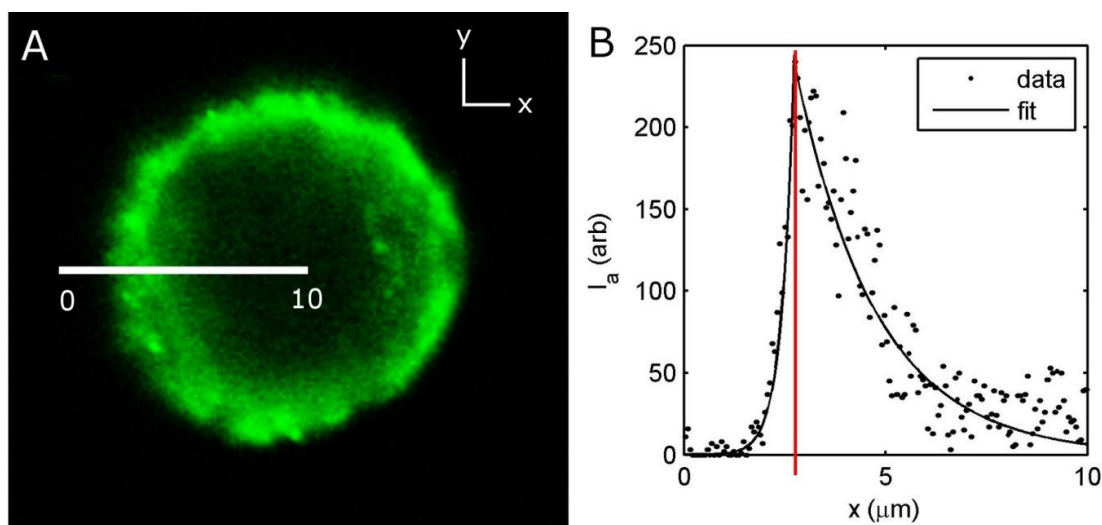


Figure 2.11 Fluorescence intensity of actin labeled with Alexa-488-phalloidin. (A) View of cortical actin in the XY-plane, through the center of a single L929 cell; fluorescence intensity, I_a , was measured through the cortex as indicated by the white line (from 0 to 10 μm); (B) I_a -values (arbitrary scale); the maximum value of $I_a = 240$ occurred at $x = 2.75 \mu\text{m}$, as indicated by the line in (B); data were fitted by two exponential decays, of differing decay-rates outside or inside of the cell, as described in the main text.

To estimate cortical actin (CA)-thickness, we used the pixel-intensity “profiling” capabilities of the LSM imaging software (LSM v5, Zeiss) to measure the actin’s fluorescence intensity, I_a , of suspended cells. In healthy (untreated) cells, cortical actin (CA) was clearly observed and maximum I_a -values, I_{max} , therefore occurred near the cell-membrane (Fig. 2.11 A). I_a -values decreased more rapidly outside the cell than in the cytoplasm, and to fit I_a -data (Fig 2B) we assumed (i) a “fast” exponential decay outside, and (ii) a “slow” exponential decay inside:

$$I_a = I_{max}e^{-k_{out}[a-x]}, \quad x < a \quad (15a)$$

$$I_a = I_{max}e^{-k_{in}[x-a]}, \quad x > a \quad (15b)$$

where k_{out} and k_{in} are the decay-constants outside and inside the cell, respectively, and a is the x -position of I_{max} (measured along the profile-line as shown in Fig. 2.11 A). MFs are well-known to extend from the cortex into the cytosol and to interact with cytosolic- and other CSK- structures [98]; this is corroborated by the slow decays of I_a -values measured in the cytosol. To estimate CA-thickness, d_{exp} , we calculated the distance at which I_a -values decreased to $I_a = (I_{max}/e)$ for both $x < a$ (Eq. 15a) and $x > a$ (Eq. 15b), and then added the two values to obtain d_{exp} . Dividing d_{exp} by the cell-radius, r_c , gives $d\% = d_{exp}/r_c$, where $d\%$ is the fraction of CA-thickness of the cell, expressed in %.

2.2 Results

We will now summarize the results of DEP, EP, and ED experiments, which we have previously reported in two published articles (Appendices II and III). The first article to be summarized (Sects. 2.2.1 and 2.2.2) describes combined DEP and EP for novel cell-manipulations, using U937 monocytes as a model cell-type. The second article to be summarized (Sect. 2.2.3) describes ED-based mechanical characterization of individual CHO and U937 cells.

2.2.1 Dielectrophoresis (DEP)

In order to displace cells within a liquid (aqueous) suspension medium, and to position individual cells accurately and reliably, we examined the DEP-response of cells as a function of the experimental variables f and σ_m (as described in Sect. 2.1.7.1). Both nDEP and pDEP of U937 cells was observed (Fig. 2.12), and the DEP crossover-frequency, f_0 , measured as a function of σ_m (Fig. 2.13), permitted dielectric characterization of this cell-type. These experiments were therefore used to establish the proper choice of experimental conditions for ED, which are discussed later in Sect. 2.3.3.

The measured DEP spectra of U937 cells revealed the ranges of f and σ_m for which both pDEP and nDEP positioning could be achieved (Fig. 2.12 B and C, respectively). The results can be represented by f_0 -data (Fig. 2.13), where a linear relationship between f_0 and σ_m was observed for $0.02 < \sigma_m$ (S/m) < 0.2 . When σ_m was close to the physiological value, 1.5 S/m, only nDEP was observed within the frequency range investigated, the onset of pDEP occurring only when $\sigma_m < 0.4$ S/m.

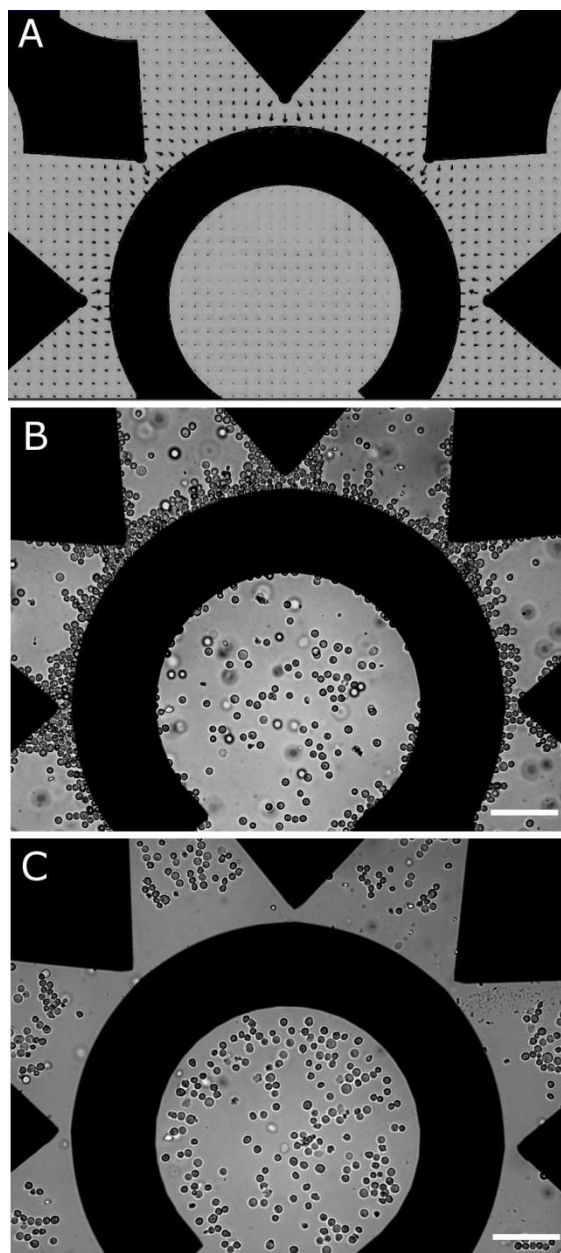


Figure 2.12 Positioning of U-937 monocytes by DEP. (A) The strength and direction of the simulated electric field, E , are indicated by the lengths and directions of arrows; (B) cells were positioned in the strong- E regions by pDEP; (C) cells were positioned in the weak- E regions by nDEP. Scale bars are 300 μm .

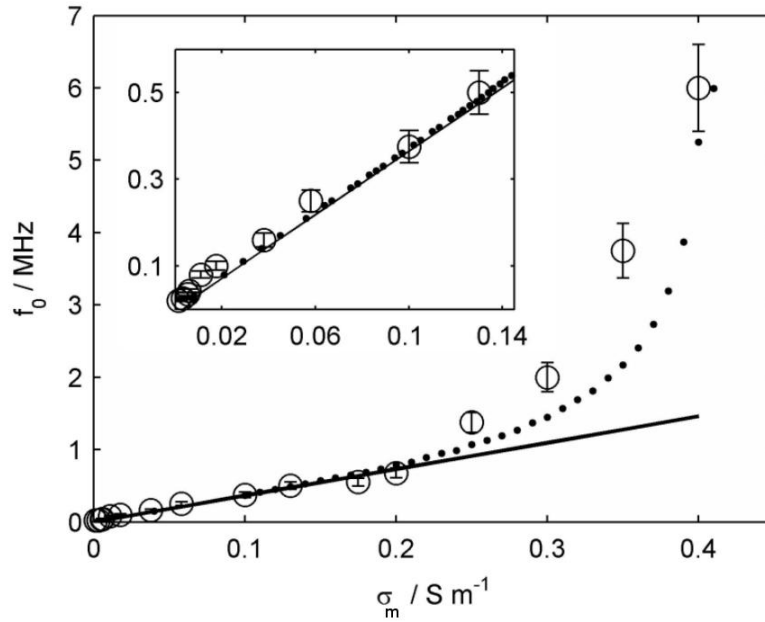


Figure 2.13 The crossover frequency, f_0 , versus conductivity of the suspension medium, σ_m , for U-937 monocytes. Open circles are experimental values of f_0 (mean \pm SD, $n = 3$), while the dotted and solid lines are fits using Eqs. 3 and 4, respectively; the insert shows the region of low σ_m values.

The intercept of f_0 -data extrapolated towards $\sigma_m = 0$ (the origin in Fig. 3.2) was close enough to zero that an upper limit of $\sigma_{CM} < 10^{-5} \text{ S m}^{-1}$ ($G_{CM} < 1430 \text{ S m}^{-2}$) could be determined. In order to estimate ϵ_{CM} and σ_i , we fit f_0 data using both Eq. (3) (with the condition $K(f_0) = 0$) and Eq. (4) (valid for $\sigma_m < \sim 0.2 \text{ S m}^{-1}$, see Fig. 2.13). The best fit for both equations was found when $\epsilon_{CM} = 6.0\epsilon_0$ ($C_{CM} = 7.6 \text{ mF m}^{-2}$) and $\sigma_i = 0.425 \text{ S m}^{-1}$. These data therefore provide estimates for the dielectric properties of U937 monocytes, namely $\sigma_{CM} < 10^{-5} \text{ S m}^{-1}$ ($G_{CM} < 1430 \text{ S m}^{-2}$), $\epsilon_{CM} = 6.0\epsilon_0$ ($C_{CM} = 7.6 \pm 1.25 \text{ mF m}^{-2}$), $\sigma_i = 0.425 \text{ S m}^{-1}$, and $\epsilon_i = 80\epsilon_0$, which were used to calculate ϵ_c^* (Eq. 1) and therefore to predict DEP responses under arbitrary conditions of f and σ_m .

2.2.2 Electroporation (EP)

The application of higher voltage ($7 \text{ V} < U < 10 \text{ V}$), short-duration ($t_e < 100 \text{ }\mu\text{s}$) pulses, superimposed on the 2 MHz a. c. voltage for DEP, demonstrated position-dependent EP of cells within the region of spatially non-uniform electric field. These results were monitored using “Live/Dead” cell-viability tests (described in Sect. 2.1.5). Although the cells displayed some non-uniform “anomalous” behaviour (some cells in the strong-E regions remained green (live), while others in weak-E regions became red (dead)), a clear position-dependent response to EP could be observed (Fig. 2.14) that was consistent with the calculated distribution of E (Fig. 2.15). For the case of low pulse amplitudes ($U < 4 \text{ V}$), few green-to-red transitions occurred (less than 3% of cells), but as U was increased the regions containing red (dead) cells expanded from near the tips of the “e1” electrodes to eventually occupy the entire space between electrodes e1 and e2 when $U > 8 \text{ V}$ (2.15 B, C). Therefore, the “critical” field values for reversible and irreversible EP could be estimated from calculated field values and these observed live/dead cell distributions, namely $E = 40 \text{ kV m}^{-1}$ and $E = 120 \text{ kV m}^{-1}$, respectively. For example, when $U = 10 \text{ V}$, the region of irreversible EP coincided with that in which pDEP was observed in the course of cell-positioning experiments (Fig. 2.12 B), while reversible EP was observed in the nDEP region (Fig. 2.12 C).

Cell positioning by DEP prior to EP significantly influenced transfection efficiency (using the fluorescent GFP plasmid described in Sect. 2.1.7.2) and cell viability, compared with randomly-distributed cells (“no DEP”) under otherwise identical pulsing conditions (Fig. 2.16). A coupling between DEP and EP was evident, where the number of transfected cells increased with U initially for all three cases (nDEP, no DEP, pDEP) (Fig. 2.16 A), but then decreased above $U = 8 \text{ V}$, initially for pDEP and then for “no DEP”. For EP amplitudes of $U = 7$ or 8 V , viability was generally high, while higher EP amplitudes reduced viability (Fig. 2.16 B). Cell viability decreased monotonically as EP amplitude U increased. Transfected cells that survived the first 24 hours after EP remained viable and were observed to proliferate for the duration of our observations (one week). For the control group (no DEP, no pulses) we found $N_T = 0$, as expected; in other words, uptake and expression of DNA plasmids occurred only in cells which had received sufficient (reversible) EP.

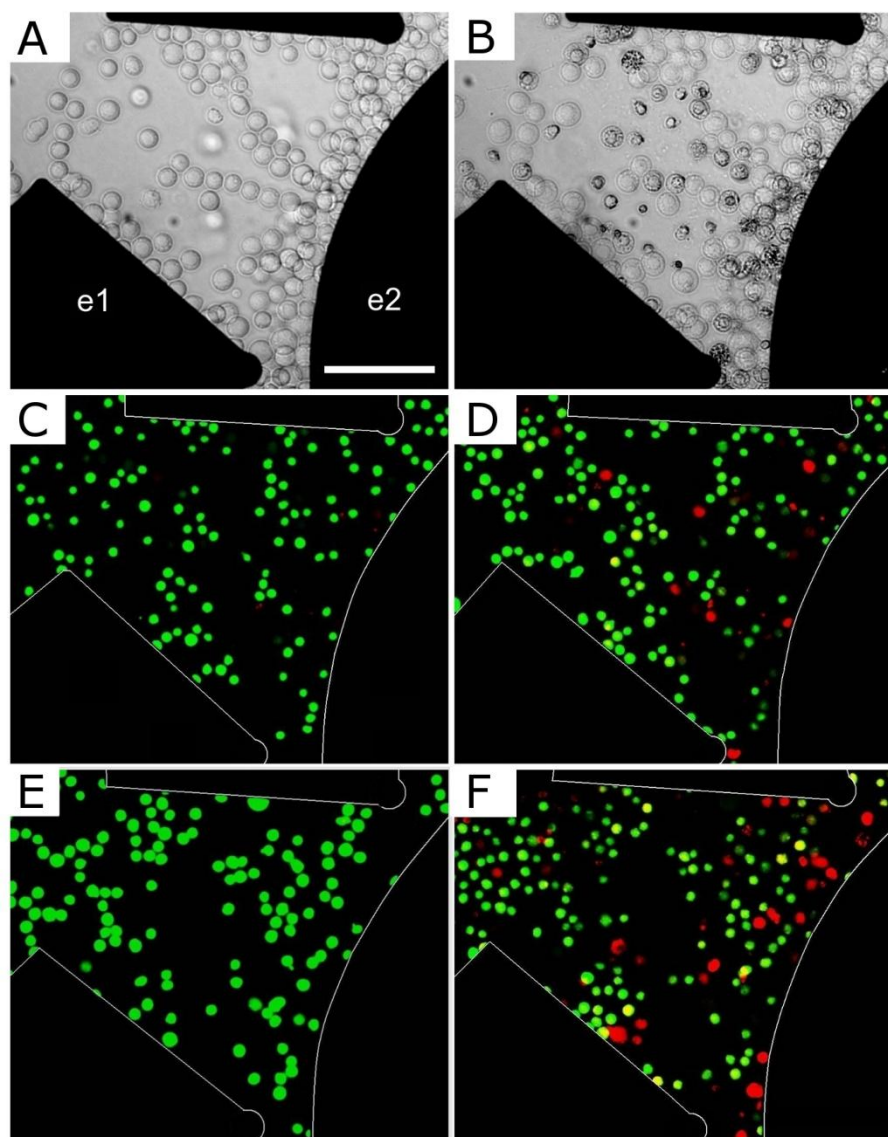


Figure 2.14 Position-dependent EP of U937 monocytes. (A) Live cells, shown before pulsing; (B) The same cells shown in (A), but five minutes after applying pulses of amplitude $U = 8$ V; (C-F) show results of Live/Dead viability tests before (C, E) or after (D, F) pulsing; (D) The same cells shown in (C), but five minutes after applying pulses of amplitude $U = 8$ V, showing limited cell death. (F) The same cells shown in (E), but five minutes after applying pulses of amplitude $U = 10$ V, showing more extensive cell death near the pDEP region; Live cells appear green and dead cells appear red; scale bar = 100 μm .

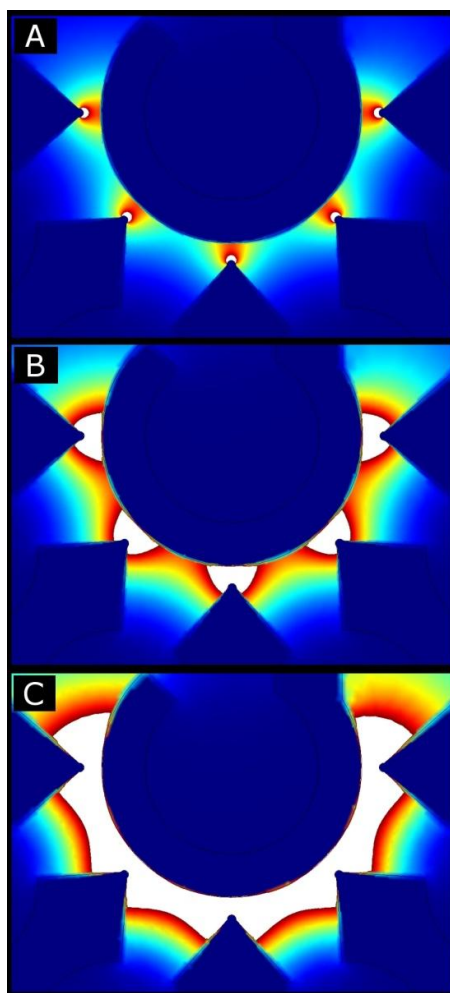


Figure 2.15 Calculated position-dependence of EP of U937 monocytes, for different values of U . White = irreversible EP (cell lysis), Red-Green = reversible EP, Blue = no EP. (A) $U = 6$ V, (B) $U = 8$ V, (C) $U = 10$ V. Position-dependent gene transfection level and viability of U937 monocytes.

The extent to which EP was reversible or irreversible (live or dead cells in Fig. 2.14) corresponded quite well with simulations (white regions in Fig. 2.15): Regions in which EP was irreversible, leading to lysis and cell-death, expanded from the tip regions as a function of rising U values (Fig. 2.15 A-C).

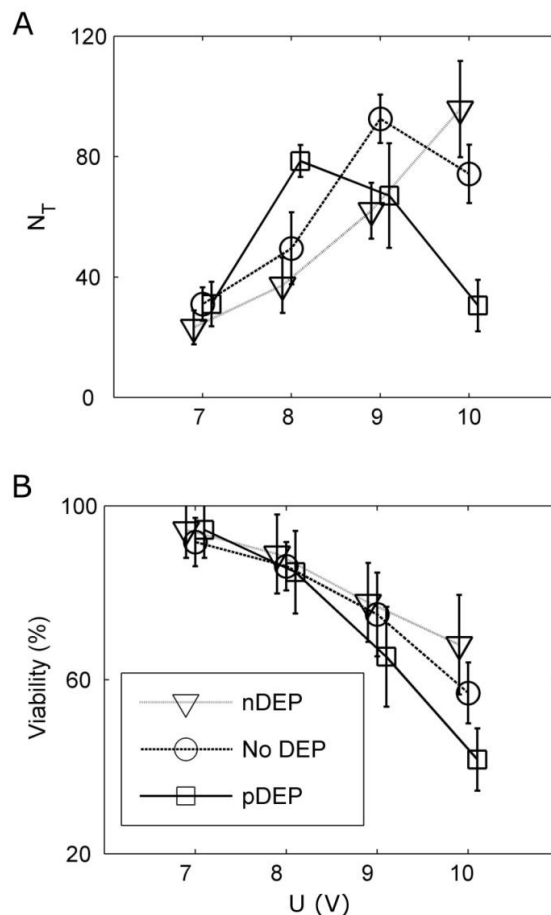


Figure 2.16 Position-dependent transfection of U937 cells. (A) Number of transfected cells, N_T , and (B) viability vs. pulse amplitude, U , for cells positioned by either pDEP (squares), nDEP (triangles), or with “no DEP” (no induced positioning, circles) prior to pulsing. Mean \pm SD ($n=4$) values are shown, and data were shifted slightly in the horizontal direction to facilitate distinction between groups.

Positioning of cells in regions of high-E by pDEP prior to EP resulted in increased gene delivery (transfection) at low U (Fig. 2.16 A, squares, $U = 8V$), but loss of cell-viability reduced the number of viable transfected cells at higher U (Fig. 2.16 A, B, squares, $U > 8V$). Compared to control conditions (Fig. 2.16, No DEP: circles), positioning of cells in regions of low-E by nDEP (Fig. 2.16, triangles) had roughly the inverse effects of pDEP (Fig. 2.16, squares), when compared to control conditions (Fig. 2.16, circles “No DEP”).

2.2.3 Electro-deformation (ED)

Our ED protocol permitted measurement of time-dependent strain, $\gamma(t)$, of individual cells over several cycles of strain and relaxation (Figs. 2.17 and 2.18). CHO were observed to be stiffer than U937 cells, and γ of the latter showed more significant long-term residual strain (or plastic deformation) than the former. Maximum values of γ for CHO cells were limited to ~ 0.2 (Fig. 2.17 C) whereas, for a typical U937 cell, $\gamma > 0.5$ was observed after the third cycle (Fig. 2.18 C). In some cases, contact with neighbouring cells imposed a limit on γ (indicated by “CL” in Fig. 2.18 C).

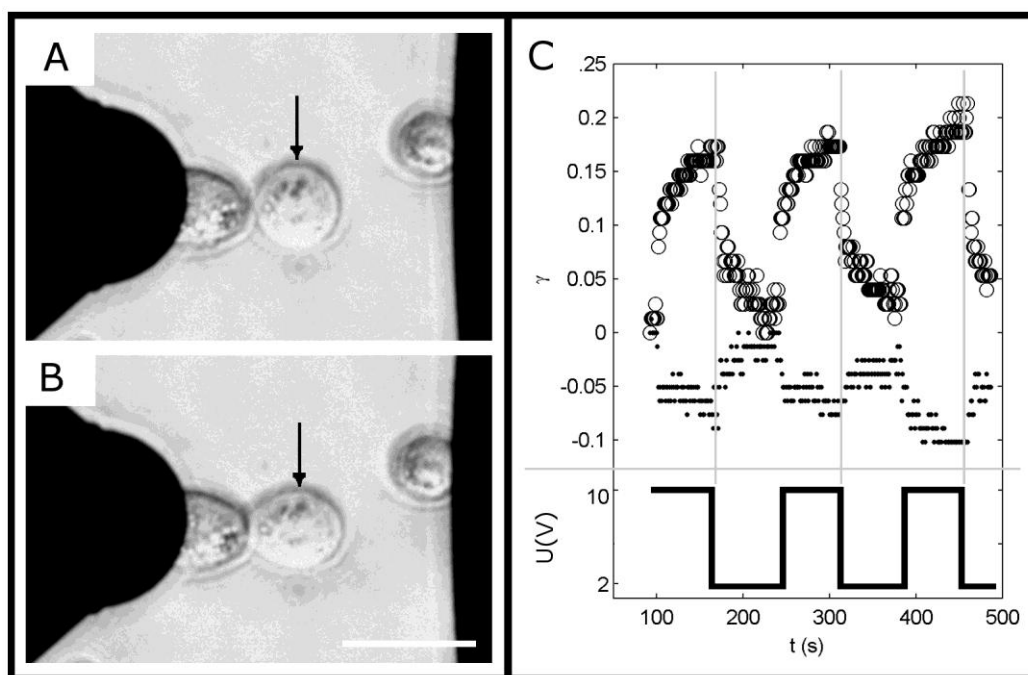


Figure 2.17 CHO stretching and recovery. (A) CHO cells in a DEP “holding potential” of $U = 2\text{V}$. (B) The same cells as in (A) 60 seconds after applying a potential step function, $U = 10\text{V}$. (C) strain, $\gamma(t)$, of the middle cell (see arrow in (A) and (B)) during the first 3 cycles; circles: γ_x , or dots: γ_y refer to the cell’s major or minor axes ; the applied electric potential, $U(t)$, is shown on the same time scale as γ . Scale bar = $25\ \mu\text{m}$.

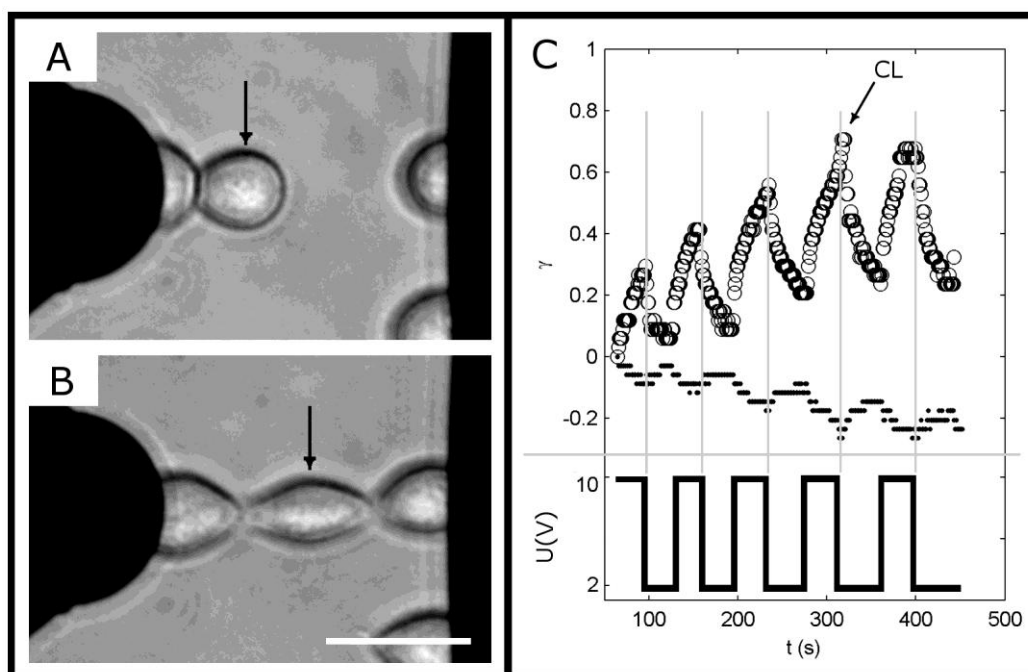


Figure 2.18 U937 stretching and recovery. (A) U937 cells in a DEP “holding potential” of $U = 2\text{V}$. (B) The same cells as in (A) 30 seconds after applying a potential step function, $U = 10\text{V}$. (C) strain, $\gamma(t)$, of the middle cell (see arrow in (A) and (B)); circles: γ_x , or dots: γ_y refer to the cell’s major or minor axes; the applied electric potential, $U(t)$, is shown on the same time scale as γ . Contact between cells (B) limits the maximum value of γ , which is indicated in (C) by “CL”. Scale bar = $25\ \mu\text{m}$.

Although contact between cells could limit the maximum strain in some cases (Fig. 2.18 B), data were always taken from the first cycle of strain and relaxation of freely-deformable cells (Fig. 2.19), where strain was not limited by the presence of other cells. Deformations of CHO and U937 cells were rendered reasonably well by both the SLS and PL models, when the maximum value of strain was limited to $\gamma < \sim 0.2$ (Fig. 2.19). Long-term plastic deformation of U937 cells was observed for higher γ values (Fig. 2.18 C), but the maximum applied stress ($\zeta \sim 20\ \text{Pa}$) was insufficient to induce comparable high strain in the case of CHO cells (Fig. 2.17 B). The three parameters of the SLS model (k_1 , k_2 , and η) can be related to the following material properties [103]: $k_1 = E_R = 2(1 + \nu)G_R$, and $(k_1 + k_2) = E_0 = 2(1 + \nu)G_0$, where E_R is the relaxed elastic modulus, G_R is the relaxed shear modulus, E_0 is the initial elastic modulus, and G_0 is the initial shear modulus.

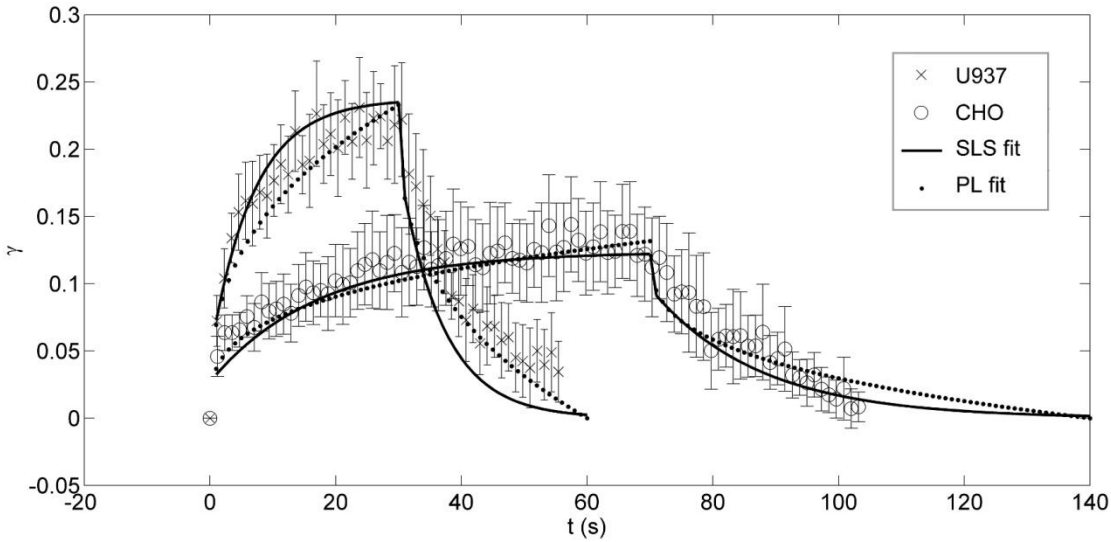


Figure 2.19 Strain and relaxation data for U937 and CHO cells, fit using the “standard linear solid” (SLS) or power-law (PL) models. Fitting parameters are shown in tables 1 and 2, respectively. Data are mean \pm SE; N=10 for U937 cells and N=5 for CHO cells.

Table 2.1 Mechanical properties of cells derived using the SLS model

Cell type	ν^*	E_R (Pa)	G_R (Pa)	E_0 (Pa)	G_0 (Pa)
CHO	0.37 ± 0.07	193 ± 130	70.3 ± 60.7	1572 ± 1059	574 ± 495
U937	0.39 ± 0.14	99.4 ± 44.0	35.8 ± 28.7	898 ± 397	323 ± 259

* Apparent Poisson's ratio of the cell; all values are mean \pm SD (CHO: N = 5, U937: N = 10)

Table 2.2 Model parameters for the “power-law solid” (PL)

Cell type	α	A ($\times 10^{-3} \text{ Pa} \cdot \text{s}^{-\alpha}$)	$G'(1 \text{ Hz})$ (Pa)*
CHO	0.301 ± 0.20	3.7 ± 2.49	466 ± 314
U937	0.356 ± 0.11	7.0 ± 3.10	262 ± 116

* Low-frequency storage modulus, $G'(\omega)$, given by Eq. (11).
† All values are mean \pm SD (CHO: N = 5, U937: N = 10).

CHAPTER 3. SUPPLEMENTARY RESULTS

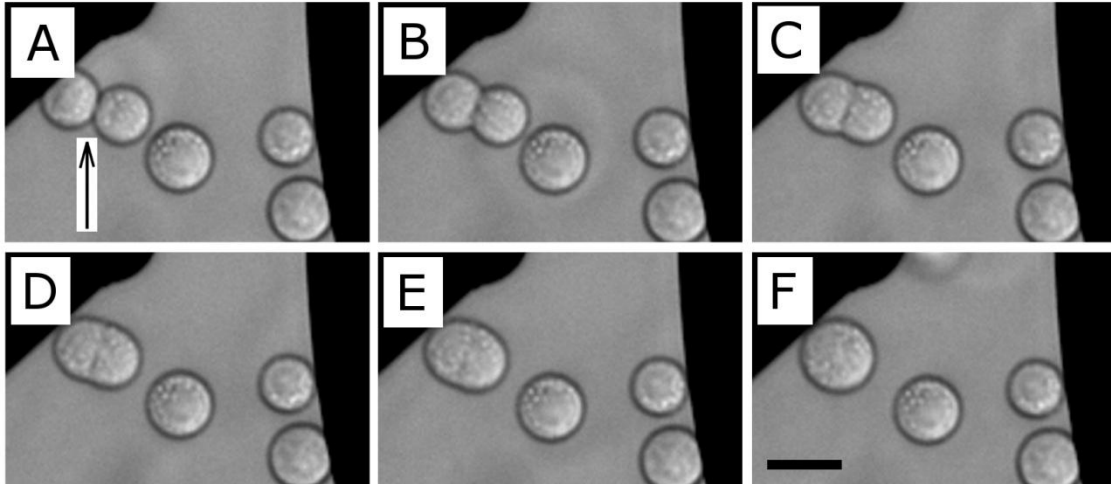
This chapter includes results that have not been previously reported. These unpublished results include DEP of cells in gels, combined DEP/EP for electro-fusion of cells, and more ED experiments using additional cell-types (L929 and HEK293). Confocal fluorescence imaging of the CSK was used for structural analysis of cells, and cortical actin thickness was correlated with measured mechanical properties. Finally, modification of the cells with CSK-disruptive drugs was found to have measurable effects on cell-mechanics.

3.1 Dielectrophoresis in gels

We performed several “trial” experiments in which U937 monocytes were patterned by DEP in gels (gelatine or agarose). As the gels cooled and solidified over the electrodes during DEP, cell-motion was observed to slow gradually until they were “frozen” in the solid gel. Although our reported DEP experiments were mostly performed using aqueous suspension media, we briefly mention these “gel” results as evidence for potentially broader applicability of DEP for tissue engineering applications.

3.2 Electro-fusion

Electro-fusion (EF) is a well-known technique in which multiple cells are first brought into contact with one-another by DEP; EP and the subsequent intermingling of multiple CMs then results in fusion of multiple cells (Fig. 3.1). A vast number of “hybrid” cell-types have been created by EF [76, 104], and it has also been used extensively for cloning applications [104]. Although microfabricated EF platforms have great potential for improving EF results, they remain rare in the literature [105].



Figur4 3.1 Electro-fusion of U937 monocytes. Two cells indicated by an arrow in (A) are fused together (B-F) after combined dielectrophoresis and electro-poration; time between images is ~ 5 s; scale bar = $20 \mu\text{m}$.

3.3 Electrodeformation

3.3.1 Electrodeformation of several mammalian cell-types

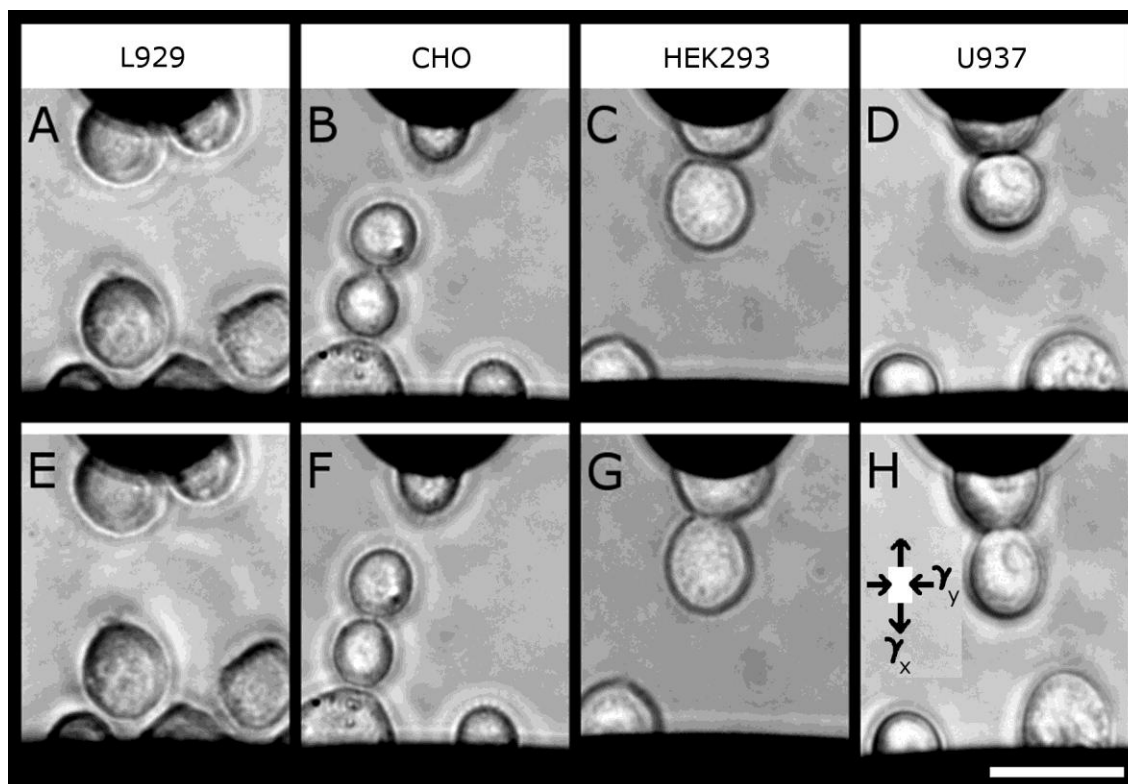


Figure 3.2 Trapping and deformation of cells. Four differing cell-types (L929, CHO, HEK293, U937) were trapped by dielectrophoresis (A-D) and deformed by electro-deformation (E-H): In all cases, cells near to either of the two opposing electrodes were trapped at the electrode-edges using an applied sinusoidal electric potential of amplitude $U = 2 \text{ V}$ and frequency $f = 5 \text{ MHz}$. The electrodes are shown in black; cells were then deformed by increasing U (E-H, $U = 10 \text{ V}$), and deformation was found to depend on the cell-type. Strain-components in the x- and y- directions, γ_x and γ_y , respectively, are shown in H; scale bar = $20 \mu\text{m}$.

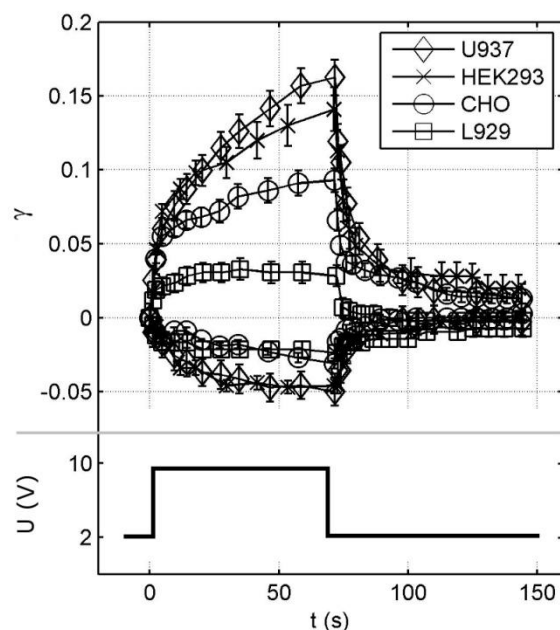


Figure 3.3 Time-dependent strain-data, $\gamma(t)$, of four cell-types. U937 (diamonds, $N = 10$); HEK293 ('x's, $N = 5$); CHO (circles, $N = 5$); and L929 (squares, $N = 5$); data are average values \pm SD/2; both x- and y- strain-components are shown: ($\gamma_x > 0$) and ($\gamma_y < 0$), respectively; the corresponding applied electric potential, U , is shown on the same time-axis.

Table 3.1 Viscoelastic (SLS) parameters of several cell-types

Cell type	ν	E_R (Pa)	E_0 (Pa)	η (Pa·s)	τ_s (s)
L929	0.5 ± 0.05	500 ± 100	5500 ± 850	3000 ± 500	6.6 ± 1.5
CHO	0.4 ± 0.05	160 ± 30	1660 ± 300	2500 ± 450	17.2 ± 3.5
HEK293	0.35 ± 0.05	100 ± 20	900 ± 150	2400 ± 425	25.9 ± 6.0
U937	0.35 ± 0.05	90 ± 20	900 ± 150	2200 ± 400	27.2 ± 6.0

*Note: Values of all SLS parameters were obtained by fitting the rising portion of γ -data, which differs increasingly when compared with the decreasing portion (relaxation) of γ , from top to bottom.

Cell-type dependent deformability of cells was clearly observed visually during ED (Fig. 3.2), and it was confirmed by measured γ -values (Fig. 3.3). L929 were stiffest, followed by CHO, HEK293, and U937. Under identical ED conditions, the maximum γ -values, γ_{\max} , obtained for L929, CHO, HEK293, and U937 cells were roughly equal to 0.03, 0.09, 0.14, and 0.16, respectively (Table 3.1). L929 cells exhibited typically “solid-like” behaviour: After an initially

rapid extension, γ -values were approximately constant after ~ 20 s of applied ζ (Fig. 3.3, squares: $d\gamma/dt \sim 0$ for $t > 20$ s). The other cells also initially extended rapidly, but they continued to deform under constant ζ . For all cell-types, $\gamma_{\max} < 0.2$, and approximately full recovery of the spherical geometry was observed (Fig. 3.3, $\gamma \sim 0$ for $t > 100$ s). The apparent Poisson's ratio, $\nu = -\gamma_x/\gamma_y$, also depended on cell-type, and only L929 cells were observed to be incompressible (Table 3.1, $\nu = 0.5$).

The apparent Poisson's ratio values for CHO, HEK293, and U937 cells were less than 0.5 (Table 3.1), suggesting that these cells are slightly compressible. As mentioned above (Sect. 2.2), both SLS and PL models were found to fit our data reasonably well, but this agreement should not be expected to hold generally; predictions based on these models tend to diverge for the case of small γ values, and at shorter timescales than ~ 1 s used in present work [96]. SLS models showed strong asymmetry when fitting either the rising or falling γ -data of HEK293 and U937 cells: This obviously results in widely differing estimated mechanical properties (compare Tables 2.1 and 3.1), and this remains an important question to resolve.

3.3.2 Cortical actin thickness

All four cell-types tested here were roughly spherical in suspension, and fluorescence microscopy revealed distinct CA in all cases (Fig. 3.4). The simple exponential decay of actin (described in Sect. 2.1.8) was applicable in all cases, and the $d_{\%}$ -values obtained clearly depended on cell-type (Fig. 3.5, Table 3.2). L929 had the highest $d_{\%}$ -value ($\sim 34\%$), followed by CHO ($\sim 21\%$), U937 ($\sim 14\%$), and HEK293 ($\sim 13\%$). These $d_{\%}$ -values were found to be inversely proportional to the corresponding γ_{\max} -values obtained by ED (Fig. 3.5).

Cortical actin filaments are known to extend toward the cytoplasm (mostly radially) from the membrane surface, connecting the cortex three-dimensionally to the cytoskeleton [6, 98]. The actin distributions, which we observed by confocal microscopy decayed exponentially as a function of distance from the maximum intensity values. As already discussed in Sect. 2.1.8, this gave us a reliable method of estimating an effective CA-thickness, $d_{\%}$, but we could not account for other mechanically relevant MF-properties, such as length, orientation, and crosslinking-density of actin filaments. However, the clear correlation between $d_{\%}$ and γ_{\max} (Fig. 3.5)

observed in the present work for the case of L929, CHO, HEK293, and U937 cells confirms the hypothesis that CA-thickness is a major determinant of cell-stiffness [4, 106].

In addition to the CA, we also observed thin shells of cortical vimentin (top-right images in Figs. 3.6 A, and 3.7 A); this disqualifies us from declaring CA to be the only important mechanical structure in the cortex. Treatments of cells with acrylamide (ACR) induced the formation of vimentin aggregates (Fig. 3.7 C), similar to what can be seen in PtK2 cells [100], and in melanophores following treatment with either ACR or nocodazole [107]. However, no significant changes in measured mechanical properties were found to occur without some concomitant disruption of MF networks (top-left images in Fig. 3.7 C). The organization of actin within cells is clearly complex and many properties of CA are known to differ from cytosolic actin. A few examples of MF-properties, which vary according to their locations (and roles) within the cell, include: (i) topological organization [6, 98], (ii) local activity constants of various MF-associated molecules, and (iii) interaction with other structures within the cell, such as IFs [108], MTs [109], and the CM [110-112].

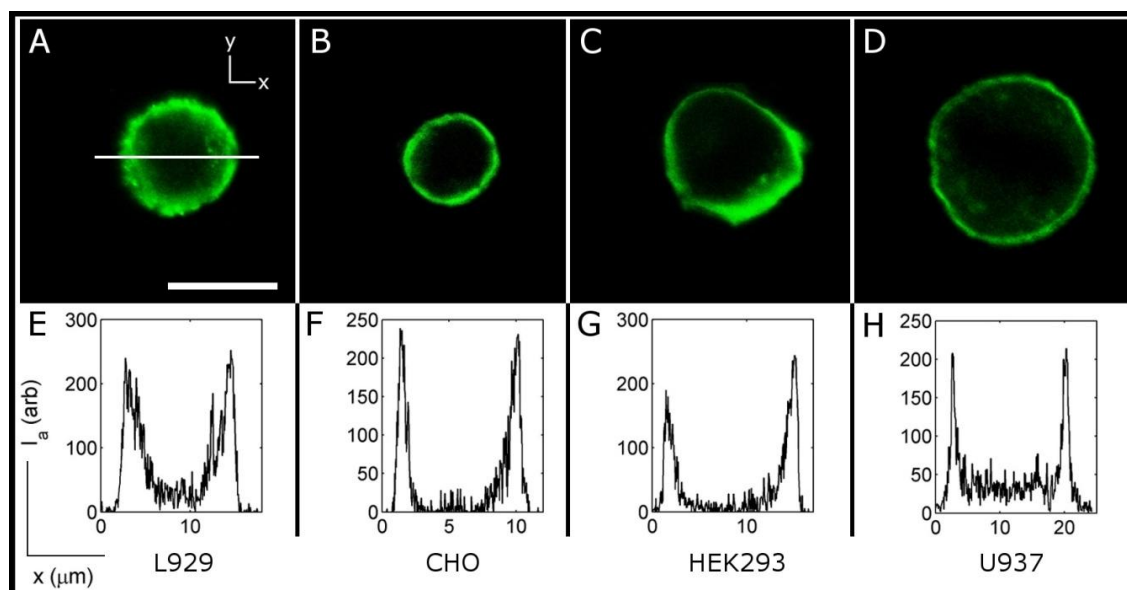


Figure 3.4 Cortical actin in four differing cell-types. Confocal fluorescence images of cortical actin (A-D) and corresponding intensity profiles, I_a (E-H), in four cell-types: L929 (A, E), CHO (B, F), HEK293 (C, G), and U937 (D, H); I_a was measured along a straight line through the center of each cell (as indicated in A); scale bar = 10 μm , same for B, C, D.

Table 3.2 Cortical thickness and maximal strain-values

Cell type	r_c (μm)	d_{exp} (μm)	$d\%$	γ_{max}
L929	6.2 ± 0.4	2.1 ± 0.3	33 ± 5	0.03 ± 0.012
CHO	4.2 ± 1.2	0.9 ± 0.3	21 ± 7	0.09 ± 0.015
HEK293	6.8 ± 0.7	1.0 ± 0.4	15 ± 5	0.14 ± 0.03
U937	6.5 ± 1.0	1.0 ± 0.2	16 ± 4	0.16 ± 0.03
All values are averages \pm SD (N = 10)				

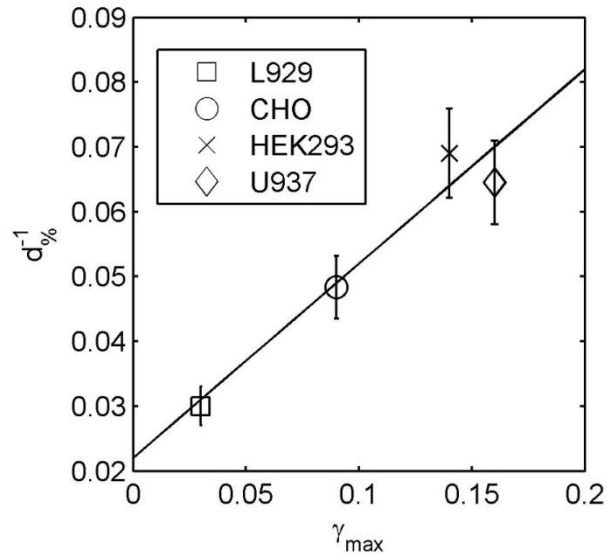


Figure 3.5 Linear correlation between maximum strain and reciprocal cortical actin thickness. Plot of the inverse of $d_{\%}$ - vs. γ_{\max} - values; data are average values \pm SD (N = 10), and refer to experiments wherein the maximal ED-stresses were $\zeta = 20$ Pa.

3.3.3 Modification of the U937-cytoskeleton (CSK)

The effects of either Lat-A or ACR on the CSK of U937 cells, as observed by confocal fluorescence microscopy (Figs. 3.6 and 3.7), differed significantly when short treatment times were used (Figs. 3.6 B, and 3.7 B). Untreated (control) cells had contiguous cortical actin of nearly uniform thickness, as expected (Figs. 3.6 A, and 3.7 A), but we observed a loss of continuity of the CA following treatment with 10 μ M Lat-A, for 2 h (Fig. 3.6 B). In contrast, the CA appeared unchanged following 10 mM ACR for 6 h (Fig. 3.7 B). Longer (4 h) treatment times resulted in concurrent MF- and IF- disruption using Lat-A (Fig. 3.6 C) or ACR (Fig. 3.7 C).

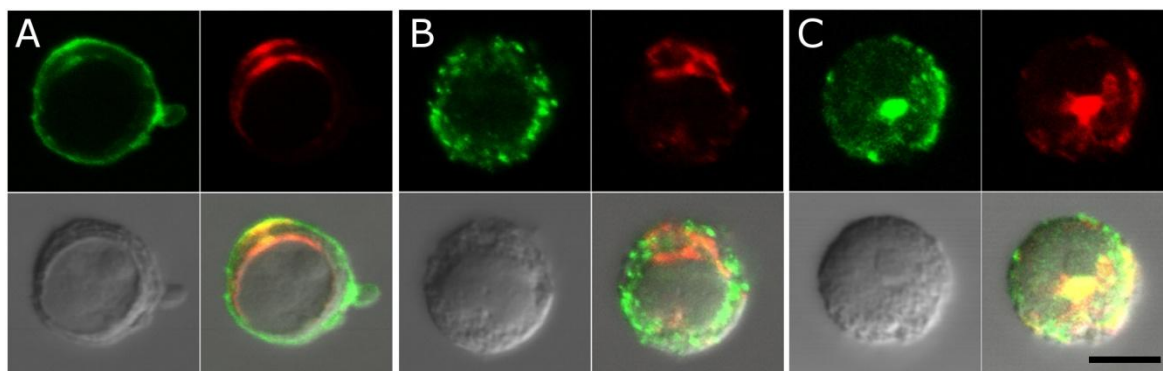


Figure 3.6 Time-dependent effects of 10 μM latrunculin-A treatment in U937 cells. Actin (green) and vimentin (red) were stained with alexa-488-phalloidin and antimouse-Cy3, respectively, as seen in the top quadrants of each images. Lower quadrants show a differential interference contrast image of the observed cell (left) and a composite image of the merged channel (right), with yellow pixels representing colocalisation between actin and vimentin; (A) untreated (control) cells; (B) cells after treatment with 10 μM Lat-A for 2 hours; (C) cells after treatment with 10 μM Lat-A for 4 hours; the scale bar is 10 μm .

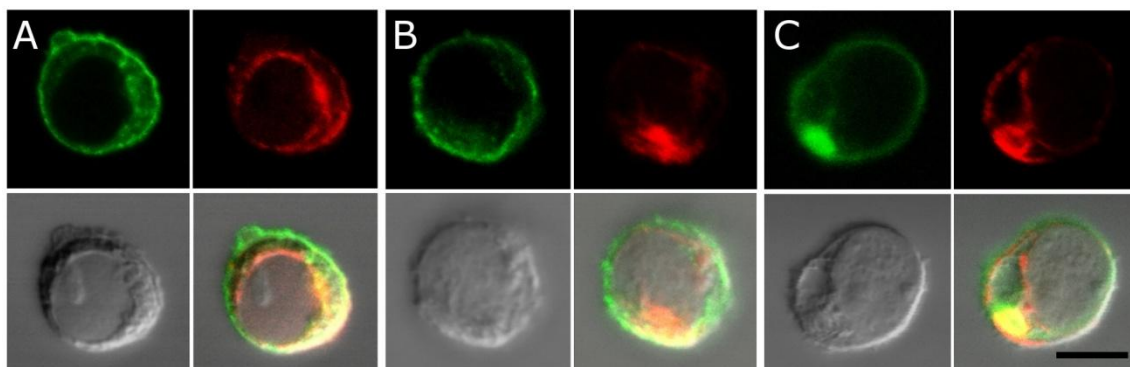


Figure 3.7 Time-dependent effects of 10 mM acrylamide treatment, in U937 cells. Actin (green) and vimentin (red) were stained with alexa-488-phalloidin and antimouse-Cy3, respectively, as seen in the top quadrants of each images. Lower quadrants show a differential interference contrast image of the observed cell (left) and a composite image of the merged channel (right), with yellow pixels representing colocalisation between actin and vimentin; (A) untreated (control) cells; (B) cells after treatment with 10 mM ACR for 6 hours; (C) cells after treatment with 10 mM ACR for 15 hours; the scale bar is 10 μm .

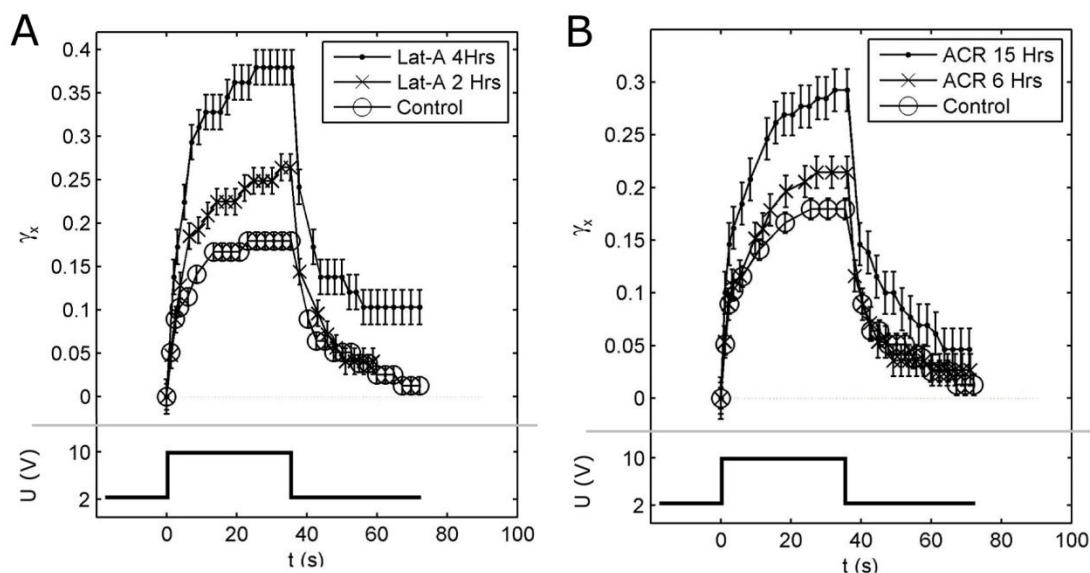


Figure 3.8 Strain data for U937 cells following treatment with 10 μ M latrunculin-A (Lat-A) or 10 mM acrylamide (ACR). A: Lat-A treatments, 4 Hrs (dots, $N = 5$), 2 Hrs ('x's, $N = 5$), or no treatment (circles, $N = 5$); B: ACR treatments, 15 Hrs (dots, $N = 5$), 6 Hrs ('x's, $N = 5$), or no treatment (circles, $N = 5$); data are average values $\pm SD/2$; the corresponding applied electric potential, U , is shown on the same time-axis.

U937 cells with disrupted CSKs were, not surprisingly, less stiff than untreated control cells (Fig. 3.8). The effects of Lat-A were readily observed using 10 μ M concentrations (Fig. 3.8 A), but the effects of ACR were less obvious, even when 10 mM concentrations were used (Fig. 3.8 B). Both Lat-A and ACR significantly reduced cell-stiffness after long treatment times ("dots" in Fig. 3.8). In these later cases, full recovery of the cell's shape was not observed ($\gamma_x > 0$, for $t > 60$ s).

3.4 Electromanipulation of sub-cellular structures

Treatment of cells with CSK-disrupting toxins was also found to have several unintended consequences, namely: (i) loosening of the IF network by ACR treatment freed the cell-nucleus within the cytosol, as manifested by DEP of the nucleus (Fig. 3.9); (ii) weakening of the CA by Lat-A treatment permitted extrusion of blebs (portions of the CM with reduced CA thickness [106]) and cell-contents near the cell-poles under the effects of applied E field (Fig. 3.10); and (iii) release of intercellular contents occasionally resulted in the creation of intact membrane-bound, spherical vesicles (cell-ghosts), which could also be manipulated by an applied E field (Fig. 3.11).

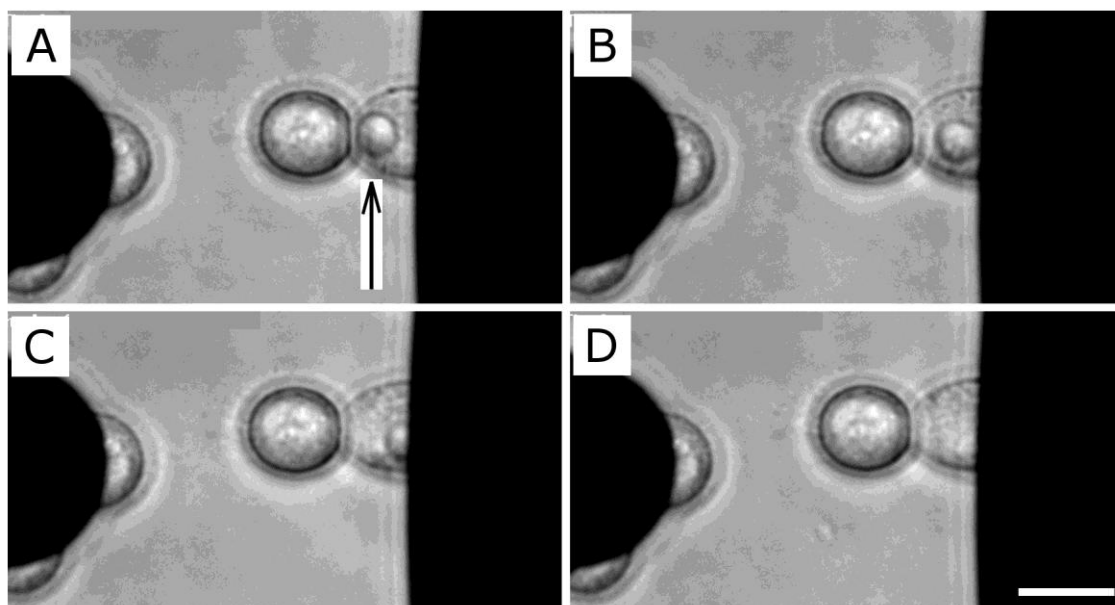


Figure 3.9 Electro-manipulation of a cell-nucleus. U937 cells are shown, following acrylamide-induced disruption of the IF network; (A) The cell-nucleus (indicated by an arrow) is moved within the cell (B-D) upon application of E ($U = 10$ V, $f = 20$ MHz); scale bar = 20 μm .

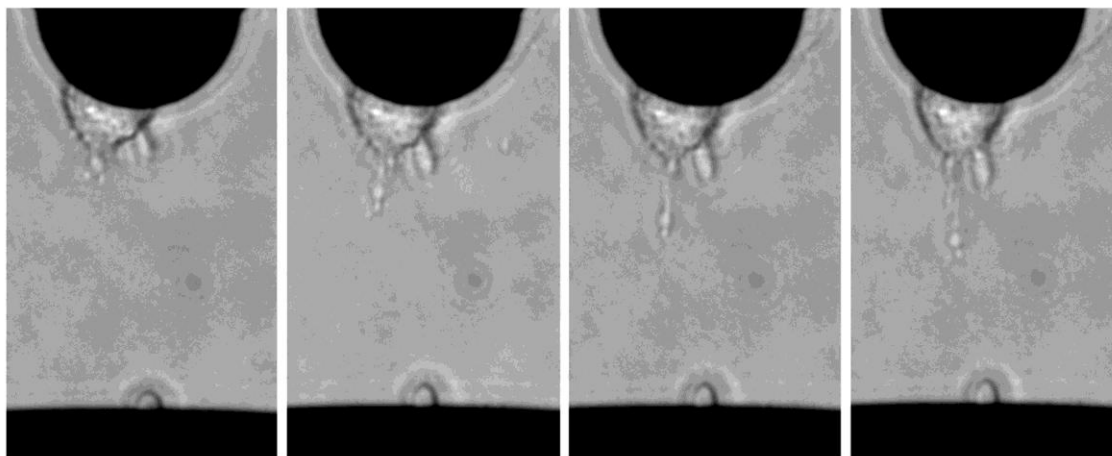


Figure 3.10 Electro-manipulation of blebs and nanoparticles. Following latrunculin treatments, cell blebs and nanoparticles were extruded from some cells; as shown here, for the case of U937 cells, these particles can align at the cell-poles or at electrode edges.

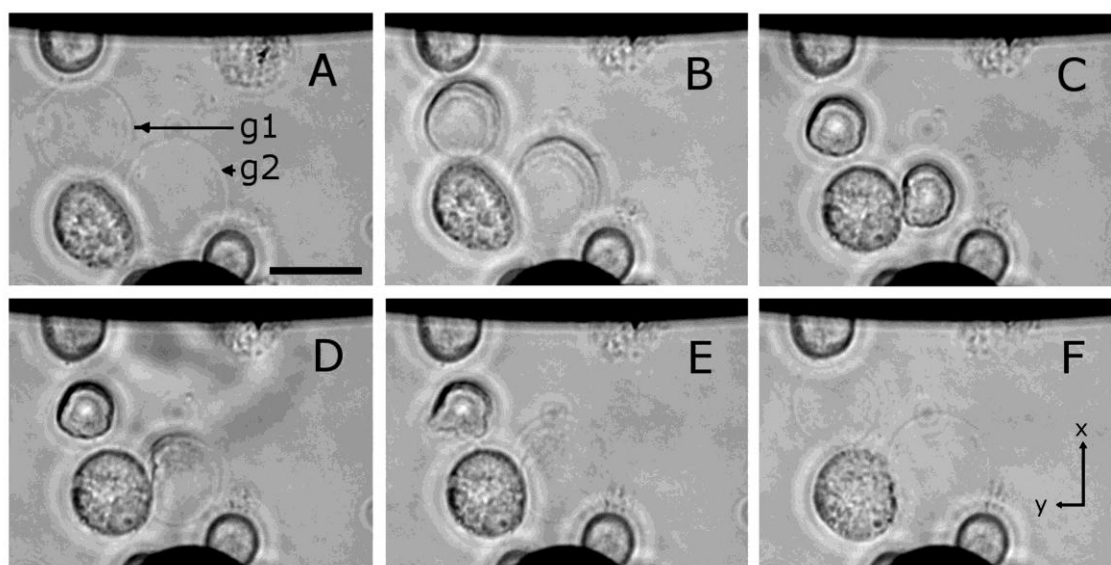


Figure 3.11 Electro-manipulation of cell-ghosts. The release of intracellular contents occasionally resulted in the creation of intact membrane-bound, spherical vesicles (cell ghosts); (A) Cell-ghosts, g1 and g2, are indicated by arrows; (B, C) collapse of g1 and g2, achieved by electric pulses; (D-F) inflation of g1 and g2, achieved by sinusoidal applied E field; scale bar = 20 μm .

CHAPTER 4. GENERAL DISCUSSION

The results presented in this thesis clearly demonstrate that ED can be used for the mechanical characterization of individual mammalian cells, using a microtechnology platform. Aided by microfabrication methods described here, we have produced ED test-devices on glass or transparent plastic (polymer) substrates (Fig. 4.1); we therefore anticipate that diverse future implementations of the methods described in this thesis will take place. We have performed a wide variety of cell- and sub-cellular manipulations: DEP and EP of cell populations, as well as ED of individual cells were all accomplished using the same device incorporating planar microelectrodes. Although similar techniques had previously been reported by others, we have here presented novel applications for each technique. As mentioned in Sect. 1.2 of this thesis, the miniaturization of existing laboratory techniques increases their efficiency and permits scale-up and automation of experiments in ever-decreasing on-chip footprints. The use of DEP in microdevices is well-established, but EP and especially ED are not as widely used. The use of combined DEP and EP for EF is a particularly good example of a widely-performed technique, which would benefit greatly from miniaturization due to the increased ability to handle and observe individual cells and fusion products. Mechanical measurements by ED are not widely-reported in either standard- or miniaturized- platforms; however, we believe that ED provides several advantages over other techniques such as OT, which we will discuss below.

The cell-type selectivity of DEP has been used by others to enrich solutions and to target specific cell-types within mixtures (as discussed in Sect. 1.3.1). Combined DEP and EP methods therefore have the potential for cell-type specific lysis, labelling, fusion, or gene transfer. Although we demonstrated position-dependent EP of a single cell-type (U937) and we influenced EP-results by prior DEP-positioning, in future work the use of multiple cell-types is needed to demonstrate true selectivity of DEP/EP manipulations. The inherent heterogeneity of dielectric and properties within cell-populations presents both challenges and opportunities to DEP/EP experiments: Detailed sub-cellular structures, cell-cycle, and other factors affect the DEP and EP characteristics of cells. To study the detailed structure of cells on an individual basis, supporting technologies such as microfluidic channels are required to provide circulation and recuperation of the cells.

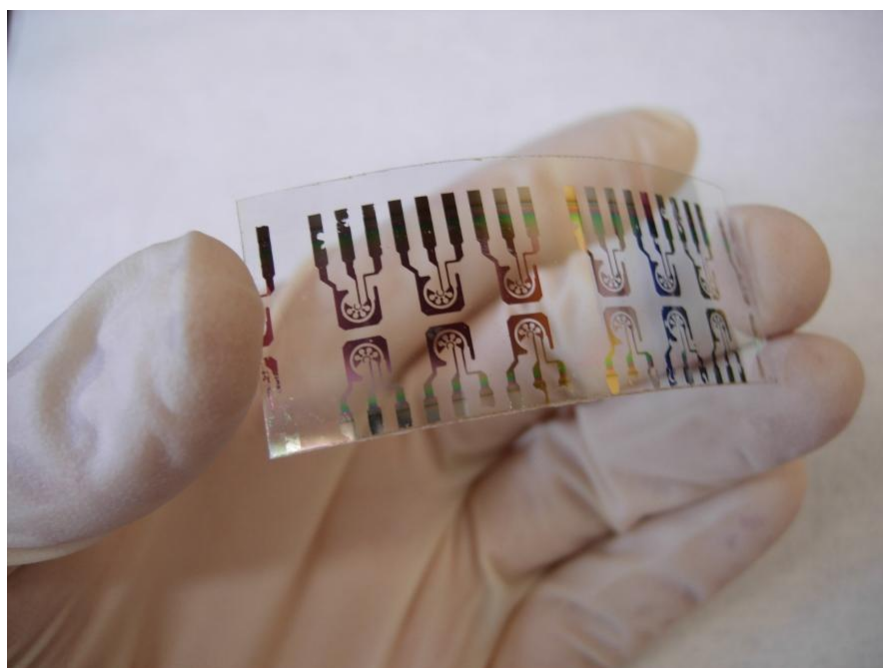


Figure 4.1 Planar electrode array micro-fabricated on a transparent insulating (flexible) polymer substrate.

Table 4.1 Physical and viscoelastic (SLS) properties of several cell-types

Cell type	r_c (μm)	E_R (Pa)	E_0 (Pa)	η (kPa·s)	τ_s (s)	Method	Ref.
L929	6.2 ± 0.4	500 ± 100	5500 ± 850	3.0 ± 0.5	6.6 ± 1.5	ED	*
CHO	4.2 ± 1.2	160 ± 30	1660 ± 300	2.5 ± 0.5	17.2 ± 3.5	ED	*
HEK293	6.8 ± 0.7	100 ± 20	900 ± 150	2.4 ± 0.4	25.9 ± 6.0	ED	*
U937	6.5 ± 1.0	90 ± 20	900 ± 150	2.2 ± 0.4	27.2 ± 6.0	ED	*
Neutrophil [§]	~ 4.0	30 ± 12	100 ± 35	0.013 ± 0.005	0.65 ± 0.3	MPA	27
Chondrocyte [¶]	7.4 ± 0.9	$\sim 80 \pm 40$	$\sim 200 \pm 200$	$\sim 3 \pm 2$	$\sim 70 \pm 40$	MPA	5
Chondrocyte [‡]	6.3 ± 0.9	$\sim 200 \pm 50$	$\sim 400 \pm 150$	$\sim 8 \pm 10$	$\sim 75 \pm 70$	MPA	5

*Present work: Values of all SLS parameters were obtained by fitting the rising portion of γ -data, which differs increasingly when compared with the decreasing portion (relaxation) of γ , from top to bottom.

[§]Neutrophils were from human donors.

[¶]Chondrocytes from articular cartilage of mature pigs; MPA done using media with osmolality: 153 mOsm

[‡]Chondrocytes from articular cartilage of mature pigs; MPA done using media with osmolality: 303 mOsm

The ED experiments presented here are the first to systematically compare multiple mammalian cell-types, other than erythrocytes (RBC). Of the four cell-types tested here, L929 fibroblasts were the stiffest, followed by CHO, HEK293, and U937, respectively. Differences in their measured mechanical properties were attributed mostly to their differing CSKs (Fig. 3.4), and we observed an inverse relationship between $d_{\%}$ and γ_{\max} (Fig. 3.5): L929, the stiffest, had the thickest CA, followed by CHO, HEK293, and U937. The linear fit in Fig. 3.5 suggests that cells possessing $d_{\%}$ -values in excess of $d_{\%} \sim 50$, cannot be measured ($\gamma_{\max} = 0$) using $\zeta_{\max} = 20$ Pa. Higher ζ -values are therefore required to increase the applicability of ED: ζ depends on the square of $E = U/d_e$ (Eq. 8) and increased ζ can therefore be achieved by increasing U (here, $U_{\max} = 10$ V) or by decreasing the inter-electrode distance (we used $d_e = 50$ μm). In the present configuration, ED can be used to deform objects having $E_0 < 5$ kPa, provided that $K \sim 1$ in Eq. 8.

Using the SLS model, our estimated E_0 values (Table 4.1) fit within the large range of previously reported values (Fig. 1.3: $100 \text{ Pa} < E_0 < 10,000 \text{ Pa}$) [3]. The mechanical properties of L929 have previously been measured by others; on the timescales of bleb formation (~ 10 s), the response of the actin cortex was purely elastic [106]. HEK293 and U937 cells, however, were significantly more readily deformed than either L929 or CHO. Although HEK293 were derived from an embryonic human kidney source [113], they have recently been related to neural progenitor cells [114], and their true lineage is not known. U937 are human promonocytes (white blood cells) derived from histiocytic lymphoma [115], and they are cultured in suspension. The larger deformability of U937 cells compared with the other cell-types discussed here can be explained by the fact that high deformability is often associated with cells of the circulatory system [103]. Cell-types such as L929, CHO, and HEK293, are normally adherent and their measured mechanical properties in suspension therefore raise several questions: Can these measured properties be related to adherent geometries? Can ED be applied to adherent cells?

We used suspended cells for two principle reasons: (i) They are easy to manipulate by DEP, and (ii) to achieve roughly-uniaxial ED and therefore provide a stable geometry, which showed similarity between the tested cell-types. New electrode geometries can surely be conceived for ED of adherent cells, although modelling their mechanical response may require more sophisticated geometrical representations than used here. Finite-element modelling (FEM) [117] may be used in the future to simulate complex geometries and to include the differing mechanical roles of sub-cellular components.

CONCLUSIONS AND OUTLOOK

Electrical stresses generated by planar microelectrodes with relatively low values of applied potential ($U < 10$ V) have been used to electro-deform several types of mammalian cells (L929, CHO, HEK293, and U937) in suspension. The electrode geometry and ED methodology have permitted detailed and reproducible biomechanical characterizations of individual cells of these cell-types. Our ED devices were microfabricated on microscope slides to permit in-situ real-time observation by optical microscopy during ED; sophisticated imaging methods can therefore be used to also study the mechanics of sub-cellular structures such as the cytoskeleton. It may further be possible to include imaging arrays directly in an ED device for increased portability. So-called “cell-on-chip” micro-fluidic devices, which permit multimodal analysis and manipulation of cells [57, 116], can be readily made to incorporate micro-electrodes for ED-based mechanical measurements. Electric fields are already used for diverse and often complementary manipulations of cells and sub-cellular particles. Taken together, the DEP, EP, and ED results presented in this thesis strongly suggest that electric fields could play prominent roles in future cell-based microtechnology platforms. However, supporting technologies such as microfluidics are required in future devices, to take full advantage of single-cell manipulations.

Reliable use of the ED technique requires experimental calibration of the generated forces and stresses. For example, cell-sized synthetic microspheres with well-characterized mechanical properties might be used as reference materials; this type of measurement would increase the precision for estimating ζ , which was calculated analytically in the present work (Eq. 8). Nevertheless, values of mechanical properties deduced here compare well with those reported in the literature (Table 4.1). Still, more realistic modelling of cell mechanics is required: Although the SLS and PL models were useful for rapid characterization (parameterization) of the investigated cell-types, the interpretation of mechanical data would benefit from more realistic cell- and electrode- geometries simulated within dynamic environments.

Finally, the use of ED for mechanical characterization of adherent cells or biomaterials other than cells (for example, small tissue constructs) is possible in theory, but is limited to materials with $E_0 < 5$ kPa in the present configuration: New electrode geometries and increased U ($U > 10$ V) are expected to widen the applicability of ED in the future.

BIBLIOGRAPHY

1. Alberts, B., Johnson, A., Lewis, J., Raff, K., Walter, P., *Molecular Biology of the Cell*. 4 ed. 2002, New York: Garland Science.
2. Lodish, H., Berk, A., Matsudaira, P., Kaiser, C. A., Krieger, M., Scott, M. P., Zipursky, L., Darnell, J., *Molecular Cell Biology*. 5 ed. 2003, New York: Freeman and Company.
3. Suresh, S., *Biomechanics and biophysics of cancer cells* Acta Biomaterialia 2007. **3**: p. 413-438.
4. Ananthakrishnan, R., Guck, J., Wottawah, F., Schinkinger, S., Lincoln, B., Romeyke, M., Moon, T., Käs, J., *Quantifying the contribution of actin networks to the elastic strength of fibroblasts* J. Theor. Biol. , 2006. **242**: p. 502-516.
5. Guilak, F., Erickson, G. R., Ping Ting-Beall, H., *The effects of osmotic stress on the viscoelastic and physical properties of articular chondrocytes* Biophysical Journal, 2002. **82**: p. 720-727.
6. Morone, N., Fujiwara, T., Murase, K., Kasai, R. S., Ike, H., Yuasa, S., Usukura, J., Kusumi, A., *Three-dimensional reconstruction of the membrane skeleton at the plasma membrane interface by electron tomography*. The Journal of Cell Biology, 2006. **174**(6): p. 851-862.
7. Chen, C.S., Jiang, X., Whitesides, G. M., *Microengineering the Environment of Mammalian Cells in Culture*. MRS bulletin, 2005. **30**: p. 194-201.
8. Engler, A.J., Sen, S., Sweeney, H. L., Discher, D. E., *Matrix Elasticity Directs Stem Cell Lineage Specification*. Cell, 2006. **126**: p. 677-689.
9. Hochmuth, R.M., *Micropipette aspiration of living cells*. J. Biomech., 2000. **33**: p. 15-22.
10. Worthen, G. S., Schwab, B., Elson, E. L., Downey, G. P., *Mechanics of stimulated neutrophils: cell stiffening induces retension in capillaries*. Science, 1989. **14**: p. 183-186.
11. Redenbach, D. M., English, D., Hogg, J. C., *The nature of leukocyte shape changes in the pulmonary capillaries*. Am. J. Physiol. Lung Cell. Mol. Physiol, 1997. **273**: p. L733-L740.
12. Rosenbluth, M. J., Lam, W.A., Fletcher, D. A., *Force microscopy of nonadherent cells: A comparison of leukocyte cell deformability*. Biophys. J., 2006. **90**: p. 2994-3003.
13. Ozturk, S.S., *Cell culture technology for pharmaceutical and cell-based therapies*, ed. Ozturk, S. S., Hu, W-S. 2006, New York: Taylor & Francis.
14. Jayapal, K. P., Wlaschin, K. F., Yap, M. G. S., Hu, W-S., *Recombinant protein therapeutics from CHO cells - 20 years and counting*. Chem. Eng. Prog 2007. **103**: p. 40-47.
15. Hammond, T. G., Hammond, J. M., *Optimized suspension culture: the rotating-wall vessel*. Am. J. Physiol. Renal Physiol, 2001. **281**: p. F12-F25.
16. Ma, N., Koelling, K.W., Chalmers, J. J., *Fabrication and use of a transient contractional flow device to quantify the sensitivity of mammalian and insect cells to hydrodynamic forces* Biotechnol. Bioeng., 2002. **80**(428-437).
17. Senger, R. S., Karim, M. N., *Effect of shear stress on intrinsic CHO culture state and glycosylation of recombinant tissue-type plasminogen activator protein* Biotechnol. Prog., 2003. **19**: p. 1199-1209.
18. Keane, J. T., Ryan, D., Gray, P. P., *Effect of shear stress on expression of recombinant protein by Chinese hamster ovary cells*. Bioengineering, 2002. **81**: p. 211-220.

19. Gigout, A., Buschmann, M. D., Jolicoeur, M. *Chondrocytes cultured in stirred suspension with serum-free medium containing pluronic-68 aggregate and proliferate while maintaining their differentiated phenotype* Tissue Eng.: Part A 2009. **15**: p. 2237-2248.
20. Lopez, L., Duck, M., Hunt, W. A., *On the Shape of the Erythrocyte*. Biophys. J., 1968. **8**(11): p. 1228-1234.
21. Li, J., Dao, M., Lim, C. T., Suresh, S., *Spectrin-Level Modeling of the Cytoskeleton and Optical Tweezers Stretching of the Erythrocyte*. Biophys. J., 2005. **88**(5): p. 3707-3719.
22. Darling, E. M., Topel, M., Zauscher, S., Vail, T. P., Guilak, F. , *Viscoelastic properties of human mesenchymally-derived stem cells, primary osteoblasts, chondrocytes, and adipocytes* J. Biomech., 2008. **41**: p. 454-464.
23. Mitchison, J.M., Swann, M. M., *The Mechanical Properties of the Cell Surface: I. The Cell Elastimeter*. The Journal of Experimental Biology, 1954. **31**(3): p. 443-460.
24. Rand, R. P., Burton, A. C., *Mechanical Properties of the Red Cell Membrane I. Membrane Stiffness and Intracellular Pressure*. Biophys. J., 1964. **4**: p. 115-135.
25. Rand, R. P., *Mechanical Properties of the Red Cell Membrane II. Viscoelastic Breakdown of the Membrane*. Biophys. J., 1964. **4**: p. 303-316.
26. Evans, E.A., *New Membrane Concept Applied to the Analysis of Fluid Shear- and Micropipette-Deformed Red Blood Cells*. Biophys. J., 1973. **13**: p. 941-954.
27. Schmid-Schoenbein, G. W., Sung, K-L. P., Toezeren, H., *Passive mechanical properties of human leukocytes*. Biophysical Journal, 1981. **36**: p. 243-256.
28. Sung, K-L. P., Dong, C., Schmid-Schoenbein, G. W., Chien, S., Shalak, R., *Leukocyte relaxation properties*. Biophysical Journal, 1988. **54**: p. 331-336.
29. Evans, E., Yeung, A. , *Apparent viscosity and cortical tension of blood granulocytes determined by micropipet aspiration* Biophysical Journal, 1989. **56**: p. 151-160.
30. Crick, F. H. C., Hughes, A. F. W., *The physical properties of cytoplasm: a study by means of the magnetic particle method*. Exp. Cell. Res., 1949. **1**: p. 37-80.
31. Crick, F. H. C., Hughes, A. F. W., *The Physical Properties of Cytoplasm: A Study by Means of the Magnetic Particle Method, Part II. Theoretical Treatment*. Exp. Cell. Res., 1950. **1**: p. 505-533.
32. Wang, N., Ingber, D. E., *Probing transmembrane mechanical coupling and cytomechanics using magnetic twisting cytometry*. Biochem. Cell Biol., 1995. **73**: p. 1-9.
33. Bausch, A.R., Moller, W., Sackmann, E., *Measuring ligand-receptor unbinding forces with magnetic beads: molecular leverage*. Langmuir, 2000. **16**: p. 8984-8993.
34. Ashkin, A., *Acceleration and trapping of particles by radiation pressure*. Phys. Rev. Lett., 1970. **4**: p. 156-159.
35. Ashkin, A., Dziedzic, J. M., Yamane, T., *Optical trapping and manipulation of single cells using infrared laser beams*. Nature, 1987. **330**: p. 769-771.
36. Engelhardt, H., Gaub, H., Sackmann, E., *Viscoelastic properties of erythrocyte membranes in high-frequency electric fields*. Nature, 1984. **307**: p. 378-380.
37. Krueger, M., Thom, F., *Deformability and stability of erythrocytes in high-frequency electric fields down to subzero temperatures* Biophysical Journal, 1997. **73**: p. 2653-2666.
38. Sukhorukov, V., Zimmermann, U., *The effect of electrical deformation forces on the electropermeabilization of erythrocyte membranes in low- and high-conductivity media* J. Membrane Biol., 1998. **163**: p. 235-245.
39. Wong, P. K., Tan, W., Ho, C-M., *Cell relaxation after electrodeformation: effect of latrunculin A on cytoskeletal actin*. J. Biomech., 2005. **38**: p. 529-535.

40. Lim, C. T., Zhou, E.H., Quek, S. T., *Mechanical models for living cells – a review* J. Biomech., 2006. **39**: p. 195-216.
41. Ashkin, A., *Optical trapping and manipulation of neutral particles using lasers* Proc. Natl. Acad. Sci. USA, 1997. **94**: p. 4853-4860.
42. Konig, K., Liang, H., Berns, M. W., Tromberg, B. J., *Cell damage by near-IR microbeams*. Nature, 1995. **377**: p. 20-21.
43. Melcher, J. R., Taylor, G. I., *Electrohydrodynamics: A Review of the Role of Interfacial Shear Stresses*. Annual Review of Fluid Mechanics, 1969. **1**: p. 111-146.
44. Riske, K. A., Dimova, R., *Electro-deformation and -poration of giant vesicles viewed with high temporal resolution*. Biophys. J., 2005. **88**: p. 1143-1155.
45. Friend A. W. , Finch, E.D., Schwan, H. P., *Low-frequency electric-field induced changes in shape and motility of amoebas*. Science, 1975. **187**: p. 357-359.
46. Zimmermann, U., Friedrich, U., Mussauer, H., Gessner, P., Hamel, K., Sukhorukov, V., *Electromanipulation of Mammalian Cells: Fundamentals and Application*. IEEE Trans. Plasma Science, 2000. **28**(1): p. 72-82.
47. Engelhardt, H., Sackmann, E., *On the measurement of shear elastic moduli and viscosities of erythrocyte plasma membranes by transient deformation in high frequency electric fields* Biophysical Journal, 1988. **54**: p. 495-508.
48. Thom, F., *Mechanical properties of the human red blood cell membrane at -15 °C* Cryobiology, 2009. **59**: p. 24-27.
49. Bao, G., Suresh, S., *Cell and molecular mechanics of biological materials*. Nature materials, 2003. **2**: p. 715-725.
50. Madou, M., *Fundamentals of Microfabrication*. 2 ed. 2002, Boca Raton, FL: CRC Press.
51. Chakraborty, S., ed. *Microfluidics and Microfabrication*. 2010, Springer New York. 357.
52. Xia, Y., Whitesides, G. M., *Soft Lithography*. Annual Review of Materials Science, 1998. **28**: p. 153-184.
53. Nguyen, N-T., Wereley, S. T., *Fundamentals and applications of microfluidics*. 2 ed. Microelectromechanical systems series. 2006: Artech House. 497.
54. Gad-el-Hak, M., *MEMS: Introduction and fundamentals*. 2006: CRC/Taylor & Francis. 448.
55. Desai, J. P., Pillarisetti, A., Brooks, A. D., *Engineering Approaches to Biomanipulation*. Annu. Rev. Biomed. Eng., 2007. **9**: p. 35-53.
56. Geschke, O., Klank, H., Tellemann, P., *Microsystem engineering of lab-on-a-chip devices*. 2 ed. 2004: Wiley-VCH. 258.
57. El-Alil, J., Sorger, P. K., Jensen, K. F., *Cells on chips*. Nature, 2006. **442**: p. 403-411.
58. King, K. R., Wang, S., Irimia, D., Jayaraman, A., Toner, M., Yarmush, M. L., *A high-throughput microfluidic real-time gene expression living cell array*. Lab on a Chip, 2007. **7**: p. 77-85.
59. Moraes, C., Chen, J-H., Sun, Y., Simmons, C. A., *Microfabricated arrays for high-throughput screening of cellular response to cyclic substrate deformation*. Lab on a Chip, 2010. **10**(2): p. 227-234.
60. Moraes, C., Wang, G., Sun, Y., Simmons, C. A., *A microfabricated platform for high-throughput unconfined compression of micropatterned biomaterial arrays*. Biomaterials, 2010. **31**(3): p. 577-584.
61. Fricke, H., *The electrical capacity of suspensions with special reference to blood*. J. General Physiol, 1925. **9**: p. 137-152.

62. Schwan, H.P., *Electrical Properties in Tissue and Cell Suspensions*, in *Advances in Biological and Medical Physics*. 1957, Academic Press: New York. p. 147-209.
63. Pohl, H.A., *Dielectrophoresis*. 1978, Cambridge: Cambridge University Press.
64. Neumann, E., Schaefer-Ridder, M., Wang, Y., Hofschneider, P. H., *Gene transfer into mouse lyoma cells by electroporation in high electric fields*. EMBO, 1982. **1**: p. 841-845.
65. Zimmermann, U., *Electric field-mediated fusion and related electrical phenomena*. Biochem. Biophys. Acta 1982. **694**(3): p. 227-277.
66. Pohl, H.A., Hawk, I., *Separation of Living and Dead Cells by Dielectrophoresis*. Science, 1966. **152**(3722): p. 647-649.
67. Pohl, H.A., Crane, J. S., *Dielectrophoresis of Cells*. Biophys. J., 1971. **11**(9): p. 711-727.
68. Becker, F.F., Wang, X-B., Huang, Y., Pethig, R., Vykoukal, J., Gascoyne, P. R. C., *Separation of human breast cancer cells from blood by differential dielectric affinity*. Proc. Natl. Acad. Sci. USA, 1995. **92**: p. 860-864.
69. Huang, Y., Joo, S., Duhon, M., Heller, M., Wallace, B., Xu, X., *Dielectrophoretic cell separation and gene expression profiling on microelectronic chip arrays*. Analytical Chemistry, 2002. **74**: p. 3362-3371.
70. Voldman, J., *A microfabricated dielectrophoretic trapping array for cell-based biological assays*, in *Department of Electrical Engineering and Computer Science*. 2001, Ph.D. Thesis, Massachusetts Institute of Technology: Boston.
71. Rosenthal, A., Taff, B. M., Voldman, J., *Quantitative modeling of dielectrophoretic traps*. Lab on a Chip, 2006. **6**: p. 508-515.
72. Suehiro, J., Pethig, R., *The dielectrophoretic movement and positioning of a biological cell using a three-dimensional grid electrode system*. J. Phys. D: Appl. Phys. , 1998. **31**: p. 3298-3305.
73. Müller, T., Gradl, G., Howitz, S., Shirley, S., Schnelle, T., Fuhr, G., *A 3-D microelectrode system for handling and caging single cells and particles*. Biosens. Bioelec. , 1999. **14**: p. 247-256.
74. Pethig, R., *Dielectrophoresis: Status of theory, technology, and applications*. Biomicrofluidics, 2010. **4**: p. 022811.
75. Sale, A. J. H., Hamilton, W. A., *Effects of high electric fields on microorganisms*. Biochem. Biophys. Acta, 1967. **148**(3): p. 781-788.
76. Neumann, E., *The relaxation hysteresis of membrane electroporation*, in *Electroporation and Electrofusion in Cell Biology*, A. E. Sowers and C.A. Jordan, Eds. 1989, Plenum Press: New York.
77. Kotnik, T., Mir, L. M., Flisar, K., Puc, M., Miklavčič, D., *Techniques of signal generation required for electroporation*. Survey of electroporation devices. Bioelectrochemistry, 2001. **54**: p. 83-90.
78. Puc, M., Čorović, S., Flisar, K., Petkovšek, M., Nastran, J., Miklavčič, D., *Techniques of signal generation required for electroporation*. Survey of electroporation devices. Bioelectrochemistry, 2004. **64**: p. 113-124.
79. Lundqvist, J. A., Sahlin, F., Aberg, M. A., Stromberg, A., Eriksson, P. S., Orwar, O., *Altering the biochemical state of individual cultured cells and organelles with ultramicroelectrode*. Proc. Natl. Acad. Sci. USA, 1998. **95**: p. 10356-10360.
80. Khine, M., Lau, A., Ionescu-Zanetti, C., Seo, J., Lee, L. P., *A single cell electroporation chip*. Lab on a Chip, 2005. **5**: p. 38-43.

81. Fox, M. B., Esveld, D. C., Valero, A., Luttge, R., Mastwijk, H. C., Bartels, P. V., van den Berg, A., Boom, R. M., *Electroporation of cells in microfluidic devices: a review*. Anal. Bioanal. Chem, 2006. **385**: p. 474-485.
82. Lee, S-W., Tai, Y-C., *A micro cell lysis device*. Sens. Actuators A : Physical 1999. **73**: p. 74-79.
83. McClain, M. A., Culbertson, C. T., Jacobson, S. C., Allbritton, N. L., Sims, C. E., Ramsey, J. M., *Microfluidic devices for the high-throughput chemical analysis of cells*. Anal. Chem., 2003. **75**: p. 5646-5655.
84. Suehiro, J., Hatano, T., Shutou, M., Hara, M., *Improvement of electric pulse shape for electroporation-assisted dielectrophoretic impedance measurement for high sensitive bacteria detection*. Sens. Actuators B: Chemical 2005. **109**: p. 209-215.
85. Heida, T., Wagenaar, J.B.M., Rutten, W. L. C., Marani, E., *Investigating membrane breakdown of neuronal cells exposed to nonuniform electric fields by finite-element modeling and experiments*. IEEE Trans. Biomed. Eng., 2002. **49**: p. 1195-1203.
86. Gowrishankar, T. R., Stewart, D. A., Weaver, J. C., *Model of a confined spherical cell in uniform and heterogeneous applied electric fields*. Bioelectrochemistry, 2006. **68**: p. 181-190.
87. Engelhardt, H., *Manipulation einzelner Zellen mit Hochfrequenzfeldern: eine empfindliche Methode zur Messung viskoelastischer Parameter und zum Nachweis subtiler struktureller Änderungen der Plasmamembran von Erythrozyten*, in *Physics*. 1987, Technical University Munich: Munich.
88. Ferry, J.D., *Viscoelastic Properties of Polymers*. 3 ed. 1980, New York: John Wiley and Sons.
89. Hu, X., Arnold, W. M., Zimmermann, U., *Alterations in the electrical properties of T and B lymphocyte membranes induced by mitogenic stimulation. Activation monitored by electro-rotation of single cells*. Biochim. Biophys. Acta 1990. **1021**: p. 191-200.
90. Müller, K.J., Sukhorukov, V. L., Zimmermann, U., *Reversible Electroporation of Mammalian Cells by High-Intensity, Ultra-Short Pulses of Submicrosecond Duration*. Journal of Membrane Biology 2001. **184**(2): p. 161-170.
91. Kim, D-H., Wong, P. K., Park, J., Levchenko, A., Sun, Y., *Microengineered Platforms for Cell Mechanobiology*. Annu. Rev. Biomed. Eng, 2007. **11**: p. 203-233.
92. Pauly, H., Schwan, H. P., *The Impedance of a Suspension of Spherical Particles Surrounded by a Shell*. ZS. f. Naturforschung, 1959. **14b**: p. 125-131.
93. Irimajiri, A., Hanai, T., Inouye, V. A., *A Dielectric Theory of "Multi-Stratified Shell" Model with its Application to a Lymphoma Cell* J. Theor. Biol., 1979. **78**: p. 251-269.
94. Huang, Y., Holzel, R., Pethig, R., Wang, X-B., *Differences in the AC electrodynamics of viable and non-viable yeast cells determined through combined dielectrophoresis and electrorotation studies*. Phys. Med. Biol., 1992. **37**(7): p. 1499-1517.
95. Jones, T.B., *Electromechanics of particles*. 1996, Cambridge: Cambridge University Press.
96. Desprat, N., Richert, A., Simeon, J., Asnacios, A. , *Creep function of a single living cell* Biophys. J., 2005. **88**: p. 2224-2233.
97. Hughes, M.P., *Nanoelectromechanics in Engineering and Biology*. 2002, CRC Press: Boca Raton, FL.
98. Penman, S., *Rethinking cell structure*. Proc. Natl. Acad. Sci. USA, 1995. **92**: p. 5251-5257.

99. Yarmola, E.G., Somasundaram, T., Boring, T. A., Spector, I., Bubb, M. R., *Actin-latrunculin A structure and function. Differential modulation of actin-binding protein function by latrunculin A*. J. Biol. Chem, 2000. **275**(36): p. 28120-28127.
100. Sager, P.R., *Cytoskeletal effects of acrylamide and 2,5-hexanedione: selective aggregation of vimentin filaments*. Toxicol. Appl. Pharmacol., 1989. **97**(1): p. 141-155.
101. Arocena, M., *Effect of acrylamide on the cytoskeleton and apoptosis of bovine lens epithelial cells*. Cell Biology International, 2006. **30**(12): p. 1007-1012.
102. Blain, E.J., Gilbert, S. J., Hayes, A. J., Duance, V. C., *Disassembly of vimentin cytoskeleton disrupts articular chondrocyte homeostasis*. Matrix Biology, 2006. **25**(7): p. 398-408.
103. Fung, Y.C., *Biomechanics: Mechanical Properties of Living Tissues*. 2 ed. 1993, New York: Springer-Verlag.
104. Zimmermann, U., ed. *Electromanipulation of Cells*. 1996, CRC Press: Boca Raton, FL.
105. Tresset, G., Takeuchi, S., *A Microfluidic Device for Electrofusion of Biological Vesicles*. Biomedical Microdevices, 2004. **6**(3): p. 213-218.
106. Tinevez, J-Y., Schulze, U., Salbreux, G., Roensch, J., Joanny, J-F., Paluch, E., *Role of cortical tension in bleb growth*. Proc. Natl. Acad. Sci. USA, 2009. **106**(44): p. 18581-18586.
107. Aspengren, S., Wielbass, L., Margareta, W., *Effects of acrylamide, latrunculin, and nocodazole on intracellular transport and cytoskeletal organization in melanophores*. Cell Motility and the Cytoskeleton, 2006. **63**(7): p. 423-436.
108. Correia, I., Chu, D., Chou, Y. H., Goldman, R. D., Matsudaira, P., *Integrating the actin and vimentin cytoskeletons. adhesion-dependent formation of fimbrin-vimentin complexes in macrophages*. J. Cell Biol., 1999. **146**(4): p. 831-842.
109. Capote, C., Maccioni, R. B., *The association of tau-like proteins with vimentin filaments in cultured cells*. Exp. Cell. Res., 1998. **239**(2): p. 202-213.
110. Isenberg, G., Goldmann, W. H., *Actin-membrane coupling: A role for talin*. J. Muscle Res. Cell Motility, 1992. **13**(6): p. 587-589.
111. Otey, C.A., Burridge, K., *Patterning of the membrane cytoskeleton by the extracellular matrix*. Semin. Cell Biol., 1990. **1**(5): p. 391-399.
112. Turner, C.E., Burridge, K., *Transmembrane molecular assemblies in cell-extracellular matrix interactions*. Curr. Opin. Cell Biol., 1991. **3**(5): p. 849-853.
113. Graham, F.L., Smiley, J., Russell, W. C., Nairn, R., *Characteristics of a human cell line transformed by DNA from human adenovirus 5*. J. Gen. Virol., 1977. **36**(1): p. 59-74.
114. Shaw, G., Morse, S., Ararat, M., Graham, F. L., *Preferential transformation of human neuronal cells by human adenoviruses and the origin of HEK 293 cells*. FASEB J., 2002. **16**(8): p. 869-871.
115. Sundstrom, C., Nilsson, K., *Establishment and characterization of a human histiocytic lymphoma cell line (U-937)*. Int. J. Cancer 1976. **17**: p. 565-577.
116. Sims, C. E., Allbritton, N.L., *Analysis of single mammalian cells on-chip Lab on a Chip*, 2007. **7**: p. 423-440.
117. Liu, Y., Liu, W-K., Belytschko, T., Patankar, N., To, A-C., Kopacz, A., Chung, J-H., *Immersed electrokinetic finite element method*. Int. J. Numer. Meth. Engng., 2007. **71**: p. 379-405.

APPENDIX 1. PECVD of Nanocrystalline Si Layers on High T_g Polymer Substrates

Citation: MacQueen, L. A., Zikovsky, J., Dennler, G., Latreche, M., Czeremuszkin, G., Wertheimer, M. R. (2006) PECVD of nanocrystalline Si layers on high- T_g polymer substrates. *Plasma Processes and Polymers*. 3: 58-65

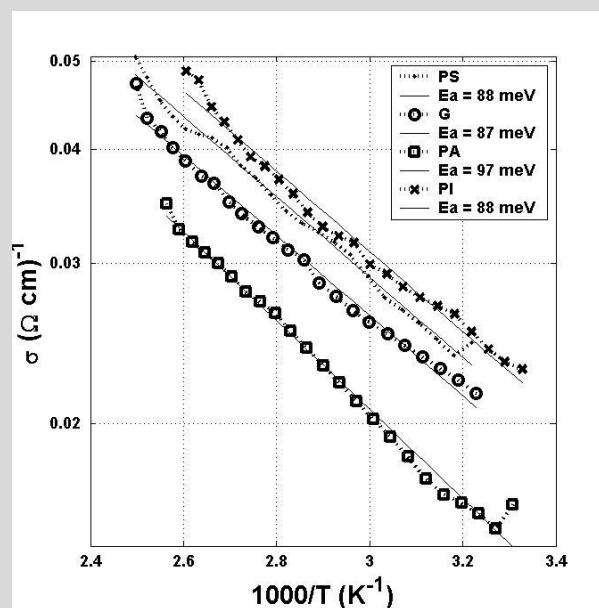
L. MacQueen¹, J. Zikovsky¹, G. Dennler², M. Latreche³, G. Czeremuszkin³, and M. R. Wertheimer^{1}.*

¹ Groupe des Couches Minces and Department of Engineering Physics, École Polytechnique, Montréal, QC, Canada

² Linz Institute for Organic Solar Cells (LIOS), Johannes Kepler University, Linz, Austria

³ Nova-Plasma Inc., Montréal, QC, Canada

Summary: Hydrogenated nanocrystalline silicon (nc-Si:H) was deposited by plasma-enhanced chemical vapor deposition (PECVD) on transparent polymers in order to qualify these for possible use as electronic substrates. As a first step, plasma etch experiments in pure H_2 revealed small etch rates for these materials. Thin films of nc-Si:H were then deposited on samples placed on the grounded electrode of a “Reinberg”-type parallel plate RF (13.56 MHz) PECVD reactor, at various substrate temperatures ($25\text{ °C} \leq T_s \leq 250\text{ °C}$), using SiH_4 diluted in H_2 as the feed-gas. Thermally induced failure of the nc-Si:H/polymer composite was avoided within a certain range of deposition conditions, permitting structural and electrical characterization of the deposits.



Temperature-dependent conductivity, $\sigma(T)$, for nanocrystalline silicon (nc-Si:H) films on glass and three polymer substrates, all deposited at $T_s=175\text{ °C}$.

1. Introduction

Electronic devices on flexible polymer substrates are becoming increasingly important, for example in displays, photovoltaic cells, etc. The advantages of using polymer substrates instead of glass for electronic applications include light weight, flexibility and conformability, and low cost with the possibility of roll-to-roll processing (large-area electronics). So far, the adoption of polymers for electronic applications has been slow due to their limited compatibility with semiconductor fabrication processes. In particular, the relatively high linear expansion coefficient, α , and low glass transition temperature, T_g , of most polymers limit their use to temperatures below 300°C. Several high- T_g polymers ($220^\circ\text{C} < T_g < 330^\circ\text{C}$) with optical transparency, good chemical resistance and barrier properties have recently been developed for use in organic (OLED) display technology [1, 2], and these have motivated the present research.

For many applications, thin film transistor (TFT) matrix arrays are required, for example to drive the individual pixel elements of a display [3, 4]. Hydrogenated amorphous silicon (a-Si:H) is a low-temperature material which is presently used as a TFT semiconductor, but its inherently low charge carrier mobility limits the density at which TFTs can be laid out. Better nano-structural control of low-temperature Si films is therefore required to increase TFT density and to reduce operating power of TFT-based devices. Silicon can be deposited as various structural phases ranging between a-Si and the fully crystalline state (c-Si); these include nanocrystalline (nc-Si), microcrystalline ($\mu\text{c-Si}$), and polycrystalline (pc-Si) materials. The first two (nc-Si and $\mu\text{c-Si}$) comprise an a-Si matrix in which are dispersed many tiny crystallites (small volumes of c-Si), the “nano” and “micro” prefixes indicating the mean crystallite size. Pc-Si refers to a material that is devoid of the amorphous matrix, the crystallites being separated by abrupt grain boundaries. Although c-Si and pc-Si possess high carrier mobility in comparison to a-Si, they are brittle and inflexible, unlike a-Si. Furthermore, as transistor dimensions are reduced, conductivity anisotropy within the pc-Si material becomes problematic.

Nanocrystalline silicon (nc-Si:H) is a preferred semiconductor for fabricating TFTs, and deposition by plasma-enhanced chemical vapor deposition (PECVD) is particularly advantageous when using temperature-sensitive substrate materials. With PECVD, the crystalline volume fraction of as-deposited Si films can be varied between 0 and close to 100% within a useful range of “low” substrate temperatures, T_s [5-7], eliminating the requirement of post-deposition laser or thermal annealing. The objective of the present research has, therefore, been to deposit nc-Si:H films at the lowest possible T_s values, and to characterize their structural and electrical properties. No coatings were deposited before or after the nc-Si:H, which was deposited directly on the various substrates in order to simplify the estimation of stress values induced within the film-substrate (f-s) structure. Such stress values, resulting from differential thermal expansion, α , can be correlated with results of structural and electrical measurements. In order to reduce possible contamination of nc-Si:H by unwanted “dopant” elements (C, O, N, etc) arising from substrate ablation (etching) during PECVD, we first performed etching experiments in order to identify the optimal conditions for high-quality nc-Si:H film growth.

2. Experimental Methodology

2.1. Etching and Deposition Experiments

Etching and deposition experiments were performed in a “Reinberg-type” parallel-plate RF-PECVD reactor, operating at 13.56 MHz (Fig. 1). The ranges of operating parameters selected and the reasons for these choices will be clarified later in this text. The substrate materials used in this research and some of their key properties for this work (α and T_g) are presented in Table 1. Since nc-Si:H films must not be contaminated by unwanted impurities, the polymer substrates must be resistant towards ablation (etching) in H_2 -rich plasma during the PECVD process. It was, therefore, deemed necessary to investigate possible etching of the polymer substrates as a preliminary step. Etch rates were determined by partially masking the substrates with 50 nm Au layers before exposing them to H_2 plasma at various RF power densities ($50 \text{ mW/cm}^2 < P < 500 \text{ mW/cm}^2$), and then profiling the etched areas by Atomic Force Microscopy (AFM). Such experiments were carried out with the substrates on the grounded or powered electrodes. The above-noted variation in P was then repeated, this time with a certain fixed concentration, C_{SiH_4} , of SiH_4 added to the H_2 (SiH_4 concentration, $C_{SiH_4} = [SiH_4]/([SiH_4] + [H_2]) = 6.25\%$). The resulting a-Si:H films were used for comparing deposition rates to etch rates.

In the case of nc-Si:H deposition experiments, P was maintained at 50 mW/cm^2 , with substrates placed on the grounded electrode only. The SiH_4 and H_2 partial pressures were maintained constant at 8 mTorr and 120 mTorr, respectively ($C_{SiH_4} = 6.25\%$), the chamber pressure was always $p = 150 \text{ mTorr}$ (20 Pa), while the substrate temperature, T_s , was varied between 25°C and 250°C . Typical deposition durations were 200 minutes, and film thicknesses, d_f , measured by variable angle spectroscopic ellipsometry (VASE, J. Woollam & Co.), were $120 \pm 15 \text{ nm}$.

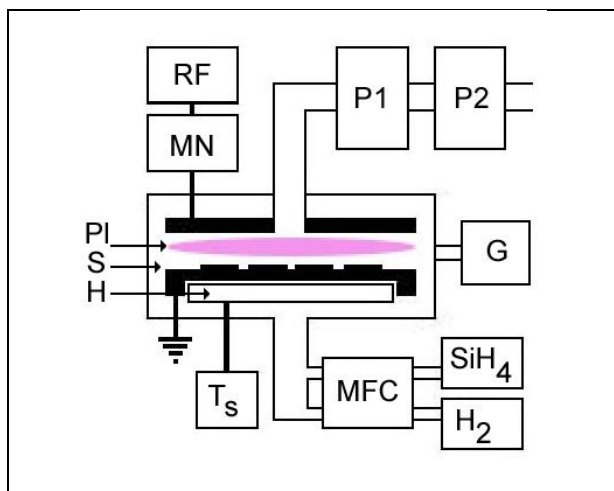


Figure 1. Schematic of RF-PECVD system: RF: 13.56 MHz Power Supply; MN: Matching Network; P1: Turbo Molecular Pump; P2: Rotary Pump; G: Pressure Gauge; T_s : Temperature Control; MFC: Mass Flow Control; Pl: Plasma; S: Substrates; H: Heater.

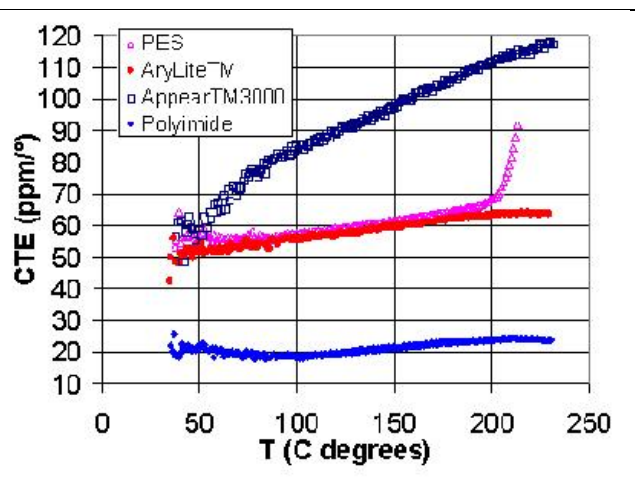


Figure 2. Coefficient of thermal expansion, α , (ppm/ $^\circ$) of four high- T_g polymers versus T . From ref. [1], with permission.

Table 1. Properties of the substrate materials investigated

Substrate	Source/Manufacturer [2]	Symbol	T _g (°C)	α (ppm/°C)*
APPEAR [®] (cyclic polyolefin)	Promerus LLC	PO	330	60 + T/4
ARYLITE [®] (polyarylate)	Ferrania Imaging Technologies.	PA	325	50 + T/15
SUMILITE [®] (polyether sulfone)	Sumitomo Bakelite Co. Ltd.	PS	223	50 + T/14
KAPTAN [®] (polyimide)	DuPont de Nemours & Co.	PI	360	20
Glass (Corning 2947)	Corning Inc.	G	-	9
* T-dependent α values are linear approximations of data from ref. [1].				

2.2. Differential Thermal Expansion

The maximum value of T_s at which we could deposit nc-Si:H films on the substrates in Table 1 was mainly limited by the differences in thermal expansion coefficients, α, of the deposited Si films, α_f, and the substrates, α_s (see Fig. 2 and Table 1). Substrates were heated (dT_s/dt ~ 1°C/min) and held at the selected value of T_s for 30 minutes prior to film deposition. Precautions were taken to limit the amount of structural relaxation (for example, buckling or rolling) of the film-substrate (f-s) composite during deposition, and the PECVD chamber was gradually returned to ambient conditions (dT_s/dt ~ -1°C/min) after the deposition had terminated. The differential thermal contraction between the substrates and the film deposits can be approximated by

$$\delta = (\alpha_s - \alpha_f)\Delta T, \quad (1)$$

where α_s and α_f are the respective coefficients of thermal expansion. Since the thicknesses, d, of our nc-Si:H deposits were typically at least a thousand times less than those of the substrates, stress relaxation of the f-s composite gave rise to curvature. When d_s/d_f ~ 10³ such as in the present case, this phenomenon may be expected to obey the Stoney formula up to Y_f/Y_s ≈ 100, where Y is Young's modulus [8]; this condition is not always met when using polymer substrates, since Y_f ≈ 150-200 GPa [9] and 1.9 < Y_s < 5 GPa [1]. However, since $\frac{d_s Y_s}{d_f Y_f} > 10$, we

can use the following expression to estimate the compressive stress in the film due to differential thermal contraction [10]:

$$s_f = \frac{Y_f \delta}{(1 - \nu_f)}, \quad (2)$$

where ν_f is Poisson's ratio of nc-Si:H. Films deposited on PO, the polymer with by far the highest α_s value (see Fig.2 and Table 1), were observed to delaminate at $T_s \geq 200$ °C; in this particular case, the compressive strain $\alpha_s \Delta T \approx 1.7\%$ resulted in a stress $s_f \approx 3.6$ GPa, a value that clearly exceeded the f-s interfacial adhesion strength. These may, therefore, be considered the limiting conditions for successful deposition of stable nc-Si:H film coatings.

2.3 Physico-chemical Characterization of Si Deposits

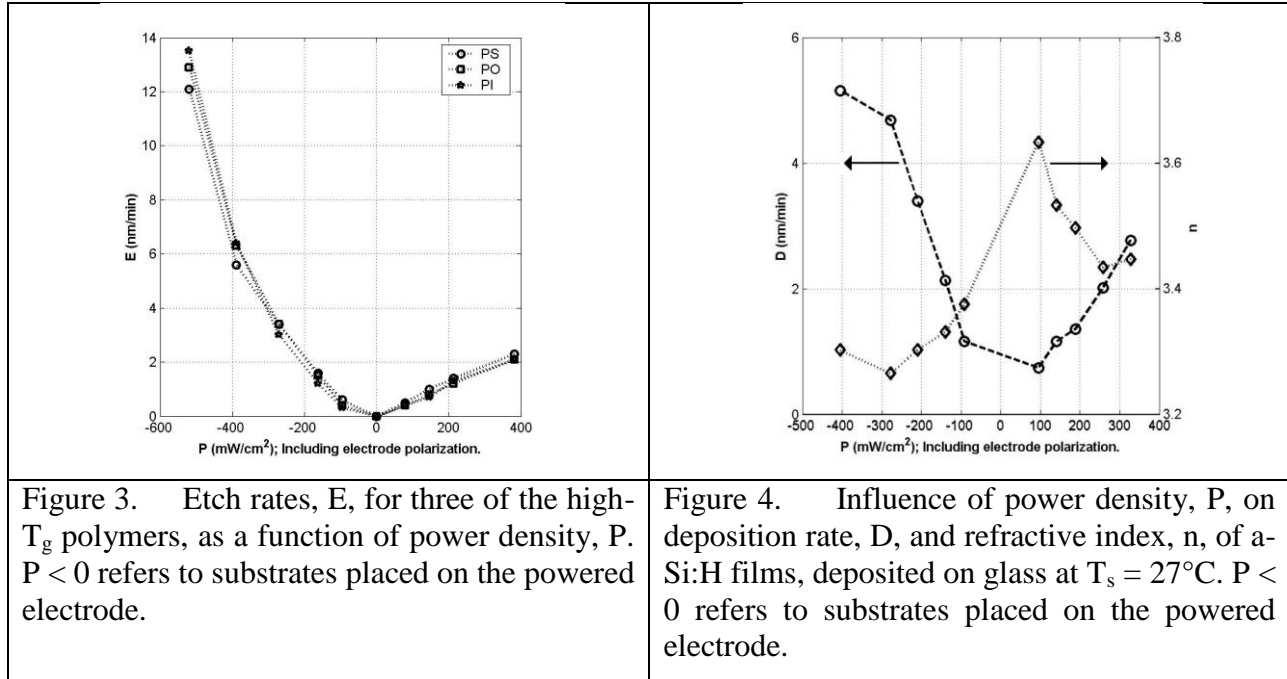
Thin Si deposits were subjected to both structural and electrical characterizations, primarily by micro-Raman spectroscopy (MRS) and by DC conductivity measurements, respectively. MRS was used to estimate the crystalline volume fractions, X_c , of the films by comparing the areas under Raman peaks corresponding to the crystalline (c) and amorphous (a) transverse optical lattice vibrations (c-TO and a-TO) [11-17]. We used an argon-ion laser, $\lambda=514$ nm, in the Stokes configuration, and calibrated the measured spectra with a c-Si sample displaying a c-TO peak centered at 520.5 cm^{-1} with a full width at half-maximum (FWHM) of 3.886 cm^{-1} . Data analysis (spectral deconvolution and area integration) was done using BOMEM GRAMS/32 software (Galactic Industries Co., Salem, NH).

DC conductivity measurements were performed by the four-point-probe method [18], with samples mounted on a temperature-controlled substrate holder and using computerized data acquisition. This system, that allowed us to measure sheet conductivity during repeated thermal cycling, comprised a Keithley 220 programmable current source, an Agilent 34401A multimeter, and a Tempronix temperature controller; probe tip spacings and radii were 1.59 mm and 17.8 μm , respectively. For the case of very low conductivity samples ($\sigma < 10^{-6}$ S/cm), planar aluminum electrodes (with a 100 μm gap) were evaporated on the Si films, and measurements were carried out under vacuum.

3. Results and Discussion

3.1. Etching and Deposition Experiments

Figure 3 presents etch rates, E , of three of the present polymers in pure H_2 plasma, samples being placed either on the grounded or the powered electrodes. Significantly higher etch rates are seen to occur on the powered electrode ($P < 0$, in Fig. 3) on account of d.c.-bias induced ion bombardment [19]. E values were very small for the case of low power densities ($|P| < 50$ mW/cm^2), especially in the absence of energetic ion bombardment, on the grounded electrode. Figure 4 presents the influence of P on the deposition rate, D , and the refractive index, n , of a-Si:H films, deposited at $T_s = 27$ °C on glass. Dense films (high n values) with low concentrations of voids and other defects are produced in the low- P (low- D) regime, substrates being placed on the grounded electrode.



3.2. Raman Spectroscopy

Micro-Raman spectroscopy (MRS) is a non-destructive optical technique that can be used to analyze structural properties of semiconductors [11-17]. In silicon, the transverse optical (TO) vibration modes differ between c-Si and a-Si:H materials. Within a multiphase material, for example nc-Si:H, we can estimate the crystalline volume fraction, X_c , by comparing the contributions from the “c” and “a” peaks. Further information can also be derived from the center frequency positions, ω , and the full widths at half-maximum (FWHM), Γ , of the peaks, as will be discussed below. X_c can be estimated using the formula [11]:

$$X_c = \frac{I_c + I_{gb}}{I_c + I_{gb} + y(L)I_a}, \quad (3)$$

where I_c , I_{gb} , and I_a are the integrated intensities of (or areas under) the “crystalline”, intermediate (grain boundary), and “amorphous” peaks, respectively (see Fig. 5 and Table 2). The weighting function, $y(L)$, is the ratio of the scattering cross-section of c-Si to a-Si:H, which depends on the excitation wavelength, λ , and the grain size, L ; according to Bustarret et al [11], $y(L) = 0.1 + \exp(-L/250)$; in other words, y is close to unity, $0.9 < y(L) < 1.1$ for the case of small grain sizes ($0 < L < 20$ nm). Since the deposition conditions used here are known to lead to L values < 20 nm [5-7], we have used $y = 1$ in our calculations, the results of which appear in Fig.

6. Figure 6 represents a plot of X_c vs. T_s : films are seen to be essentially amorphous ($X_c \approx 0$) for $T_s < 100^\circ\text{C}$, but the crystalline fraction, X_c , then rises near-linearly with increasing T_s values. The majority of our nc-Si:H films, corresponding to deposits made at $150^\circ\text{C} \leq T_s \leq 225^\circ\text{C}$, show a maximum X_c of ~ 0.5 . Increasing either T_s or the deposition duration (film thickness) resulted in unstable film-substrate composite structures, as will be discussed later.

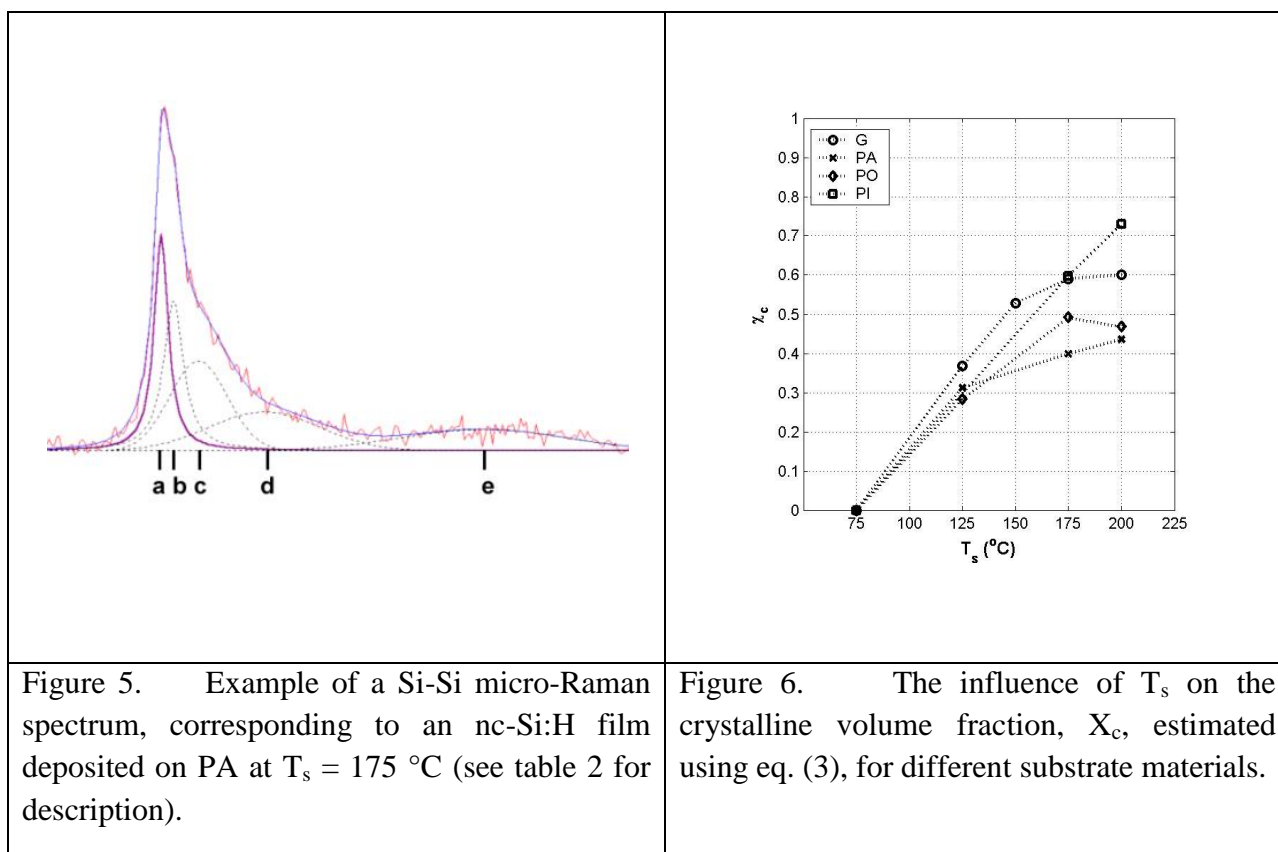


Table 2. Data analysis of the micro-Raman spectrum shown in Fig. 5.

Symbol	ω_0 (cm^{-1})	Γ (cm^{-1})	Peak assignment	Reference
a	520	4-15	c-Si TO	[11-17]
b	494-510	20-30	gb-Si	[12, 13]
c	480	45-80	a-Si:H TO	[11-17]
d	440	~ 100	a-Si:H LO	17
e	330	~ 120	a-Si:H LA	17

The measured peak-center positions, ω , and FWHM, Γ , of our a-Si:H and nc-Si:H samples vary considerably, depending on the chosen substrate material and T_s . For the c-TO peak $\omega = 516 \pm 4 \text{ cm}^{-1}$ and $\Gamma = 13 \pm 3 \text{ cm}^{-1}$, while for the a-TO peak $\omega = 485 \pm 10 \text{ cm}^{-1}$ and $\Gamma = 55 \pm 10 \text{ cm}^{-1}$. Onset of the intermediate peak (Table 2, symbol b) coincided with that of the crystalline peak; its ω and Γ values were $\omega = 503 \pm 4 \text{ cm}^{-1}$ and $\Gamma = 25 \pm 5 \text{ cm}^{-1}$. A full examination of this data will not be presented here due to the many film properties and measurement conditions which can affect ω and Γ . Some of these factors include: (i) the size and shape of crystallites [14], (ii) the local temperature of the measured volume, T_m , [15] which can be raised by the probe laser, and (iii) residual stresses (both intrinsic and extrinsic) which are variable throughout the film thickness [16].

3.3 DC Conductivity

The electrical conductivity of semiconducting materials such as nc-Si:H, $\sigma(T)$, is thermally activated and therefore obeys the Arrhenius relation:

$$\sigma(T) = \sigma_0 \exp\left(\frac{-E_a}{kT}\right), \quad (4)$$

where σ_0 is the pre-exponential factor, E_a is the so-called activation energy, and k is Boltzmann's constant. For the case of nc-Si:H films grown directly on plastic substrates, the temperature dependence of $\sigma(T)$ is also influenced by stress in the film resulting from the differential thermal expansion between it and the substrate [8-10]. After repeated thermal cycles, excessive stresses may result in failure (cracking and delamination of the nc-Si:H) of the f-s composite. Figures 7 and 8 present $\sigma(T)$ data for nc-Si:H films on PA and PO substrates, respectively, measured while continuously heating and cooling the composites ($dT/dt = 3^\circ\text{C}/\text{min}$) within a range of temperatures, $40^\circ\text{C} < T < 120^\circ\text{C}$. "Good" f-s composite structures display the expected near-linear behavior (Fig. 7), while a highly non-linear behaviour is observed for the case of nc-Si:H/PO (Fig. 8). Values of σ and E_a for "good" nc-Si:H films grown at particular fixed conditions were always found to be very similar, independent of whether they were deposited on polymers or on glass. "Arrhenius-like" behavior within the specified T range was observed for all films deposited at $T_s \leq 175^\circ\text{C}$, except for those grown on the PO substrate. The reason for this "anomaly" is the following: As shown in Fig. 2, APPEAR[®] (PO) undergoes a structural transition at $T \approx 60^\circ\text{C}$ that gives rise to rapidly increasing $\alpha(T)$ values above that temperature. As a result, stress values in the nc-Si:H deposits on this substrate increase concomitantly with rising T, and this gives rise to the hysteretic, non-Arrhenius behavior observed in Fig. 8. For the case of all other substrate materials, α is either constant or only mildly T-dependent (see Fig. 2 and Table 1) so that this "anomaly" does not occur. The series of near-parallel linear curves in Fig. 7, which eventually stabilize to a single, reproducible one, result from gradual relaxation of the residual stresses in the polymer that originate from the manufacturing process.

In Fig. 9 we present a series of Arrhenius plots corresponding to different substrate materials (PS, PA, PI and glass), in all cases following mechanical relaxation of possible stresses in the substrates, and all nc-Si:H films having been deposited under identical conditions at $T_s = 175^\circ\text{C}$. Clearly, the curves are all parallel ($E_a = 92 \pm 5 \text{ meV}$), but the $\sigma(T')$ values can differ by a factor of about 1.5 for any given T' value. For easier comparison with data from the literature, we shall

focus our attention on our data pertaining to the Corning 2947 glass substrate material: Figure 10 shows plots of $\sigma(300\text{K})$, values measured at 300K, versus the corresponding apparent E_a values, along with similar plots drawn from the literature [7, 20]. Even though the latter correspond to significantly different fabrication conditions (for example, Ram et al [7] used SiF_4 as their Si feed gas, instead of SiH_4), the three data sets are remarkably similar. Figures 11 and 12 show plots of $\sigma(300\text{K})$ and of E_a values versus T_s and X_c , respectively, for the present a-Si:H and nc-Si:H deposits, again on the Corning 2947 glass substrates. Like the data displayed in Fig. 10, these illustrate the remarkable range of property variations, their systematic dependence on T_s (or X_c , itself strongly dependent on T_s), and their excellent reproducibilities achieved in the current research. Although the data are not shown here (other than in the example of Fig. 9), similar results were also obtained with the “well-behaved” polymer substrates, that is, all but PO.

As mentioned in connection with Fig. 10, the present data correlate well with those in the literature, but only if one takes into account the “normal” existence of oxygen doping of the nc-Si:H at the ppm level. This is known to occur on account of trace quantities of O_2 and H_2O in the reactor, and its extent depends on X_c since oxygen is reported to migrate preferentially within the grain boundaries [21]. Torres et al [21] demonstrated that O-doping could only be avoided by taking extraordinary measures for assuring purity of the feed gas and of the reactor system.

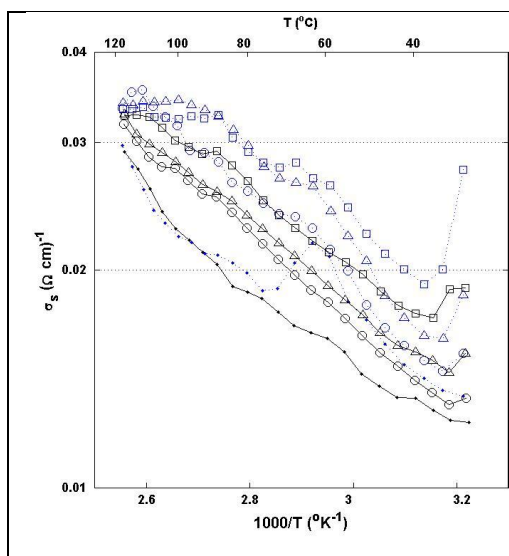


Figure 7. $\sigma(T)$ values for nc-Si:H films deposited at $T_s = 175^\circ\text{C}$ on PA, during four cycles within the temperature range: ($40^\circ\text{C} < T < 120^\circ\text{C}$).

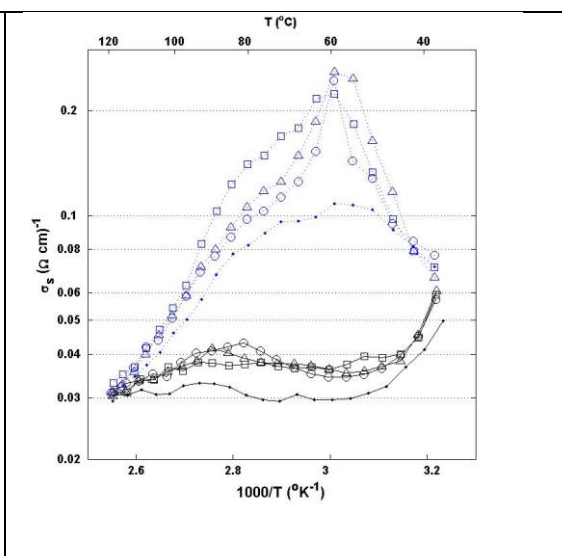


Figure 8. $\sigma(T)$ values for nc-Si:H films deposited at $T_s = 175^\circ\text{C}$ on PO, during four cycles through the temperature range: ($40^\circ\text{C} < T < 120^\circ\text{C}$).

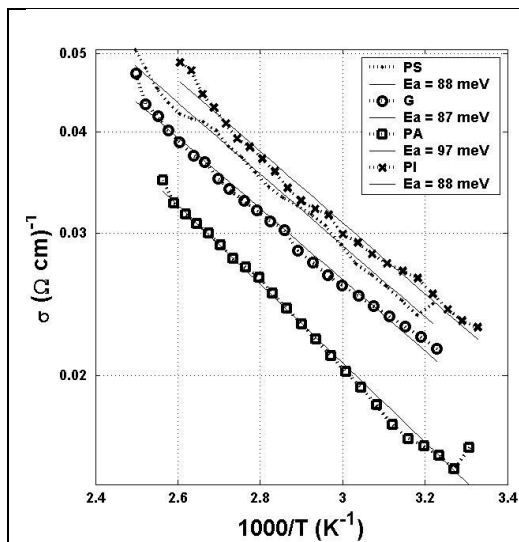


Figure 9. Arrhenius plots for nc-Si:H films on glass and on three polymer substrates, all deposited at $T_s=175^\circ\text{C}$.

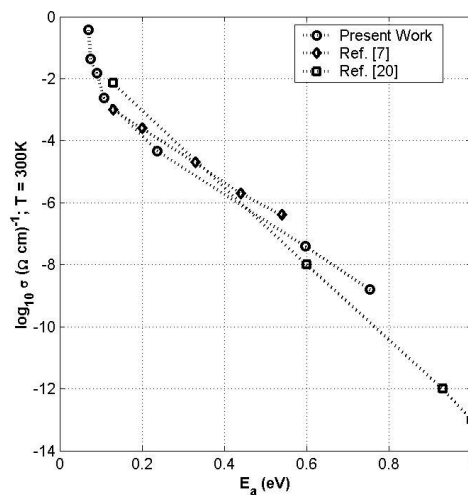


Figure 10. Plots of σ values measured at 300K versus the corresponding apparent E_a values, for the present work and data from the literature [7, 20]; all data pertain to glass substrates.

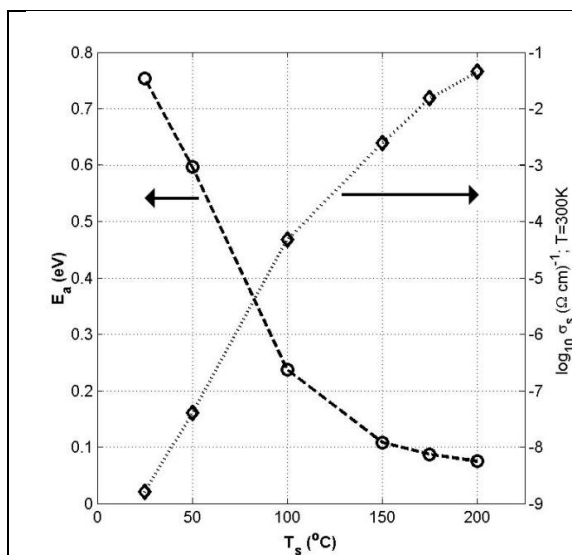


Figure 11. Plots of $\sigma(300\text{K})$ and of E_a values versus substrate temperature, T_s , at which the nc-Si:H films were deposited, for the case of Corning 2947 glass substrate material.

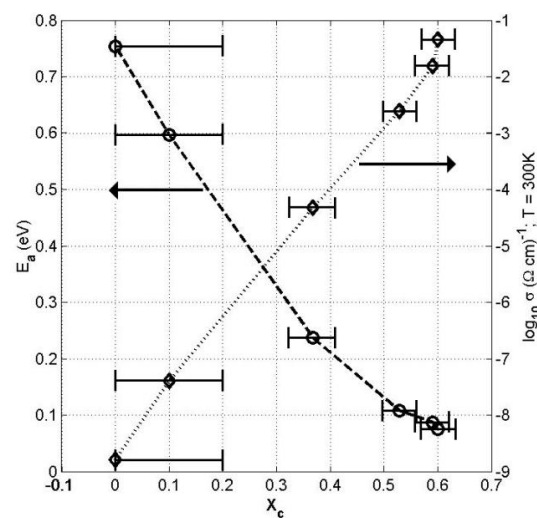


Figure 12. Plots of $\sigma(300\text{K})$ and of E_a values versus the films' crystalline volume fraction, X_c , for the case of nc-Si:H films deposited on Corning 2947 glass.

4. General Discussion and Conclusions

Like the present work, other earlier research [5-7] also had an objective to elucidate the micro-structural evolution of thin Si films, deposited by PECVD from SiH₄ mixtures highly diluted in H₂, for the most part using silica or c-Si substrates. With a suitable choice of C_{SiH4} (between 5% and 8%, 6.25% in the present case) it was found that the microstructure of deposited films can be effectively controlled by varying a single parameter, T_s [5-7]. The present micro-structural and electrical results also clearly demonstrate that a very wide range of material properties can be achieved simply by varying T_s within the range tolerated by the current substrate materials (T_s < 250°C). The first appearance of nanocrystalline structure (detected by MRS) occurred at T_s = 100 ± 10°C (Fig. 6). Thermal expansion of these substrates has clearly been our greatest challenge for the development of highly stable film-substrate composite structures. Compressive strains ($\alpha_s \Delta T \approx 1.7\%$) and compressive stress values $s_f \approx 3.6 \text{ GPa}$, have been identified as those that clearly exceeded the adhesive strength of the nc-Si:H/PO interface, when T_s ≥ 200 °C. Although highly stressed samples (PO substrate, T_s = 175 °C) were not observed to immediately delaminate, their $\sigma(T)$ behavior was hysteretic (Fig. 8), and they eventually did delaminate after numerous thermal cycles (~10 cycles of ~8 hours per cycle). The large majority of nc-Si:H films on polymers nevertheless showed resilience, as evidenced by the stability of their electrical behaviors (linear Arrhenius plots for nc-Si:H on all substrates other than PO), even when repeatedly subjected to ~ GPa stresses, both in tension and compression, for example during continuous thermal cycling for periods in excess of 80 hours. Like Angiolini et al [1], we are therefore confident that the results presented here “point to the successful fabrication of high-performance TFT arrays on plastic substrates”.

The high-T_g polymers we have used here as substrates fulfill certain important requirements for electronic applications, for example in OLED technology: Their high T_g values and their resistance to plasma-induced ablation have allowed us to deposit satisfactory nc-Si:H layers by RF-PECVD, subject to the selection of suitable deposition parameters. The high expansion coefficients of some polymers, particularly of PO, remains an important obstacle opposing fabrication of reliable devices, yet the resilience of nc-Si:H films observed on substrates other than PO is encouraging. Relationships between deposition conditions, structural and transport properties that we have observed manifest much similarity between the behaviors of nc-Si:H films grown on glass and on polymer substrates.

Acknowledgements

This work is supported by grants from the Natural Sciences and Engineering Research Council of Canada (NSERC). The authors are grateful to Drs X.M Zhao and R.A. Shick of Promerus LLC, for providing high-T_g substrate materials (PO, PA, and PS) and for valuable discussions. We also thank the staff at the LMF and LCM laboratories at École Polytechnique and at the Université de Montréal for valuable assistance.

References

- [1] S. Angiolini, M. Avidano, R. Bracco, C. Barlocco, N.D. Young, M. Trainor, X-M. Zhao, *SID Digest*, **2003**, 47.1
- [2] Anon, “see what can be high performance films”; pamphlet published jointly by Ferrania Imaging Technologies, Promerus LLC and Sumitomo Bakelite Co., Ltd.
- [3] Y. Kuo, Editor, *Thin Film Transistors*, Kluwer Academic Publishers, Dordrecht, **2004**.
- [4] A. Marshall and S. Natarajan, Editors, *SOI Design: Analog, Memory and Digital Techniques*, Kluwer Academic Publishers, Dordrecht, **2002**.
- [5] U. Kroll, J. Meier, A. Shah, S. Mikhailov, J. Weber, *J. Appl. Phys.*, **1996**, 80, 4971.
- [6] O. Vetterl, A. Gross, T. Jana, S. Ray, A. Lambertz, R. Carius, F. Finger, *J. Non-Cryst. Sol.*, **2003**, 299-302, 772.
- [7] S. K. Ram, S. Kumar, R. Vanderhagen, P. Roca I Cabarrocas, *J. Non-Cryst. Sol.*, **2002**, 299-302, 411.
- [8] Z. Suo, E.Y. Ma, H. Gleskova, and S. Wagner, *Appl. Phys. Lett.*, **1999**, 74, 1177.
- [9] H. Gleskova, S. Wagner, Z. Suo, *Appl. Phys. Lett.*, 1999, 75, 3011,.
- [10] M. Ohring, *Material Science of Thin Films*, Second Edition, Academic Press, Boca Raton, **2002**.
- [11] E. Bustarret, M. A. Hachicha, M. Brunel, *Appl. Phys. Lett.*, **1988**, 52, 1675.
- [12] G. Yue, J.D. Lorentzen, J. Lin, D. Han, Q. Wang, *Appl. Phys. Lett.*, **1999**, 75, 492.
- [13] C. Droz, E. Vallet-Sauvain, J. Bailat, L. Feitknecht, J. Meier, A. Shah, *Solar Energy Mat. & Solar Cells*, **2004**, 81, 61.
- [14] I.H. Cambell and P.M. Fauchet, *Solid State Commun.*, **1986**, 58, 739.
- [15] D.M. Bhusari, A.S. Kumbhar, S.T. Kshirsagar, *Phys. Rev. B*, **1993**, 47, 6460.
- [16] V. Paillard, P. Puech, P. Roca I Cabarrocas, *J. Non-Cryst. Sol.*, **2002**, 299-302, 280.
- [17] J. Owen, D. Han, B. Yan, J. Yang, K. Lord, S. Guha, *NCPV and Solar Review Meeting*, **2003**, NREL/CD-520-33586, 776.
- [18] F.M. Smits, *Bell System Technical Journal*, **1958**, 37.3.
- [19] D.M. Manos and D.L. Flamm, *Plasma Etching: An Introduction*, Academic Press, Boston, **1988**.
- [20] R. Platz, S. Wagner, *J. Vac. Sci. Technol. A*, **1988**, 16, 3218.
- [21] P. Torres, J. Meier, R. Fluckinger, U. Kroll, J.A. Anna Selvan, H. Keppner, A. Shah, S.D. Littelwood, I.E. Kelly, P. Giannoules, *Appl. Phys. Lett.*, **1996**, 69, 1373.

APPENDIX II. Gene delivery by electroporation after dielectrophoretic positioning of cells in a non-uniform electric field

Citation: MacQueen, L. A., Buschmann, M. D., Wertheimer, M. R. (2008) Gene delivery by electroporation after dielectrophoretic positioning of cells in a non-uniform electric field. *Bioelectrochemistry*. 72: 141–148

Luke A. MacQueen,^a Michael D. Buschmann,^{*b} and Michael R. Wertheimer^a

^a Department of Engineering Physics, Ecole Polytechnique, PO Box 6079 Station Centre-ville, Montreal, Qc H3C 3A7, Canada.

^b Department of Chemical Engineering and Institute of Biomedical Engineering, Ecole Polytechnique

E-mail: michael.buschmann@polymtl.ca; Web site : <http://www.polymtl.ca/tissue/>

Abstract

We report the use of dielectrophoresis (DEP) to position U-937 monocytes within a non-uniform electric field, prior to electroporation (EP) for gene delivery. DEP positioning and EP pulsing were both accomplished using a common set of inert planar electrodes, micro-fabricated on a glass substrate. A single-shell model of the cell's dielectric properties and finite-element modeling of the electric field distribution permitted us to predict the major features of cell positioning. The extent to which electric pulses increased the permeability of the cell-membranes to florescent molecules and to pEGFP-Luc DNA plasmids were found to depend on prior positioning. For a given set of pulse parameters, EP was either irreversible (resulting in cytolysis), reversible (leading to gene delivery), or not detectable, depending on where cells were positioned. Our results clearly demonstrate that position-dependent EP of cells in a non-uniform electric field can be controlled by DEP.

Keywords: Electroporation; electropermeabilization; dielectrophoresis; non-uniform electric field; gene delivery; transfection; microelectrode;

1. Introduction

Biological cells of various types can be distinguished from one-another and displaced within a liquid medium using dielectrophoresis (DEP) [1]. In a spatially non-uniform electric field, \mathbf{E} , the differential electric polarizability of cells and their suspending medium produces the DEP force, which can be either attractive (towards the strong- \mathbf{E} regions) or repulsive (towards the weak- \mathbf{E} regions), depending on experimental conditions. Attractive or repulsive DEP forces are usually referred to as “positive” (pDEP) or “negative” (nDEP), respectively. Measurement of the DEP force as a function of experimental variables produces DEP “spectra” which are characteristic of each cell-type, allowing for cell separation and identification [2, 3]. In microfluidic devices, DEP has been used to transport and position cells with sufficient precision to enable single-cell manipulation [4-6].

Microfluidic devices for single-cell or sub-cellular analysis often use electric field-based techniques other than DEP to increase permeability of the cell membrane [7-9], or to induce cytolysis [10, 11]: Electroporation or electro-permeabilization (EP) results from the application of an intense electric field to bring about structural changes of the cell membrane that increase its permeability. It is well known that irreversible EP leads to cytolysis [12], while reversible EP can be used to transfer molecules such as DNA into the cells while maintaining high rates of cell survival [13]. Generally, pulsed electric fields are used and the extent of EP is determined by parameters such as the strength, duration, and repetition rate of the electric pulses. Critical values of the electric field strength, which determine whether cell-membrane EP is reversible or irreversible, are specific to each cell-type and are usually determined by performing experiments at different \mathbf{E} -values [14, 15].

Traditionally, *in vitro* EP has been accomplished using electrodes with millimeter spacing, and the position of individual cells within the electrode chamber did not need to be considered [16]. In contrast, micro-fabricated devices for EP accommodate relatively small numbers of cells and their smaller (sub-mm) electrode dimensions require consideration of spatial non-uniformities in \mathbf{E} and of cell-positioning with respect to the electrodes [7-11]. Cell-positioning by DEP is known to complement EP experiments. For example, the alignment of cells by DEP after EP has been used for cell-cell fusion [17], and EP of DEP-trapped cells increased the sensitivity of impedance-based cell-detection [18]. In a spatially non-uniform \mathbf{E} , the dependence of EP on the field’s amplitude results in position-dependent EP, and therefore leads to regions within the chamber where either reversible or irreversible EP may prevail [19, 20].

In the present report, we have used spatially non-uniform \mathbf{E} to assess the extent of reversible and irreversible EP as a function of cell position within the electrode chamber. As a first step, position-dependent EP of a single cell-type, U-937 [21], was investigated using fluorescent probes. We selected a single cell-type to ensure that pulsing conditions required for EP were similar for all cells, such that any differences in EP would primarily be due to their positioning. We then used DEP to accentuate position-dependent EP, by moving cells into

specific regions within the electrode chamber. Gene-delivery was accomplished for all cases of cells being randomly distributed, or selectively positioned by DEP prior to EP, however the number of successfully transfected cells and their viability depended on the specific conditions of EP and of DEP.

2. Methodologies

2.1. DEP analyses using a single-shell dielectric model of a spherical cell

Dielectric parameters were determined independently of EP experiments, by fitting the measured cross-over frequency from DEP experiments (defined in Eq 3 below) with a single-shell model of the spherical cell [22, 23]. Different values of the complex electrical permittivity, ε^* , were assigned to the external medium, $\varepsilon_e^* = \varepsilon_e - j\sigma_e/\omega$, to the cell membrane, $\varepsilon_m^* = \varepsilon_m - j\sigma_m/\omega$, and to the (internal) cytosol, $\varepsilon_i^* = \varepsilon_i - j\sigma_i/\omega$, where ε designates permittivity, σ electrical conductivity, and $\omega = 2\pi f$ angular frequency, f being the frequency of the applied sinusoidal electric field, and $j = \sqrt{-1}$. The *relative* permittivity is $\kappa = \varepsilon/\varepsilon_0$, ε_0 being the permittivity of free space.

The DEP phenomena observed in the present work can be modeled using the following four equations (Eqs. 1-4) [25]: The DEP force, F_{DEP} , for the case of a spherical cell of radius, a , is approximated by

$$F_{DEP} = 2\pi\varepsilon_e a^3 \operatorname{Re}[K(\omega)]\nabla E^2, \quad (1)$$

where the polarization factor, K , is

$$K(\omega) = \frac{\varepsilon_{cell}^* - \varepsilon_e^*}{n\varepsilon_{cell}^* + (n+1)\varepsilon_e^*}, \quad (2)$$

where $\varepsilon_{cell}^* = \varepsilon_{cell} - j\sigma_{cell}/\omega$ is the complex electrical permittivity of the cell and n is the multipolar term (for the present spherical case, we assumed a pure dipole, $n = 1$). nDEP and pDEP correspond to $K < 0$ and $K > 0$, respectively. A single “cross-over” frequency, f_0 , defined by $K(f_0) = 0$ and $F_{DEP}(f_0) = 0$, was seen in DEP experiments (described below) when $f < 10^7$ Hz:

$$f_0 = \frac{1}{2\pi} \left(\frac{(\sigma_e - \sigma_{cell})(\sigma_{cell} + 2\sigma_e)}{(\varepsilon_{cell} - \varepsilon_e)(\varepsilon_{cell} + 2\varepsilon_e)} \right)^{\frac{1}{2}} \quad (3)$$

The effective complex permittivity of the cell, ε_{cell}^* , based on the above single-shell theory is

$$\varepsilon_{cell}^* = \varepsilon_m^* \frac{\left(\frac{a}{a-d} \right)^3 + 2 \frac{\varepsilon_i^* - \varepsilon_m^*}{\varepsilon_i^* + 2\varepsilon_m^*}}{\left(\frac{a}{a-d} \right)^3 - \frac{\varepsilon_i^* - \varepsilon_m^*}{\varepsilon_i^* + 2\varepsilon_m^*}}, \quad (4)$$

where d is the membrane's thickness. This model has been used in previous work to measure ε_m^* , ε_i^* and the area-specific conductance of the membrane, $G_m = \sigma_m/d$, for several cell-types, using DEP [2, 3, 22, 23] and the electrorotation technique [24, 26, 27]. In our study we took fixed values for a , d , σ_m , ε_i and ε_e . We assumed $a = 7.5 \mu\text{m}$ (from optical measurements), $d = 7 \text{ nm}$ [27], $\sigma_m = 10^{-6} \text{ S m}^{-1}$, and $\varepsilon_i = \varepsilon_e = 80\varepsilon_0$, as will be further discussed below. The experimental conditions determined f and σ_e , that were in the ranges $10^4 < f \text{ (Hz)} < 10^7$ and $10^{-3} < \sigma_e \text{ (S m}^{-1}\text{)} < 1.6$. The remaining two parameters, ε_m and σ_i , were then found by fitting experimental f_0 data using Eq. 2 ($K(f_0) = 0$), with ε_{cell}^* given by Eq. 4 and restricting the fit parameters to the ranges $0.2 < \sigma_i \text{ (S m}^{-1}\text{)} < 1$; and $3\varepsilon_0 < \varepsilon_m < 23\varepsilon_0$. The differences between measured and calculated values of f_0 were minimized using a least-squares algorithm (lsqcurvefit, Matlab v. 7.2, The Mathworks, Natick, MA).

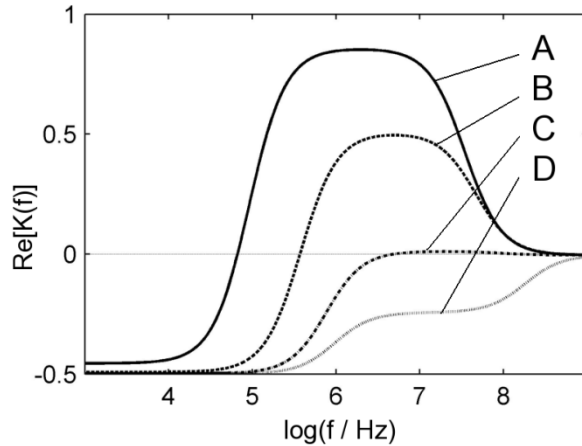


Fig. 1 The real part of the polarization factor, $\text{Re}[K(f)]$, in Eqs 1 and 2 versus frequency, f , for model parameters corresponding to U937 monocytes and at different values of σ_e . A: $\sigma_e = 0.0175 \text{ S m}^{-1}$; B: $\sigma_e = 0.1 \text{ S m}^{-1}$; C: $\sigma_e = 0.4 \text{ S m}^{-1}$; and D: $\sigma_e = 1.0 \text{ S m}^{-1}$.

The polarization factor $K(f, \sigma_e)$ determines cell positioning by DEP, where nDEP occurs when $K(\text{low-}f) < 0$ and pDEP when $K(\text{high-}f) > 0$. Using parameters found from best fits presented below in the results ($\epsilon_m = 6.0\epsilon_0$, $\sigma_i = 0.425 \text{ S m}^{-1}$), the cross-over frequency, f_0 , is seen to increase when σ_e increases (from A to B to C to D in Fig 1). When $\sigma_e \gg \sigma_i$, $K < 0$ for all values of f , and only nDEP can occur (Fig. 1, curves C and D).

2.2. Fabrication of electrodes and modeling of the electric field

Planar Ti/Pt electrodes were fabricated on glass substrates using standard lift-off processes [28]: Chromium masks were fabricated on glass (Bandwidth Foundry, Sydney, NSW, Australia) and photolithography was carried out by spin-coating an adhesion promoter, AP300 (Silicon Resources, Chandler, AZ), a lift-off resist LOR5A (MicroChem, Newton, MA) and a final, positive, resist S1813 (Shipley, now part of Rohm & Haas, Philadelphia, PA). UV exposure was done using a Karl Süss MA-4 mask aligner (Süss Microtec, Waterbury Center, VT). The electrodes were deposited by electron beam evaporation (Ti adhesion layer, 10 nm) and sputtering (Pt layer, 70 nm), the former under ultra-high-vacuum and the latter in Argon at 2.4 Pa. For each glass slide (dimensions: 76.2 x 25.4 x 1.5 mm), the lift-off procedure produced 12 sets of electrodes, each with three leads (Fig. 2a) to which electrical connectors were bonded using a combination of conductive silver epoxy (MG Chemicals, Surrey, BC, Canada) and a standard two-phase epoxy (LePage, Toronto, ON, Canada). The electrodes were placed within

the microscope slide-carrier of an inverted optical microscope (AxioVert S100TV, Carl Zeiss Microimaging, Thornwood, NY) and connected to a signal generator (Model 33220A, Agilent, Palo Alto, CA), which was used to generate both sine waves for DEP and square pulses for EP, without the requirement for any additional signal conditioning or amplification. During DEP manipulations, the central electrode was driven at opposite polarity to the surrounding structure (Fig. 2b, e2 and e1, respectively). The latter possessed periodically-spaced triangular features, which gave rise to alternating regions of strong- and weak- \mathbf{E} (Fig. 2c). The electrode area over which significant DEP occurred (Fig. 2c, outlined trace) was about 3 mm^2 . The distance of closest approach between the inner two electrodes (at the tip of each triangular portion) was $50 \text{ }\mu\text{m}$.

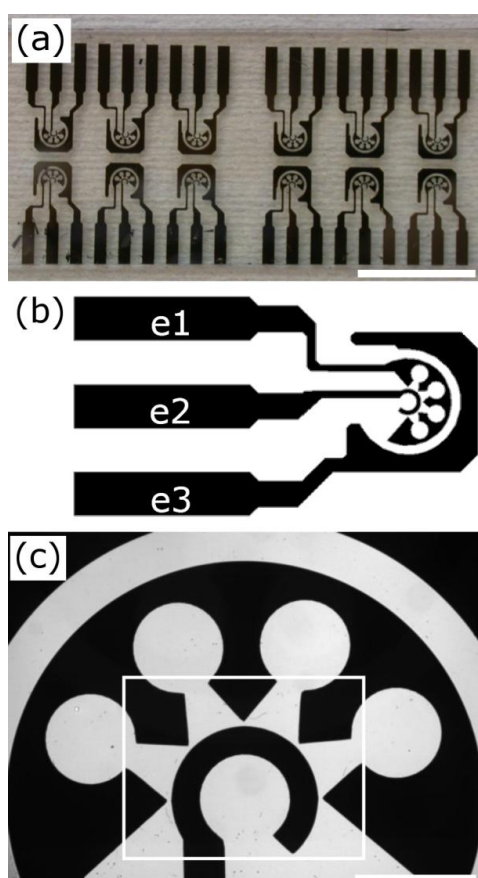


Fig. 2 Ti/Pt electrodes deposited on a glass microscope slide. (a) Twelve sets of 3-lead electrodes. Scale bar is 1.5 cm. (b) One 3-lead electrode set with electrodes labeled e1, e2, and e3. The inner two electrodes, e1 and e2, are driven at opposite polarity, while the outermost electrode, e3, is grounded. (c) Magnified view of the inner two electrodes, e1 and e2. The rectangular trace represents the region used for DEP: Strong- and weak- \mathbf{E} regions occur where e1 approaches and recedes from e2, respectively. Scale bar is 1 mm.

We defined positions within 50 μm of the electrode edges as strong-**E** regions, and otherwise as weak-**E**. The values of **E** averaged over the strong and weak regions differed by a factor of approximately three. For example, when the applied voltage was $U = 10\text{ V}$, the maximum value of $E = U/l$, where l is the inter-electrode distance, was 200 kV m^{-1} . The **E** values averaged over the strong- and weak- **E** regions were $\sim 180\text{ kV m}^{-1}$ and $\sim 60\text{ kV m}^{-1}$, respectively. These estimates of **E** were accomplished with Comsol Multiphysics v3.2 software (Comsol, Stockholm, Sweden) using the conductive media mode with the electric potential assigned at boundaries (Dirichlet-type of boundary conditions), and assuming a homogeneous medium in which the presence of cells was neglected.

2.3. Cells and media

An established human monocytic cell-line, U-937, obtained from ATCC (Manassas, VA), was chosen for these experiments, primarily because these cells are cultured in suspension and tend not to adhere either to solid surfaces or to one-another. The cells were cultured in RPMI 1640 (Sigma-Aldrich, St. Louis, MO) supplemented with 10% FBS (Atlanta Biologicals, Laurenceville, GA), and incubated at $37\text{ }^{\circ}\text{C}$ in an atmosphere supplemented with 5% CO_2 . Prior to EP and DEP experiments, the cells were centrifuged at 190g for five minutes (Model CR4 22, Jouan, Saint-Herblain, France) and re-suspended in one of several low-conductivity buffers. Buffers of different conductivity were made by diluting phosphate-buffered saline (PBS D1283: 136.8 mM NaCl, 8.1 mM Na_2HPO_4 , 2.7 mM KCl, 1.5 mM KH_2PO_4 , Sigma) in de-ionized water ($\text{DI-H}_2\text{O}$), and adding D-glucose (Sigma) to maintain the osmolality at $200 \pm 25\text{ mOsm kg}^{-1}$ (close to the isotonic value of $\sim 285\text{ mOsm kg}^{-1}$). A slightly hypotonic buffer was used to induce a slight swelling of the cells that is advantageous for EP experiments since the amplitude and numbers of pulses could be reduced compared to the isotonic case [29, 30]. The cell radius (and standard deviation) was estimated at $a = 7.5 \pm 1.0\text{ }\mu\text{m}$, on using the straight-line measurement feature of imaging software (Northern Eclipse v. 7.0, Empix Imaging, Mississauga, ON, Canada). In comparison, the isotonic value was $a = 6.25 \pm 1.0\text{ }\mu\text{m}$. This level of hypotonicity was considered acceptable with reference to the relatively large range of osmolalities $75 < \text{Osmolality (mOsm kg}^{-1}) < 300$ used in previous EP-based experiments [29, 30]. The pH was always above 6.0 ± 0.5 , and was also safe for short-term use, cells being kept within the buffer solution for less than 15 minutes. The conductivity range of the diluted PBS buffers was $10^{-3} < \sigma_e\text{ (S m}^{-1}) < 1.6$, and the maximum concentration of D-glucose required, corresponding to the medium with lowest σ_e , was 220 mM. Conductivity and pH were measured using an Accumet model 20 instrument (Fisher Scientific, Hampton, NH), and osmolality was measured using a model 3D3 osmometer, based on freezing-point depression (Advanced Instruments, Norwood, MA).

2.4. Cell positioning and measurement of the cross-over frequency

Unless otherwise stated, cells were suspended in buffer at a density of $\sim 5 \times 10^5$ cells mL⁻¹, as measured by hemocytometer (VWR Scientific, Mississauga ON), and were transferred in 7.5 μ L volumes to the electrode surface using a micropipette. This produced a ~ 250 μ m deep liquid layer containing ~ 3750 cells, which covered an area of ~ 30 mm². The DEP signal applied to the electrodes was a sine wave with a peak voltage of $U = 3$ V, and a frequency sweep $10^4 < f$ (Hz) $< 10^7$ was performed for each value of σ_e . Cell behavior was monitored visually or with a CCD camera (Model QIC-F-/M2: QImaging, Burnaby, BC, Canada), and still images were captured for subsequent analysis. Under these conditions, the majority of cells attained equilibrium positions along the plane of the electrodes after about five minutes, by a combination of DEP and sedimentation, at which point the experiment was stopped. Cell-positioning statistics were then compiled from the image by counting the cells that had migrated to strong-**E** regions (where the distance between cells and electrode edges was < 50 μ m), versus weak-**E** regions (where the distance between cells and electrode edges was > 50 μ m).

Under certain conditions with appropriate choices of f and σ_e , F_{DEP} was found to be negligible, and cells remained randomly distributed over the electrode surfaces. As described above, the corresponding f values are the “cross-over” frequencies, f_0 , and a different value of f_0 was found for each value of σ_e . To determine f_0 , we repeated the positioning experiments at different f values, until random distributions of cells were observed, approaching f_0 from frequencies both above and below f_0 in order to minimize error. This procedure was repeated three times for each σ_e .

2.5. Electroporation and gene-delivery

We used square-wave bipolar electric pulses for electroporation. For each experimental condition, a sequence of six pulses was applied, each with width $t_e = 20$ μ s, rise- and fall times of $t_s = 5$ ns, and inter-pulse intervals $t_r = 0.5$ s (that is, repetition rate, $rr = 2$ Hz). Peak applied voltages were $U = 7, 8, 9,$ and 10 V. First, randomly-distributed cells were electroporated in the presence of fluorescent probes, to visualize the spatial dependence of EP in the case of a non-uniform electric field. Cell-positioning by DEP was used to accentuate this position-dependence of EP and further influence gene-transfer. Expression of the transferred genes and cell viability (cell-survival) were quantified by determining the ratios N_T/N_{TOT} and N_S/N_{TOT} , N_T being the number of transfected cells, N_S the number of surviving cells, and N_{TOT} the total number of cells.

We used a “Live(green)/Dead(red)” cytotoxicity kit (Invitrogen, Carlsbad, CA) to visualize the position-dependence of EP. The protocol consists of adding a mixture of two different fluorescent indicators, each at 1 μ M concentration, to the cell suspension. The first indicator, Calcein AM, can enter through the cell membrane and then be cleaved by esterases in healthy cells to become fluorescent (green). The second indicator, Ethidium HD-1, is excluded

from healthy cells with intact cell membranes, but traverses those that have been compromised; once inside the nucleus, it binds to nucleic acids, which greatly ($40 \times$) increases its fluorescence (red). Thus, healthy cells appear green, irreversibly damaged cells red, and reversibly electroporated cells appear orange due to the combined presence of both indicators. Live/Dead EP results were obtained using a random and uniform distribution of cells to assess position dependence of EP due to the spatially varying E .

For gene-transfer we used a DNA plasmid expressing a fluorescent reporter, pEGFP_{Luc} (Clontech, Mountain View CA), at a concentration of $0.55 \mu\text{g mL}^{-1}$. As above, $7.5 \mu\text{L}$ of buffer containing cells and DNA were placed over the electrodes at a cell density of $D = 5 \times 10^5 \text{ cells mL}^{-1}$ (total number of cells ~ 3750). The buffer was PBS diluted in DI- H_2O , with conductivity $\sigma_e = 50 \text{ mS m}^{-1}$, and osmolality $= 200 \pm 25 \text{ mOsm kg}^{-1}$. Transfection experiments were performed at room temperature ($27 \text{ }^\circ\text{C}$, or 300 K) under four sets of conditions: (i) EP pulses were applied after the cells had been positioned by pDEP for five minutes, using a 3 V , 1 MHz sinusoidal potential; (ii) EP pulses were applied after five minutes of nDEP positioning, using a 3 V , 40 kHz sinusoidal potential; (iii) EP pulses were applied after five minutes of sedimentation only (“no DEP”); and (iv) as a control with neither DEP nor EP pulses. Each condition (i) to (iv) was repeated four times. Following gene transfer, cells were incubated in FBS-supplemented RPMI growth medium at $37 \text{ }^\circ\text{C}$ with $5\% \text{ CO}_2$. The number of transfected cells, N_T , and surviving cells, N_S , were monitored by fluorescence microscopy.

3. Results

3.1. Cell Positioning

The measured DEP spectra of cells reveal the ranges of f and σ_e for which both pDEP and nDEP positioning were achieved (Figs. 3b and 3c, respectively). The data can be represented by the crossover frequencies (Fig. 4), where a linear relationship between f_0 and σ_e was observed for $0.02 < \sigma_e \text{ (S m}^{-1}\text{)} < 0.2$. When σ_e was close to physiological (1.5 S m^{-1}), only nDEP was observed within the frequency range investigated, the onset of pDEP occurring only when $\sigma_e < 0.4 \text{ S m}^{-1}$. The intercept of f_0 data extrapolated towards $\sigma_e = 0$ (the origin in Fig. 4) was close enough to zero that an upper limit of $\sigma_m < 10^{-5} \text{ S m}^{-1}$ ($G_m < 1430 \text{ S m}^{-2}$) could be determined. These small values of σ_m have a negligible effect when calculating K , for $\sigma_e > 5 \times 10^{-2} \text{ S m}^{-1}$ so that we assumed $\sigma_m = 10^{-6} \text{ S m}^{-1}$ for further calculations and for model fitting.

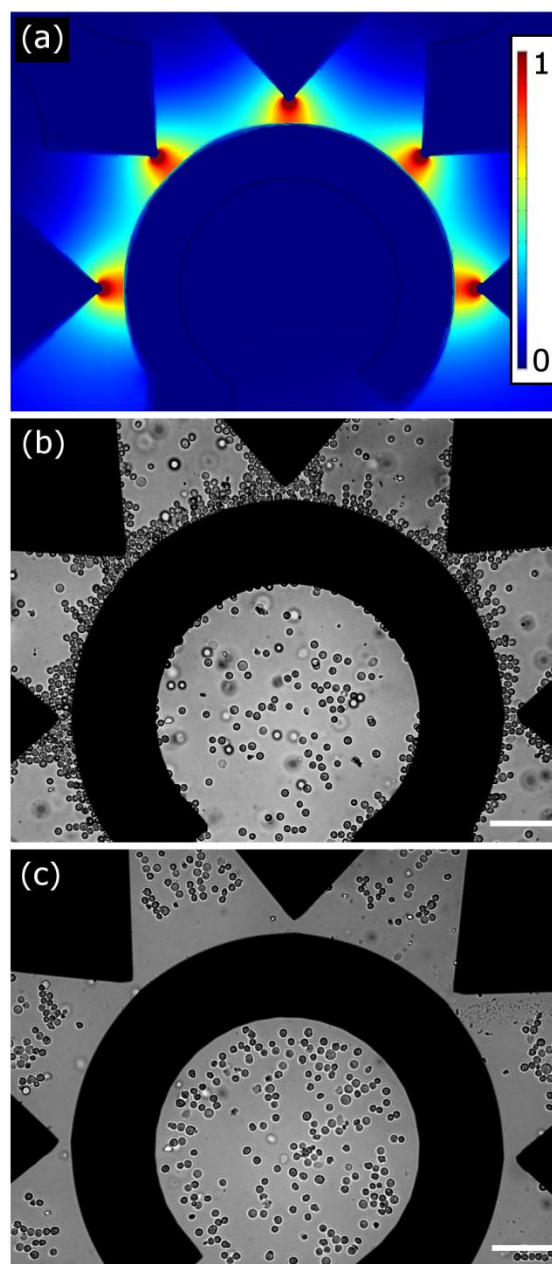


Fig. 3 Positioning of U-937 monocytes by DEP. (a) Simulated electric field distribution using an arbitrary linear scale. (b) Cells positioned in the strong- E regions by pDEP. (c) Cells positioned in the weak- E regions by nDEP. Scale bars are 300 μm .

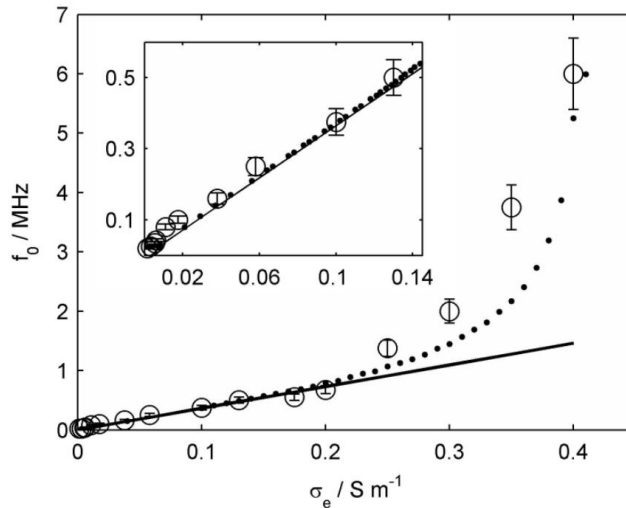


Fig. 4 The crossover frequency, f_0 , versus conductivity of the extracellular medium, σ_e , for U-937 monocytes. Open circles are experimental f_0 (mean \pm SD, $n = 3$), while the dotted line is a fit using Eqs 2 and 4, and the solid line is a fit using Eq 3. The insert shows the region of low σ_e .

We fit f_0 data to both Eq. 2 (with the condition $K(f_0) = 0$) and Eq. 3 (valid for $\sigma_e < \sim 0.2 \text{ S m}^{-1}$, see Fig. 4) by varying ϵ_m and σ_i , with other parameters fixed at $a = 7.5 \text{ }\mu\text{m}$, $d = 7.0 \text{ nm}$, $\sigma_m = 10^{-6} \text{ S m}^{-1}$ and $\epsilon_i = \epsilon_e = 80\epsilon_0$. The best fit for both equations was found when $\epsilon_m = 6.0\epsilon_0$ ($C_m = 7.6 \text{ mF m}^{-2}$) and $\sigma_i = 0.425 \text{ S m}^{-1}$. These data therefore provide estimates for the dielectric properties of U-937 monocytes as $\sigma_m < 10^{-5} \text{ S m}^{-1}$ ($G_m < 1430 \text{ S m}^{-2}$), $\epsilon_m = 6.0\epsilon_0$ ($C_m = 7.6 \pm 1.25 \text{ mF m}^{-2}$), $\sigma_i = 0.425 \text{ S m}^{-1}$, and $\epsilon_i = 80\epsilon_0$, and can be used to predict DEP responses under arbitrary conditions of f and σ_e .

3.2. Live/Dead viability tests

During DEP experiments with $U < 4 \text{ V}$, Live/Dead tests revealed that the U-937 cells remained viable for at least 15 minutes, independent of f and σ_e values. Thus an amplitude of $U = 3 \text{ V}$ was used for subsequent DEP positioning prior to EP.

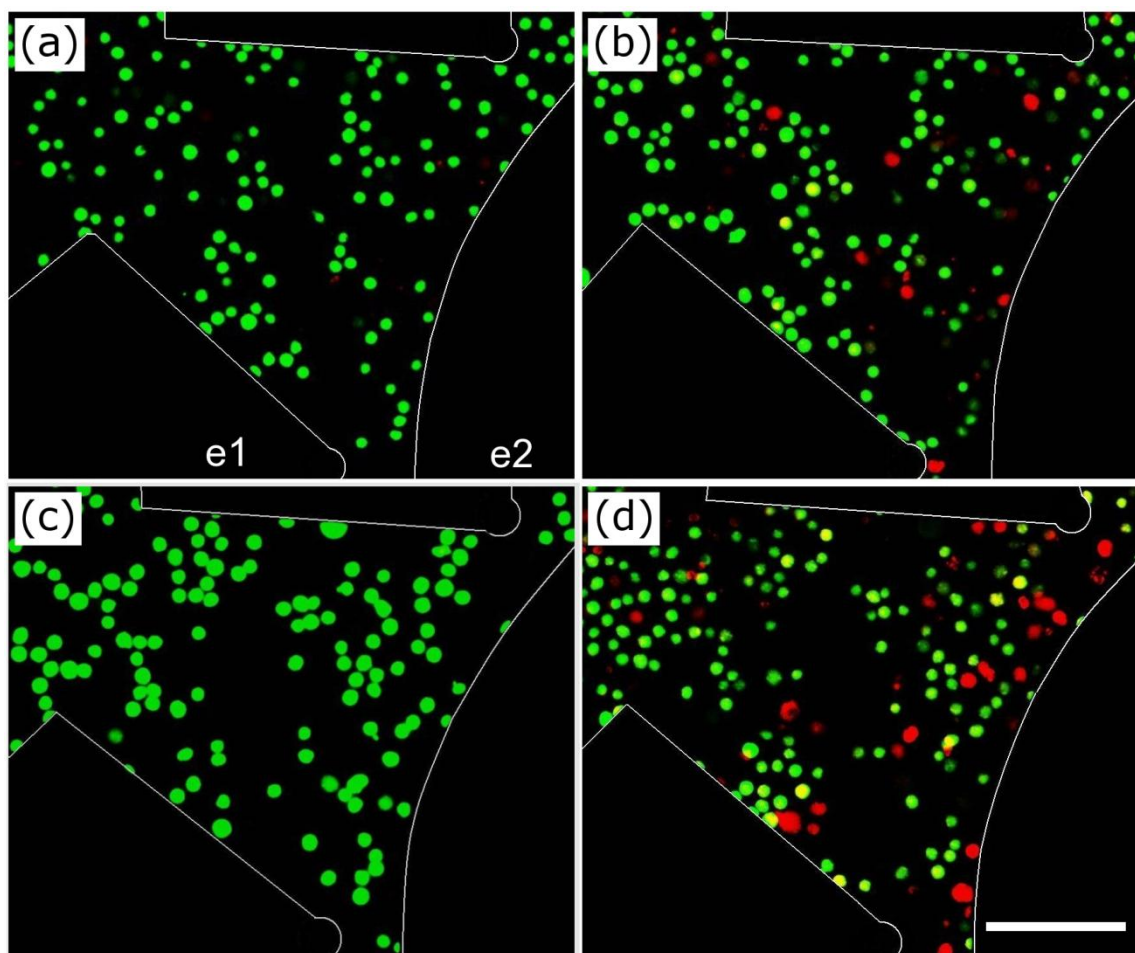


Fig. 5 Position-dependent EP of U-937 monocytes, as monitored by “Live(green)/Dead(red)” fluorescence tests. (a) Live cells, shown before pulsing. (b) The same cells shown in (a), but five minutes after applying pulses of amplitude $U = 8$ V, showing limited cell death. (c) Live cells shown before pulsing. (d) The same cells shown in (c), but five minutes after applying pulses of amplitude $U = 10$ V, showing more extensive cell death near the pDEP region. Electrode (e1, e2) edges are outlined for clarity. Scale bar is $100 \mu\text{m}$.

The application of higher voltage ($7 \text{ V} < U < 10 \text{ V}$), short-duration ($t_e < 100 \mu\text{s}$) pulses demonstrated position-dependent EP within the region of spatially non-uniform electric field. Although cells displayed some heterogeneous behaviour (some cells in the strong- \mathbf{E} regions remained green, while others in weak- \mathbf{E} regions became red), a clear position-dependent response to EP could be observed (Fig. 5), consistent with the calculated distribution of \mathbf{E} (Fig. 6). For the case of low pulse amplitudes ($U < 4 \text{ V}$), few green-to-red transitions occurred (less than 3% of cells), but as U was increased the regions containing red cells expanded from the tips of the “e1” electrodes to eventually fill in the space between electrodes e1 and e2 when $U > 8 \text{ V}$ (Fig. 5d and 6c). Therefore, the “critical” field values for reversible and irreversible EP could be estimated

from calculated field values and these cell distributions as $E = 40 \text{ kV m}^{-1}$ and $E = 120 \text{ kV m}^{-1}$, respectively. For example, when $U = 10 \text{ V}$, the region of irreversible EP coincided with that in which pDEP was observed in the course of cell-positioning experiments (Fig. 3b), while reversible EP was observed in the nDEP region (Fig. 3c).

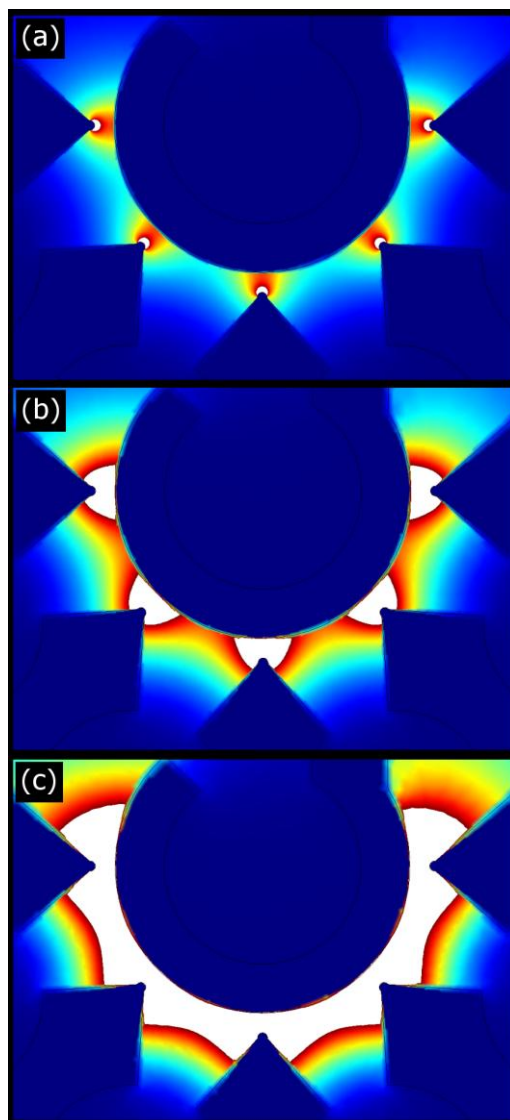


Fig. 6 Calculated position-dependence of EP of U-937 monocytes, for different values of U . White = irreversible EP (cytolysis), Red-Green = reversible EP, Blue = no EP. (a) $U = 6 \text{ V}$, (b) $U = 8 \text{ V}$, (c) $U = 10 \text{ V}$.

3.3. Gene-delivery

Cell positioning by DEP prior to EP significantly influences transfection efficiency and cell viability, compared with randomly-distributed cells (“no DEP”) under otherwise identical pulsing conditions (Fig. 7). For EP amplitudes of $U = 7$ or 8 V, viability was generally high, while higher EP amplitudes reduced viability (Fig. 7b). A coupling between DEP and EP was evident, where the number of transfected cells increased with U initially for all three cases (nDEP, no DEP, pDEP) (Fig. 7a), but then decreased above $U = 8$ V, initially for pDEP and then for “no DEP”. Cell viability decreased monotonically as EP amplitude U increased. Transfected cells that survived the first 24 hours after EP remained viable and were observed to proliferate for the duration of our observations (one week). For the control group (no DEP, no pulses) we found $N_T = 0$, as expected.

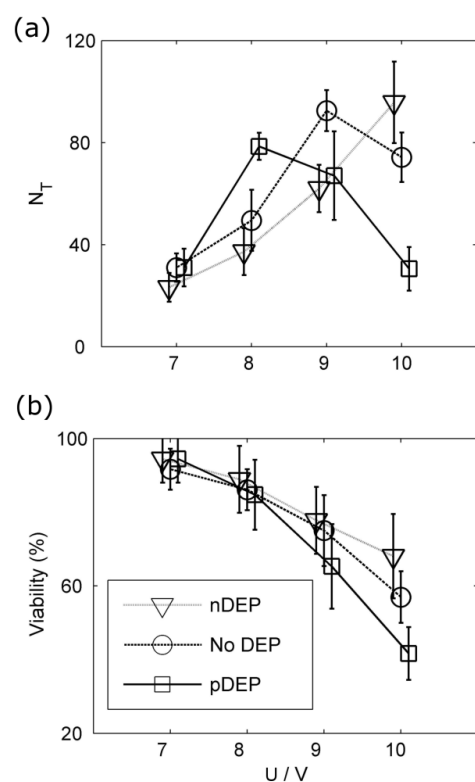


Fig. 7 Position-dependent gene transfection level and viability of U937 monocytes. (a) Number of transfected cells, N_T , and (b) viability vs. pulse amplitude, U , for cells positioned by either pDEP (squares), nDEP (triangles), or with “no DEP” (no induced positioning, circles) prior to pulsing. Mean \pm SD ($n=4$) values are shown, and data were shifted slightly to increase clarity between groups.

It is important to note that a sizeable fraction of cells remained outside the DEP/EP-affected regions (identified in Fig. 2c), and that these cells were later counted when compiling transfection data (Fig. 7). This was the result of the necessarily quite large (7.5 μL) volumes of cell suspension applied, and led to a relatively high background of viable but non-transfectable cells that were estimated to be $\sim 30\%$ of the total cell number.

4. Discussion

4.1. Dielectrophoresis and Electroporation

The major features of DEP positioning were adequately predicted using a single-shell theory, with static dielectric properties of the membrane, (ϵ_m, σ_m) , cytosol, (ϵ_i, σ_i) , and media (ϵ_e, σ_e) . Best fit values of $\epsilon_m = 6.0\epsilon_0$ ($C_m = 7.6 \pm 1.25 \text{ mF m}^{-2}$), $\sigma_m < 10^{-5} \text{ S m}^{-1}$ ($G_m < 1430 \text{ S m}^{-2}$), and $\sigma_i = 0.425 \text{ S m}^{-1}$, with ϵ_i taken as $80\epsilon_0$, are comparable to previously published parameters for U937 monocytes [3], particularly when the low osmolarity is taken into account [29]. The measurements of f_0 allowed optimization of experimental parameters (ranges of f and σ_e values), in order to examine the influence of cell positioning by DEP on cell transfection.

We found that the spatial non-uniformity of \mathbf{E} used during DEP produced a position-dependent EP. Comparing cell positioning by DEP (Fig. 3) with the position-dependence of EP for randomly distributed cells (Fig. 5) reveals how pDEP and nDEP, increased and decreased, respectively, the EP and number of transfected cells. For a given value of U , the field acting on cells in the strong- \mathbf{E} region (corresponding to pDEP) was, on average, three times higher than in the weak- \mathbf{E} region (corresponding to nDEP). Thus, for example, when $U = 8 \text{ V}$, the average \mathbf{E} in the nDEP region was too low for significant EP, in contrast to the pDEP region. In the case of still higher U ($U > 8 \text{ V}$), lysis of cells frequently occurred in the pDEP region, resulting in low viability and low N_T (Fig. 7) while nDEP positioned cells retained better viability and increased transfection efficiency.

The occurrence of “optimal” \mathbf{E} values, the range below which transfection is low and above which viability drops, is well known in the literature [14, 15]. Generally, when \mathbf{E} is spatially uniform, experiments designed to correlate EP with field strength are repeated at different U values. The present spatially non-uniform field offers an advantage that for a given U and set of pulse conditions (fixed values of t_e , t_r , and t_s), EP can be visualised for a range of \mathbf{E} in a single experiment. For the present conditions and cell-type, we estimated “critical” field strengths

of $E = 40 \text{ kV m}^{-1}$ for reversible EP, and $E = 120 \text{ kV m}^{-1}$ for irreversible EP. Therefore, reversible EP leading to the possible uptake of dyes and genes was observed to occur in the range $40 < E \text{ (kV m}^{-1}) < 120$. Since the regions within the electrode chamber where these conditions existed could be calculated from U , we were able to predict the extent of EP based on the combined effect of DEP cell-positioning and the EP pulse amplitude U .

4.2. Limitations

Commercial electroporators are capable of transfecting various cell-types (including U-937) with a higher efficiency than that reported here. This is in part due to the fact that the device presented here allows ~30% of cells to remain in low- E regions, and they were therefore not transfected. Additionally, we did not optimize the cell transfection medium with special reagents that are used in commercial systems. Another limitation related to prediction of gene transfer is the use of the Live/Dead viability tests with dyes that are ~4200 times smaller (by molecular weight) than the DNA plasmid.

5. Conclusions

Several new micro-devices for the manipulation of biological cells have been reported in the literature. Dielectrophoresis (DEP) and electroporation (EP) enable diverse manipulations such as physical displacement (transport and trapping of cells), and gene delivery. The present simple planar micro-electrode device demonstrated that applying both DEP and EP in a spatially non-uniform electric field, permitted correlation of EP with electric field strength. Regions within the electrode chamber where reversible or irreversible EP occurred could then be predicted by the choice of EP pulse height U and DEP positioning allowed additional control over the outcome of EP. This study shows that future devices may combine DEP and EP using spatially non-uniform fields to achieve different objectives in cell movement and manipulation.

Acknowledgements

This work was supported by the Natural Sciences and Engineering Research Council of Canada (NSERC), and by the Canadian Institutes of Health Research (CIHR). The authors thank Yves Drolet for his technical assistance, and Drs. Stéphane Methot and Marc Lavertu for providing the pEGFP plasmids. We also thank the staff of the Micro-fabrication Laboratories (LMF) for their help and expertise, in particular Dr. Souleymane Bah for his assistance with photolithography and fabrication of electrodes.

References

- [1] H. A. Pohl, *Dielectrophoresis*, Cambridge University Press, Cambridge, UK, 1978.
- [2] F. F. Becker, X-B. Wang, Y. Huang, R. Pethig, J. Vykoukal, P. R. C. Gascoyne, Separation of human breast cancer cells from blood by differential dielectric affinity, *Proc. Natl. Acad. Sci. USA* 92 (1995) 860-864.
- [3] Y. Huang, S. Joo, M. Duhon, M. Heller, B. Wallace, X. Xu, Dielectrophoretic cell separation and gene expression profiling on microelectronic chip arrays, *Anal. Chem.* 74 (2002) 3362-3371.
- [4] J. Suehiro, R. Pethig, The dielectrophoretic movement and positioning of a biological cell using a three-dimensional grid electrode system, *J. Phys. D: Appl. Phys.* 31 (1998) 3298-3305.
- [5] T. Müller, G. Gradl, S. Howitz, S. Shirley, Th. Schnelle, G. Fuhr, A 3-D microelectrode system for handling and caging single cells and particles, *Biosens. Bioelec.* 14 (1999) 247-256.
- [6] A. Rosenthal, B. M. Taff, J. Voldman, Quantitative modeling of dielectrophoretic traps, *Lab. Chip* 6 (2006) 508-515.
- [7] J. A. Lundqvist, F. Sahlin, M. A. Aberg, A. Stromberg, P. S. Eriksson, O. Orwar, Altering the biochemical state of individual cultured cells and organelles with ultramicroelectrodes. *Proc. Natl. Acad. Sci. USA* 95 (1998) 10356-10360.
- [8] M. Khine, A. Lau, C. Ionescu-Zanetti, J. Seo, L. P. Lee, A single cell electroporation chip, *Lab. Chip* 5 (2005) 38-43.
- [9] M. B. Fox, D. C. Esveld, A. Valero, R. Lutge, H. C. Mastwijk, P. V. Bartels, A. van den Berg, R. M. Boom, Electroporation of cells in microfluidic devices: a review, *Anal. Bioanal. Chem.* 385 (2006) 474-485.
- [10] S-W Lee, Y-C Tai, A micro cell lysis device, *Sens. Actuators A : Physical* 73 (1999) 74-79.
- [11] M. A. McClain, C. T. Culbertson, S. C. Jacobson, N. L. Allbritton, C. E. Sims, J. M. Ramsey, Microfluidic devices for the high-throughput chemical analysis of cells, *Anal. Chem.* 75 (2003) 5646-5655.
- [12] A. J. H. Sale, W. A. Hamilton, Effects of high electric fields on microorganisms, *Biochem. Biophys. Acta* 148/3 (1967) 781-788.
- [13] E. Neumann, M. Schaefer-Ridder, Y. Wang, P. H. Hofschneider, Gene transfer into mouse lyoma cells by electroporation in high electric fields, *EMBO* 1 (1982) 841-845.
- [14] E. Neumann, The relaxation hysteresis of membrane electroporation, in *Electroporation and Electrofusion in Cell Biology*, A. E. Sowers, and C. A. Jordan (Eds.), Plenum Press, New York, 1989.
- [15] T. Kotnik, L. M. Mir, K. Flisar, M. Puc, D. Miklavčič, Cell membrane electropermeabilization by symmetrical bipolar rectangular pulses: Part 1. Increased efficiency of permeabilization, *Bioelectrochemistry* 54 (2001) 83-90.
- [16] M. Puc, S. Čorović, K. Flisar, M. Petkovšek, J. Nastran, D. Miklavčič, Techniques of signal generation required for electropermeabilization. Survey of electropermeabilization devices, *Bioelectrochemistry* 64 (2004) 113-124.
- [17] U. Zimmermann, Electric field-mediated fusion and related electrical phenomena, *Biochem. Biophys. Acta* 694/3 (1982) 227-277.
- [18] J. Suehiro, T. Hatano, M. Shutou, M. Hara, Improvement of electric pulse shape for electropermeabilization-assisted dielectrophoretic impedance measurement for high sensitive bacteria detection, *Sens. Actuators B: Chemical* 109 (2005) 209-215.

- [19] T. Heida, J. B. M. Wagenaar, W. L. C. Rutten, E. Marani, Investigating membrane breakdown of neuronal cells exposed to nonuniform electric fields by finite-element modeling and experiments, *IEEE Trans. Biomed. Eng.* 49 (2002) 1195-1203.
- [20] T. R. Gowrishankar, D. A. Stewart, J. C. Weaver, Model of a confined spherical cell in uniform and heterogeneous applied electric fields, *Bioelectrochemistry* 68 (2006) 181-190.
- [21] C. Sundstrom, K. Nilsson, Establishment and characterization of a human histiocytic lymphoma cell line (U-937), *Int. J. Cancer* 17 (1976) 565-577.
- [22] P. Gascoyne, R. Pethig, J. Satayavivad, F. F. Becker, M. Ruchirawat, Dielectrophoretic detection of changes in erythrocyte membranes following malarial infection, *Biochim. Biophys. Acta* 1323 (1997) 240-252.
- [23] F. H. Labeed, H. M. Coley, H. Thomas, M. P. Hughes, Assessment of multidrug resistance reversal using dielectrophoresis and flow cytometry, *Biophys. J.* 85 (2003) 2028-2034.
- [24] X. Hu, W. M. Arnold, U. Zimmermann, Alterations in the electrical properties of T and B lymphocyte membranes induced by mitogenic stimulation. Activation monitored by electro-rotation of single cells, *Biochim. Biophys. Acta* 1021 (1990) 191-200.
- [25] T. B. Jones, *Electromechanics of particles*, Cambridge University Press, Vol. 1, 1995, Eq. 3.4, p. 39.
- [26] J. Yang, Y. Huang, X. Wang, X-B. Wang, F. F. Becker, P. R. C. Gascoyne, Dielectric properties of human leukocyte subpopulations determined by electrorotation as a cell separation criterion, *Biophys. J.* 76 (1999) 3307-3314.
- [27] E. G. Cen, C. Dalton, Y. Li, S. Adamia, L. M. Pilarski, K. V. I. S. Kaler, A combined dielectrophoresis, traveling wave dielectrophoresis and electrorotation microchip for the manipulation and characterization of human malignant cells, *J. Microbiol. Meth.* 58 (2004) 387-401.
- [28] M. Madou, *Fundamentals of Microfabrication*, CRC-Press, Boca Raton, FL, 1998.
- [29] V. L. Sukhorukov, W. M. Arnold, U. Zimmermann, Hypotonically induced changes in the plasma membrane of cultured mammalian cells, *J. Membrane Biol.* 132 (1993) 27-40.
- [30] U. Zimmermann, The effect of high intensity electric field pulses on eukaryotic cell membranes: Fundamentals and applications, in *Electromanipulation of Cells*, U. Zimmermann, and G. A. Neil (Eds.), CRC Press, Boca Raton, Florida, 1996.

APPENDIX III. Mechanical properties of mammalian cells in suspension measured by electro-deformation

Citation: MacQueen, L. A., Buschmann, M. D., Wertheimer, M. R. (2010) Mechanical properties of mammalian cells in suspension measured by electro-deformation. *Journal of Micromechanics and Microengineering*. 20: 065007

Luke A MacQueen,¹ Michael D Buschmann,² and Michael R Wertheimer¹

Departments of ¹Engineering Physics, and ²Chemical Engineering and Institute of Biomedical Engineering, Ecole Polytechnique de Montreal, PO Box 6079 Station Centre-ville, Montreal, QC H3C 3A7, Canada. E-mail: michael.buschmann@polymtl.ca

Running head: Electro-deformation of mammalian cells

Abstract

We describe a planar, micro-fabricated device for generating fringing non-uniform electric fields. We used it to measure mechanical properties of individual mammalian cells in suspension by deforming them in time-varying, non-uniform electric fields. Electrical stresses generated by the planar microelectrodes were used to trap and stretch cells, while cell deformation was observed using optical microscopy. Two distinct cell-types were compared after fitting strain data with a three-parameter “standard linear solid” (SLS) model of visco-elasticity, and with a two-parameter power-law (PL) method. Chinese hamster ovary (CHO) cells were approximately twice as stiff as U937 human promonocytes, and CHO cells displayed an elastic behaviour with recovery of initial shape, while U937 strain data bore witness to plastic deformation. Our results demonstrate that electrical stresses generated by micro-fabricated electrodes permit mechanical characterization of distinct mammalian cell-types.

Keywords: biological cell, mechanics, viscoelasticity, dielectrophoresis, electro-deformation, microfabrication

List of symbols

U	electric potential	V
E	electric field strength	$V \cdot m^{-1}$
ϵ_c	dielectric permittivity of a cell	$F \cdot m^{-1}$
ϵ_m	dielectric permittivity of suspension media	$F \cdot m^{-1}$
κ	electric conductivity	$S \cdot m^{-1}$
f	frequency	Hz
ω	angular frequency	$rad \cdot s^{-1}$
σ_u	free surface charge density	$C \cdot m^{-2}$
K	Clausius-Mosotti factor	dimensionless
F	force	N
r_c	cell radius	m
L	length	m
L_x	length of ellipsoid major-axis	m
L_y	length of ellipsoid minor-axis	m
L_0	initial length	m
γ	strain	dimensionless
γ_x	strain of ellipsoid major-axis	dimensionless
γ_y	strain of ellipsoid minor-axis	dimensionless
ν	Poisson's ratio	dimensionless
σ	stress	Pa
J	material compliance	Pa^{-1}
C	cell compliance factor	$m^2 \cdot V^{-2}$
k	elastic constant	Pa
E_0	initial elastic modulus	Pa
E_R	relaxed elastic modulus	Pa
G_0	initial shear modulus	Pa
G_R	relaxed shear modulus	Pa
η	viscosity	$Pa \cdot s$
τ	time constant (or "relaxation time")	s
α	power-law exponent	dimensionless
A	power-law prefactor	$Pa^{-1} \cdot s^{-\alpha}$

1. Introduction

The mechanical properties of mammalian cells in suspension are important determinants of biological functionality in several *in vivo* and *ex vivo* contexts. Cells of the circulatory system, for example, have been extensively studied from a mechanical perspective, and increased stiffness of diseased erythrocytes and leukocytes is known to restrict their flow through small channels such as capillaries (1, 2). Recently, some chemotherapy treatments were shown to increase the stiffness of both lymphoid and myeloid leukemia cells (3). Measurements of cell-stiffness have therefore been essential for determining the biomechanical effects of various drugs and treatments relevant to cells in circulation (4, 5).

Mammalian cells are increasingly being used for the production of recombinant proteins and related products in large-scale bioreactors (6, 7). Suspension culture permits mammalian cells to grow in bioreactors by methods similar to those used in microbial systems that enable scale-up (6). The range of available culture conditions is, however, limited by shear and extensional forces, which are present in several types of bioreactors (8-11). To reduce the harmful effects of mechanical stresses, shear-stress modifiers are often added to cell suspensions (12), although some of these additives can enter through the cell-membrane, with unknown consequences to the health and function of the cultured cells (13). Methods to quantify mechanical properties of suspended cells can therefore be used to improve the design of new cell-types, bioreactors, and micro-fluidic devices by predicting the cellular elastic and visco-elastic responses to various forces.

Unlike adherent cells, which remain fixed during the timescales of most mechanical measurement protocols, suspended cells must be stably positioned within a measurement device. Although the requirement for cell-positioning complicates measurements in some cases, suspended cells have nevertheless been mechanically characterized using a variety of techniques: These include optical traps (OT) (14-18), micropipette aspiration (MPA) (19-23), atomic force microscopy (AFM) (3, 24), and electro-deformation (ED) (25-28). Surprisingly, the most recent review articles that describe methods for mechanical characterization of individual cells did not discuss ED (18, 29), in spite of several important advantages of this technique mentioned in the Discussion section below. Furthermore, erythrocytes appear to be the only cell-type for which multiple independent ED measurements have been reported to date (25, 27, 30, 31) and thus ED appears to be underutilized. The vast majority of mammalian cell-types have not been studied using the ED method.

It is well-known that cells in suspension can be trapped in a non-uniform electric field, E , by dielectrophoresis (DEP) (32, 33), and increased strength of E can result in cell-deformation (25, 34). Although ED has not been widely reported compared with other techniques, recent advances in micro-fabrication have resulted in increased use of electric fields to manipulate cells (35-37), and ED of protoplasts in a micro-fabricated device has been demonstrated (38). We hypothesized that new micro-fabricated electrode geometries could be used to produce electrical forces of sufficient magnitude to trap and deform several types of mammalian cells, which have not yet been characterized mechanically. Our objective was therefore to use ED for mechanical characterization of individual mammalian cells. To accomplish this goal we designed a new microelectrode geometry, which permits the capture and deformation of individual cells in suspension by DEP and ED, respectively. We used ED to measure strain and relaxation of two distinct cell-types: (i) Chinese hamster ovary (CHO) cells (39), which are adherent epithelial cells; and (ii) U937 human promonocytes (40), which are non-adherent. The mechanical properties of these cell-types are relevant to their use in suspension cultures since CHO cells are used in large-scale bioreactors for the production of recombinant proteins (7, 12), and U937 cells are used to study differentiation along the monocyte-macrophage pathway (41, 42). To demonstrate the potential use of ED for the mechanical characterization of these two cell-types, we fit strain and relaxation data with two well-known models of visco-elastic mechanical properties.

2. Materials and methods

2.1. Cells and media

U937 cells were obtained from ATCC (Manassas, VA), and cultured in RPMI 1640 (Sigma, St. Louis, MO) supplemented with 10% fetal bovine serum (FBS; Atlanta Biologicals, GA). CHO-K1 cells were obtained from ATCC (Cat. No. CCL-61) and cultured in HAM-F12 (Sigma) supplemented with 10% FBS. Both cell types were incubated at 37°C, in an atmosphere supplemented with 5% CO₂. All cells used for ED were selected during the third and fourth weeks of culture, namely passage Nos. 8-12 for the U937 cells and Nos. 6-8 for CHO cells, to ensure they were healthy and proliferating normally.

The medium used for ED experiments (EDM) was an isotonic buffer with low electrical conductivity, $\kappa = 15$ mS/m, (EDM: 3.4 mM NaCl, 0.115 mM KH₂PO₄, 280 mM D-Glucose); pH was adjusted to 7.3 ± 0.1 with NaOH and the osmolality was 285 mOsm/kg. Low electrical conductivity was required to maximize ED stretching forces, as previously described by others (25-28). Cell-viability tests (“Live/Dead”, Invitrogen, Carlsbad, CA) showed no observable differences for either CHO or U937 cells, which were suspended in EDM for up to 30 minutes, compared with tests performed in media with roughly physiological κ (PBS, $\kappa \sim 1.5$ S/m). For ED experiments, exposure of cells to EDM was limited to 10 minutes. The use of low- κ media also reduces electrical conductivity-generated (“Joule”) heat, which scales with κ (see section 3.7 of (35)). In the present work, the maximum temperature increase of the suspension during ED was estimated to be less than 1 °C. Prior to ED experiments, cells were centrifuged at 190g for five minutes at moderate cell densities ($\sim 10^6$ cells/mL), and re-suspended in EDM at low densities ($\sim 1\text{-}5 \times 10^4$ cells/mL), as measured by hemocytometer. Low densities were used for ED in order to facilitate the capture of individual cells and to minimize undesirable effects arising from too many neighbouring cells. However, cell density could readily be increased depending on the required number at each electrode tip (see below: 10^4 cells/mL led to ~ 1 cell/tip). Cells suspended in EDM were deposited over the electrode surface in 5 μ L droplets (total cell number $\sim 50\text{-}250$).

2.2. Fabrication of electrodes and modeling of the electric field

To perform ED experiments during observation by optical microscopy, we micro-fabricated arrays of planar electrodes on standard microscope glass slides (figure 1). An electric potential, U , applied between opposing planar electrodes resulted in a “fringing” electric field, E (figure 1(a)), which penetrated into the cell-suspension dispensed in droplets over the surface (a droplet of suspension medium is represented by the circular area in figure 1(b)). The following electrode geometry was used to trap and deform cells: A set of triangularly-shaped outer electrodes (e1 in figures 1 and 2) surrounded a central ring-electrode (e2 in figures 1 and 2), which was driven at opposite polarity (see figure 1(b)). The triangular tips were rounded (radius of electrode curvature, $r_e = 12.5$ μ m), and their closest approach to the outer perimeter of the ring was 50 μ m (figure 2). A third electrode (e3 in figure 1) was not required for the present ED experiments and was, therefore, not connected to the signal generator.

Planar Ti/Pt electrodes were fabricated using standard lift-off processes, which we have described previously (43): Chromium masks were fabricated on glass (Bandwidth Foundry, Sydney, NSW, Australia) and photolithography was carried out by spin-coating an adhesion promoter, AP300 (Silicon Resources, Chandler, AZ), a lift-off resist LOR5A (MicroChem, Newton, MA) and a final, positive, resist S1813 (Shipley, now part of Rohm & Haas, Philadelphia, PA). UV exposure was done using a Karl Süss MA-4 mask aligner (Süss Microtec, Waterbury Center, VT). The electrodes were deposited by electron beam evaporation (Ti adhesion layer, 10 nm) and sputtering (Pt layer, 70 nm), the former under ultra-high-vacuum and the latter in Argon at 2.4 Pa. For each glass slide (dimensions: 76.2 x 25.4 x 1.5 mm), the lift-off procedure produced 12 sets of electrodes, each with three leads (figure 1(b)) to which electrical

connectors were bonded using a combination of conductive silver epoxy (MG Chemicals, Surrey, BC, Canada) and a standard two-phase epoxy (LePage, Toronto, ON, Canada).

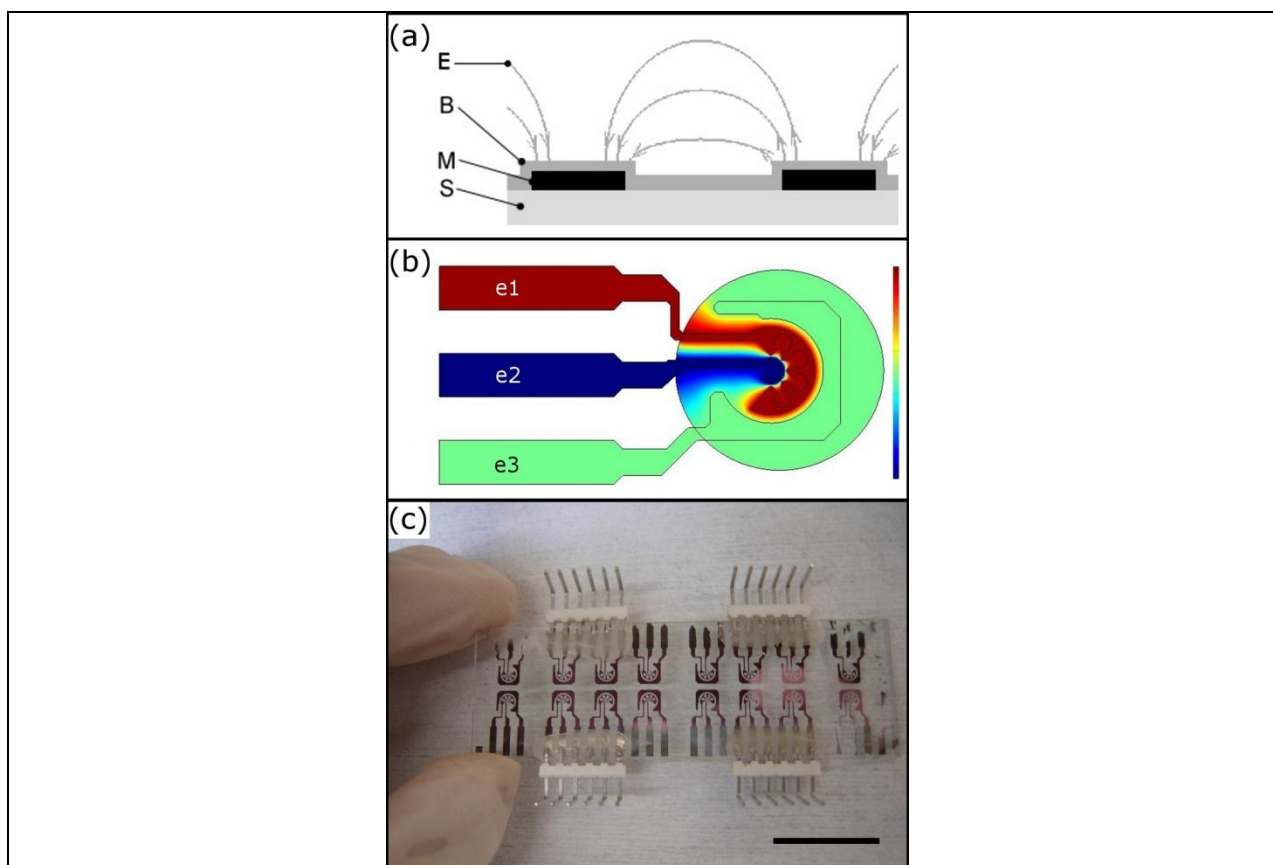


Figure 1. Micro-fabricated planar electrode array. (a) Illustration of the “fringing” electric field (E), insulating barrier (B), metallic conductors (M), and substrate (S) (dimensions are not to scale). (b) Geometry of the 3-electrode (e1, e2, and e3) configuration, with an applied electric potential of arbitrary magnitude (red = max, blue = min). (c) Array of electrodes on a glass microscope slide; scale bar is 2 cm.

Thin films (~ 550 nm) of hydrogenated silicon nitride ($\text{SiN}_x\text{:H}$, a clear, transparent dielectric) were deposited over the electrodes by plasma-enhanced chemical vapor deposition (PECVD), to prevent electrolysis of the suspension medium during ED, and to enable multiple reuses of the devices. For this, the slides were placed on the grounded electrode of a “Reinberg”-type parallel plate radio-frequency (RF, 13.56 MHz) PECVD reactor, in a flowing gaseous mixture of silane (SiH_4) and ammonia (NH_3): The flow-rates and partial pressures were (SiH_4 : 2.5 sccm, 12 mTorr) and (NH_3 : 25 sccm, 43 mTorr), and the total pressure was maintained at 55 mTorr. The power delivered to the plasma was 50 W (the power density at the surface of the grounded electrode was ~ 150 mW/cm²), and the substrate temperature was maintained at 125 °C. The deposition time was 45 minutes and film-thickness, measured by variable-angle spectroscopic ellipsometry (VASE, J. A. Woollam & Co., Lincoln, NE), was 550 ± 25 nm. We have previously described the operation of this PECVD system in more detail, albeit for the case of depositing thin films of a semi-conductor, nano-crystalline silicon (44).

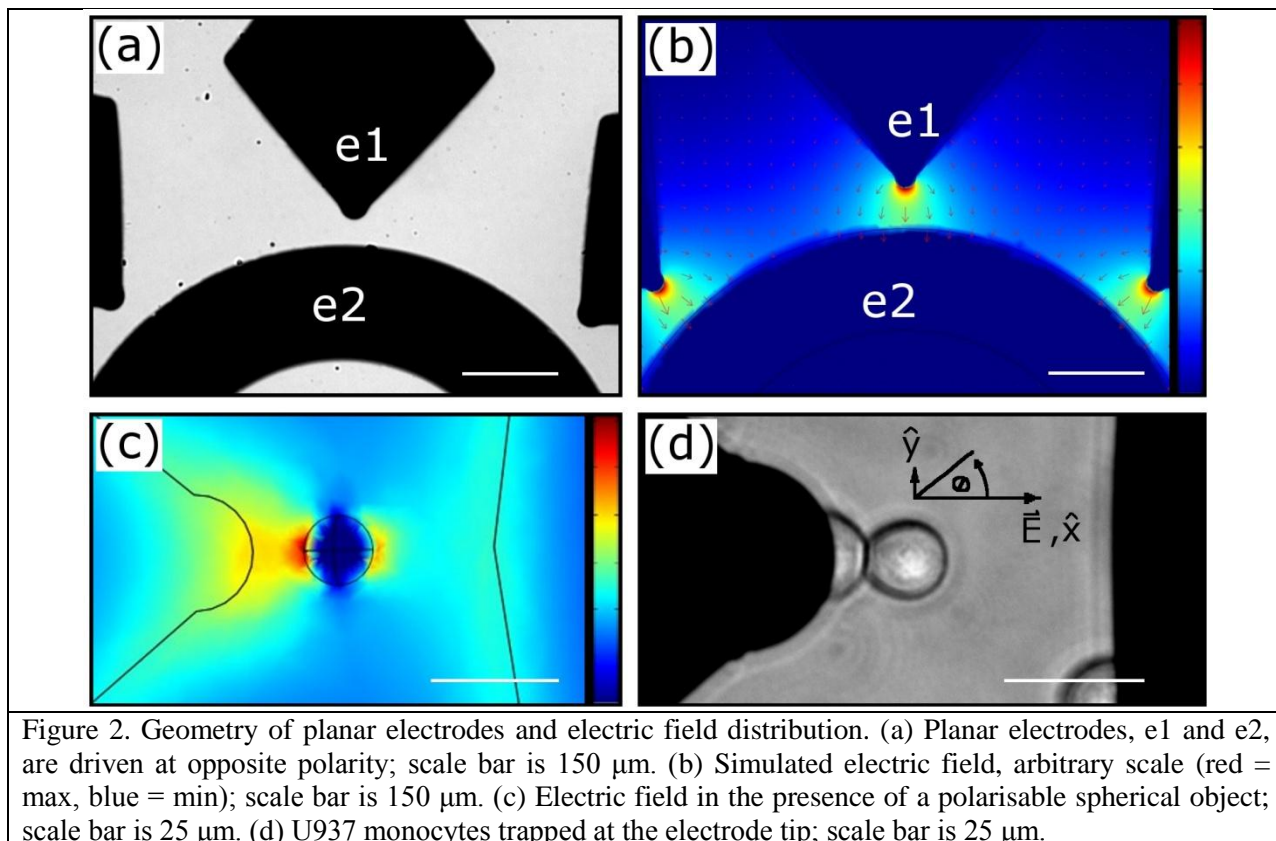
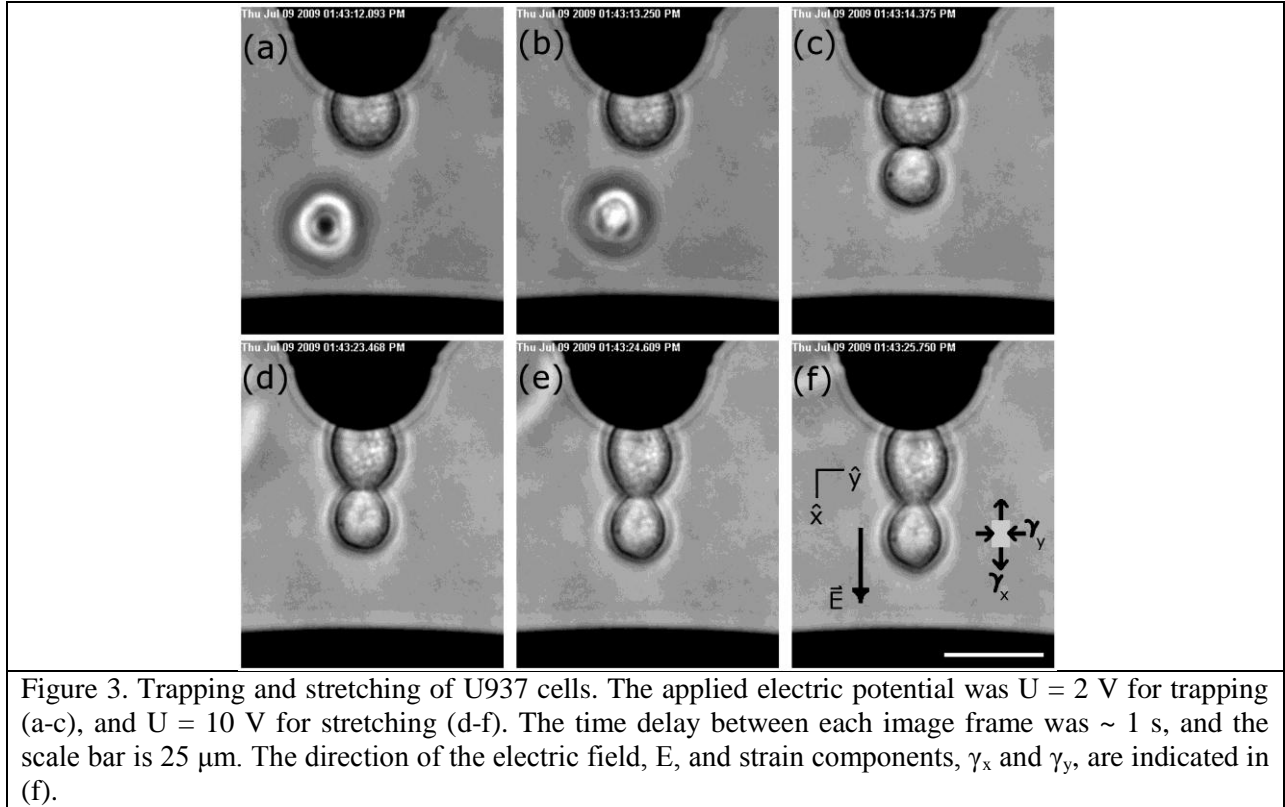


Figure 2. Geometry of planar electrodes and electric field distribution. (a) Planar electrodes, e1 and e2, are driven at opposite polarity; scale bar is 150 μm . (b) Simulated electric field, arbitrary scale (red = max, blue = min); scale bar is 150 μm . (c) Electric field in the presence of a polarisable spherical object; scale bar is 25 μm . (d) U937 monocytes trapped at the electrode tip; scale bar is 25 μm .

We simulated the electric field distribution using the “conductive media mode” in Comsol Multiphysics v3.2 software (Comsol, Stockholm, Sweden), with the electric potential assigned at boundaries (Dirichlet-type boundary conditions). The non-uniform E (figure 2(b)) was designed to capture individual cells at each electrode tip. In this region (figure 2(c)), values of E surrounding a polarized cell are high near the cell-poles and low near the equator. For the case of a uniform applied E , the radial component of the induced dipole field has an angular dependence that is proportional to $\cos\theta$ (45). In the present (non-uniform) case, E is highest near the cell-pole that faces the electrode tip (figure 2(c)), and cells are therefore trapped in this region (figure 2(d)).

2.3. Cell trapping and stretching protocol

Electrodes were placed within the slide-carrier of an inverted optical microscope (Zeiss, AxioVert S100TV) and connected to a signal generator (Agilent, 33220A). A sinusoidal electric potential, U , of frequency, $f = 5 \times 10^6$ Hz, was applied and the amplitude was modulated during ED: $U = 2$ V (peak-to-peak) was used to capture and hold cells (figure 3(a-c)), and $U = 10$ V (peak-to-peak) was used to deform cells at constant stress (figure 3(d-e)). The f -dependence of cell-polarization (see Appendix 1) can be approximated using well-known “single-shell” theories, which estimate the effective permittivity of the cell in terms of ϵ and κ for the cell-membrane and the internal cytosol (35, 36, 47). Three distinct f -regimes occur: (i) At low f ($f < \sim 10^5$ Hz, in the present cases), membrane charging by diffuse currents occurs and we observed “negative” DEP of cells; (ii) at intermediate f (10^6 Hz $< f < 10^7$ Hz), the cytosolic κ -term is dominant (compared with κ_m), and we observed “positive” DEP (and ED); at high f ($f > \sim 10^7$ Hz), similar ϵ -values of the cytosol and the suspension medium (both aqueous) resulted in negligible force. The three operating regimes outlined above have been previously described in detail by others (28), and we too have previously described the f -dependent DEP of U937 cells in various suspension media (43).



2.4. Strain measurement

Images were captured with a CCD camera (Model QIC-F/M2, QImaging, Burnaby, Canada) at a rate of approximately one frame per second, during ED experiments, and saved for subsequent analysis using commercial software (Northern Eclipse v.7, Empix Imaging, Mississauga, Canada). Measurements of cell dimensions were done manually, using the ellipse-fitting and measurement tools of the Graphic Image Manipulation Program (GIMP v.2). Strain in the directions parallel or perpendicular to E (γ_x and γ_y , respectively; see figure 3(f)) were both calculated as:

$$\gamma(t) = \frac{L(t) - L_0}{L_0}, \quad (1)$$

where $L(t)$ was the length of the cell at time, t , and L_0 was the original length. The apparent Poisson's ratio of the cell was then given by: $\nu = -\gamma_y/\gamma_x$. Mechanical behaviour of “simple” solids, for example viscoelasticity, involves the (*linear*) relationship between an applied stress, σ , and the resulting strain, γ ; the material-specific property linking the two is known as the solid's compliance, J (46):

$$\gamma = \sigma J \quad (2)$$

In other words, J is the strain per unit stress, and it is a measure of the solid's “stiffness”.

2.5. Calculation of the applied stress

To simplify data fitting, we derived an expression for the average value of uni-axial stress, σ , applied to a whole cell during a typical ED experiment. We estimated the magnitude of the total force acting on the cell, using the following well-known expression for the time-averaged DEP force (47):

$$\begin{aligned}\langle F_{DEP}(t) \rangle &= 2\pi r_c^3 K \varepsilon_m \nabla |E_{rms}|^2 \\ &= 4\pi r_c^3 K \varepsilon_m |E_{rms}| \nabla |E_{rms}|,\end{aligned}\quad (3)$$

where r_c is the cell radius, ε_m is the dielectric permittivity of the suspension medium, E_{rms} is the root-mean-squared value of E , and $K = \text{Re}\{K(f)\}$ is the real part of the dielectric polarisation (Clausius-Mosotti) factor of the cell (see Appendix 1). For trapped cells, we assumed $\pm \langle F_{DEP} \rangle / 2$ were the forces acting on each half-sphere, which stretched the cell approximately uni-axially. The actual distribution of E , and therefore of σ and F , was more complicated (figure 2(c)); the present simplifications are discussed in the Discussion section below.

Equation (3) can be written in one dimension as:

$$\langle F_{DEP}(x, t) \rangle_t = 4\pi r_c^3 K \varepsilon_m |E_{rms}(x)| \frac{d}{dx} |E_{rms}(x)|, \quad (4)$$

and the following approximation for $E(x)$ used:

$$\langle |E_{rms}(x)| \rangle = 0.7E_0, \quad (5a)$$

$$\langle \frac{d}{dx} |E_{rms}(x)| \rangle = n \frac{E_0}{r_c}, \quad (5b)$$

where $E_0 = U/d$ is the peak magnitude of the electric field, with U being the applied potential and $d = 50 \mu\text{m}$, the electrode gap; n is a geometry- and material property-dependent factor, and r_c is the cell radius. Good estimates of E_0 during ED are $E_0 = 4 \times 10^4 \text{ V/m}$ during trapping ($U = 2 \text{ V}$), and $E_0 = 2 \times 10^5 \text{ V/m}$ during stretching ($U = 10 \text{ V}$). The approximations in Eq. (5) result in the following expression for the force on each half-sphere:

$$F = \pm 2\pi r_c^2 n K \varepsilon_m E_0^2, \quad (6)$$

The average value of stress on the surface of the sphere can then be found by dividing Eq. (6) by the half-cell area:

$$\langle \sigma \rangle = n K \varepsilon_m E_0^2. \quad (7)$$

The non-uniformity of E_0 , near the tip of e1, was determined by FEM simulations and found to be of the same order of magnitude as that induced around a typical cell: $d/dx(E_0) \sim 1.5E_0/r_c$ ($n \sim 1.5$ in Eq. 5b). Assuming a maximum value of $K = 1$ (see Appendix 1), and $r_c = 7.0 \mu\text{m}$ (measured optically), Eq. (7) yields $\langle \sigma \rangle = 0.85 \text{ Pa}$ during trapping ($U = 2\text{V}$), and $\langle \sigma \rangle = 21.2 \text{ Pa}$ during stretching ($U = 10 \text{ V}$).

2.6. Viscoelastic properties

The simplest ‘‘lumped-parameter’’ visco-elastic model, which fits our data reasonably well, is the three-parameter standard linear solid (SLS) model, characterized by two elastic constants, k_1 and k_2 , and one viscous constant, η . In a well-known mechanical analog, the so-called Zener model, these correspond to a

parallel combination of a spring (k_1) with a series combination of a second spring (k_2) and a dashpot (η). The compliance function, $J(t)$, now describes the time-dependent response of the material to an applied time-varying σ , in terms of these model parameters. For the SLS, $J(t)$ is given by (48, 49):

$$J(t) = \frac{1}{k_1} \left[1 - \left(\frac{k_2}{k_1 + k_2} \right) e^{-t/\tau_\sigma} \right] \mathbf{1}(t), \quad (8)$$

where $\mathbf{1}(t)$ is the unit step function and τ_σ is the time-constant (or “relaxation time”) at constant stress:

$$\tau_\sigma = \eta \frac{(k_1 + k_2)}{k_1 k_2}. \quad (9)$$

In response to a step-wise (either increasing or decreasing) change in σ , the SLS model predicts (i) an instantaneous change in J , $J(t = 0) = J_0 = 1/(k_1 + k_2) = 1/E_0$, where E_0 is the initial elastic modulus; (ii) a limiting value of J , $J(t = \infty) = J_\infty = 1/k_1 = E_R$, where E_R is the relaxed elastic modulus; and (iii) a single time-constant, τ_σ , given by Eq. (9), which determines the relaxation time.

2.7. Power-law model

We also use a power-law to model $J(t)$, as was done previously by others for uni-axial stretching of single C2-7 cells, derived from skeletal muscle of adult CH3 mice (50):

$$J(t) = At^\alpha, \quad (10)$$

where A and α are constants. The power-law has been proposed as a general fitting procedure, which considers the cell to be a material with a continuum of relaxation times. The parameters, α and A , can be related to the low-frequency storage modulus, $G'(\omega)$, using the following equation (50):

$$G'(\omega) = \left(\frac{\cos(\alpha\pi/2)}{A\Gamma(1+\alpha)} \right) (2\pi f)^\alpha, \quad (11)$$

where Γ is the gamma function and f is the frequency.

2.8. Data fitting

Strain data were fit using Eq. (2) shown above, with the stress σ given by Eq. (7), and the material’s compliance function $J(t)$ given by either Eq. (8) or Eq. (10). The differences between measured and calculated values of γ were minimized using a non-linear least-squares algorithm (lsqnonlin, Matlab v. 7.2, The MathWorks, Natick, MA).

3. Results

3.1. Strain and relaxation of cells

Our ED protocol permitted time-dependent strain, $\gamma(t)$, measurement of individual cells, over several cycles of strain and relaxation (figures 4 and 5). CHO cells were observed to be stiffer than U937 cells,

and γ of the latter showed more significant long-term residual strain or plastic deformation than the former cells. Maximum values of γ for CHO cells were limited to ~ 0.2 (figure 4(c)) whereas, for a typical U937 cell, $\gamma > 0.5$ was observed after the third cycle (figure 5(c)). In some cases, contact with neighbouring cells imposed a limit on γ (indicated by “CL” in figure 5(c)).

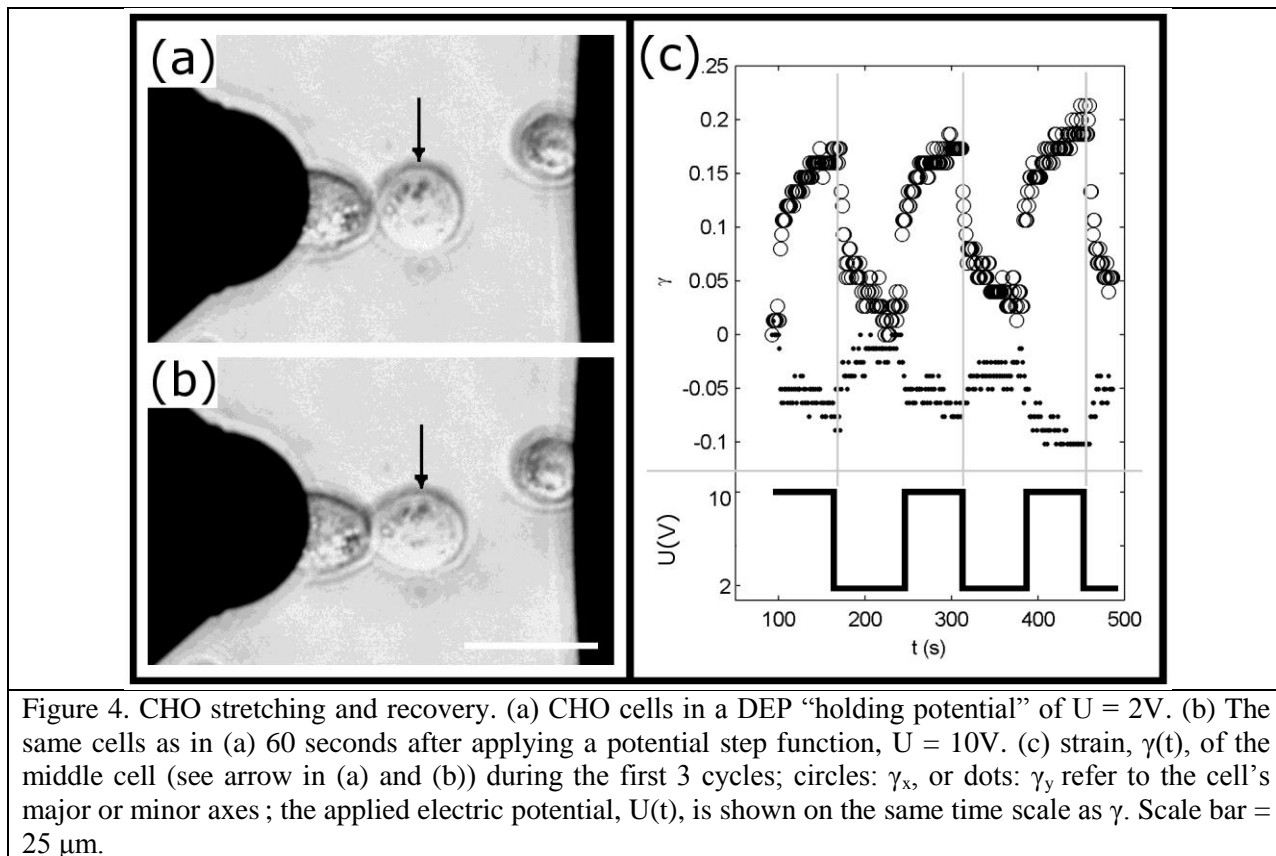


Figure 4. CHO stretching and recovery. (a) CHO cells in a DEP “holding potential” of $U = 2\text{V}$. (b) The same cells as in (a) 60 seconds after applying a potential step function, $U = 10\text{V}$. (c) strain, $\gamma(t)$, of the middle cell (see arrow in (a) and (b)) during the first 3 cycles; circles: γ_x , or dots: γ_y refer to the cell’s major or minor axes; the applied electric potential, $U(t)$, is shown on the same time scale as γ . Scale bar = $25\ \mu\text{m}$.

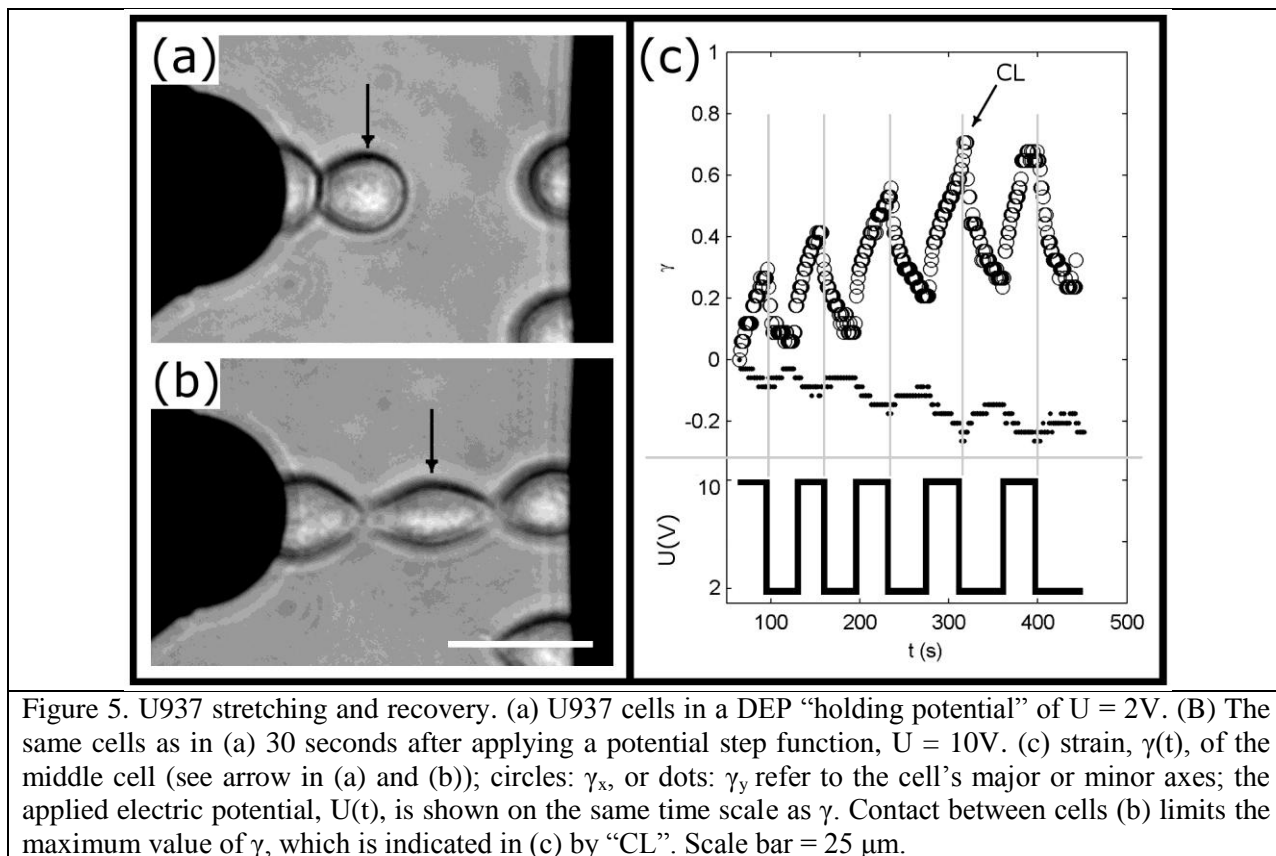


Figure 5. U937 stretching and recovery. (a) U937 cells in a DEP “holding potential” of $U = 2\text{V}$. (B) The same cells as in (a) 30 seconds after applying a potential step function, $U = 10\text{V}$. (c) strain, $\gamma(t)$, of the middle cell (see arrow in (a) and (b)); circles: γ_x , or dots: γ_y refer to the cell’s major or minor axes; the applied electric potential, $U(t)$, is shown on the same time scale as γ . Contact between cells (b) limits the maximum value of γ , which is indicated in (c) by “CL”. Scale bar = $25\ \mu\text{m}$.

3.2. Modeling of cell strain

Although contact between cells could limit the maximum strain in some cases (figure 5(c)), data were always taken from the first cycle of strain and relaxation of freely-deformable cells (figure 6), where strain was not limited by the presence of other cells. Both the SLS and PL models (Eqs. (8) and (10), respectively) were found to fit γ -data reasonably well (tables 1 and 2), although better fits were encountered for the case of CHO cells: Using the SLS model, the coefficients of determination values were $R^2 = 0.91$ and $R^2 = 0.95$ for U937 and CHO cells, respectively. Using the PL model, $R^2 = 0.91$ and $R^2 = 0.96$ for U937 and CHO cells, respectively.

3.3. Measured material properties

Deformations of CHO and U937 cells were rendered reasonably well by both the SLS and PL models, when the maximum value of strain was limited to $\gamma < \sim 0.2$ (figure 6). Long-term plastic deformation of U937 cells was observed for higher γ values (figure 5(c)), but the maximum applied stress ($\sigma \sim 20\ \text{Pa}$) was insufficient to induce comparable high strain in the case of CHO cells (figure 4(c)).

The three parameters of the SLS model (k_1 , k_2 , and η) can be related to the following material properties (51): $k_1 = E_R = 2(1 + \nu)G_R$, and $(k_1 + k_2) = E_0 = 2(1 + \nu)G_0$, where E_R is the relaxed elastic modulus, G_R is the relaxed shear modulus, E_0 is the initial elastic modulus, and G_0 is the initial shear modulus (51). Their numerical values are listed in table 3.

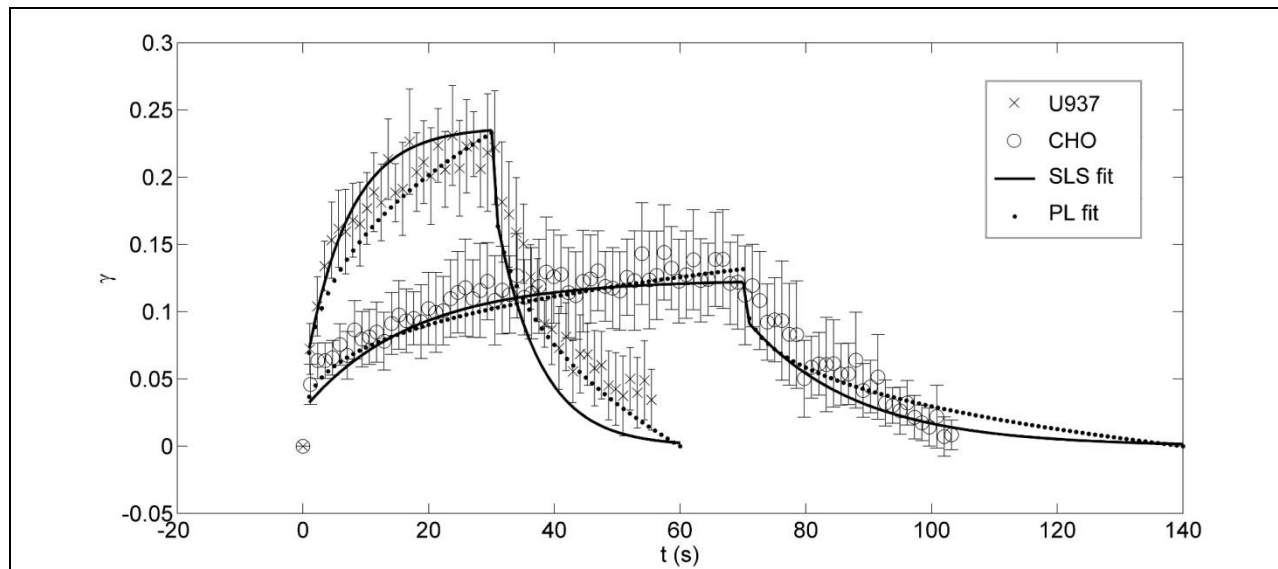


Figure 6. Strain and relaxation data from the first cycle for U937 and CHO cells, fit using the “standard linear solid” (SLS) or power-law (PL) models; fitting parameters are shown in tables 1 and 2, respectively. Data are mean \pm SE; N=10 for U937 cells and N=5 for CHO cells.

Table 1 Model parameters for the “standard linear (visco-elastic solid)” (SLS)

Cell type	k_1 (Pa)	k_2 (Pa)	η (Pa·s)	τ_σ (s) [*]	Reference
CHO	193 \pm 130	1379 \pm 930	2905 \pm 1958	17.2 \pm 11.6	Present work [†]
U937	99 \pm 44	798 \pm 353	608 \pm 269	6.2 \pm 2.8	Present work [†]
Neutrophil	27.5 \pm 12	73.7 \pm 35	13.0 \pm 5.4	0.65 \pm 0.3	19
Chondrocyte	~170	~180	~7500	~75	23

^{*}Relaxation time given by Eq. (9).

[†]All values from the present work are mean \pm SD (CHO: N = 5, U937: N = 10).

Table 2 Model parameters for the “power-law solid” (PL)

Cell type	α	A ($\times 10^{-3}$ Pa·s ^{-α})	G'(1 Hz) (Pa) [*]	Reference
CHO	0.301 \pm 0.20	3.7 \pm 2.49	466 \pm 314	Present work [†]
U937	0.356 \pm 0.11	7.0 \pm 3.10	262 \pm 116	Present work [†]
C2-7 Myoblast	0.24 \pm 0.01	2.4 \pm 0.3	~ 660	49

^{*}Low-frequency storage modulus, G'(ω), given by Eq. (11).

[†]All values from the present work are mean \pm SD (CHO: N = 5, U937: N = 10).

Table 3 Mechanical properties of cells derived using the SLS model

Cell type	ν^*	E_R (Pa)	G_R (Pa)	E_0 (Pa)	G_0 (Pa)
CHO	0.37 \pm 0.07	193 \pm 130	70.3 \pm 60.7	1572 \pm 1059	574 \pm 495
U937	0.39 \pm 0.14	99.4 \pm 44.0	35.8 \pm 28.7	898 \pm 397	323 \pm 259

^{*}Apparent Poisson’s ratio of the cell; all values are mean \pm SD (CHO: N = 5, U937: N = 10)

4. Discussion

4.1. Assessment of cell mechanical behaviour by ED and comparison with other techniques

The objective of this work was to use micro-fabricated planar (micro)-electrodes to generate (non-uniform) electric fields, E , of sufficient magnitude to induce substantial deformations to mechanically assess both CHO and U937 cells. These cell-deformations, observed by optical microscopy, enabled us to fit measured γ data with well-known SLS and PL models: Our results clearly demonstrate that ED may indeed be used to evaluate the biomechanical properties of individual (CHO and U937) cells in suspension; preliminary work with other cell-types (not shown here) further suggests that even broader applicability of ED is possible. The advantages of flexibility and modularity of micro-fabricated devices would further lend themselves to more widespread application of ED for mechanical assessment of cell behavior. Some advantages of ED over other techniques that have also been used, by other workers, for mechanical characterization of individual cells in suspension, are the following: (i) ED obviates the need for moving parts or for micro-beads in the cell suspension; (ii) mechanical contact between cells and device structures is minimized; (iii) planar electrodes for ED are easily micro-fabricated as arrays, which enables simultaneous measurements on several cells, and simple integration within biochips; and (iv) programmable ranges of U values enable the study of mechanical properties over multiple timescales.

4.2. Mechanical properties of CHO, U937 and other cell-types

CHO cells were found to be stiffer than U937 cells, and less easily deformed by electrical stresses during ED. The nearly two-fold higher elastic modulus of CHO cells compared with U937 cells (table 3) can be partly explained by differences of their cytoskeletons (work being reported in a separate study). To our knowledge, neither of these cell-types had previously been studied by ED, nor have their mechanical properties been estimated using either the SLS or PL models. It is therefore of interest to compare the present results with those of other workers, who did use these models with other cell-types and other measuring techniques. Comparison of the present data with those for neutrophil- or articular chondrocyte deformation, the latter two using the MPA technique, demonstrates a large range of biomechanical properties among the different cell-types: CHO and U937 cells both appear to be stiffer than neutrophils, but less stiff than suspended chondrocytes (table 1). The viscous constant, η , does not represent the cytosolic viscosity, but rather an “apparent” viscosity of the whole cell, so that high values reported here are not unexpected. The apparent Poisson’s ratio values for CHO and U937 cells were both less than 0.5 (table 3), suggesting that the cells are slightly compressible. As mentioned above, both SLS and PL models were found to fit our data reasonably well, but this agreement is not expected to hold generally; predictions based on these models tend to diverge for small γ values, and at shorter timescales than the ~ 1 s used in present work (50).

Our findings are consistent with previous reports, which suggest that healthy suspension cells are generally less stiff than anchorage-dependent ones (22, 29). Furthermore, higher E_R values have been reported for spread- than for spherical morphologies, for the cases of osteoblasts, chondrocytes, adipose-derived adult stem cells, and mesenchymal stem cells (24). We cite the morphology-dependent stiffness of cells in suspension, but we also acknowledge that E_0 and E_R values previously reported by others were found to increase as a function of seeding time for the case of superficial chondrocytes, but to decrease for that of chondrocytes taken from middle/deep cartilage layer depths (52). The above-described observations and the large statistical variances within the estimated mechanical properties for a given cell-type, reported both by the present and by other workers (see large SD values in tables 1 and 3), emphasise the need to refine methods for biomechanical characterization of cells on an individual basis.

Non-lethal (but physiologically significant) responses to hydrodynamic shear stresses have been reported for a variety of cell-types in suspension, when the stress was in the range of 1-10 Pa (9): Lethal values of stress for anchorage-dependent CHO-K1 cells were on the order of 1 Pa, but exceeded 200 Pa for suspension-cultured cells. In the present work, $\gamma \sim 0.1-0.3$ for suspended CHO and U937 cells rarely resulted in their rupture or lysis. Our calculated value of $\sigma \sim 20$ Pa is therefore in good agreement with previous measurements of non-lethal, physiologically-relevant mechanical stresses. We conclude that ED, although not capable (at least, in the present configuration) of generating maximum σ values comparable to their MPA-based counterparts (up to ~ 1 kPa (22, 23)), can nevertheless be used to study biomechanical properties of several mammalian cell-types in suspension.

4.3. Potential methodological improvements and future work

Reliable use of the ED technique requires experimental calibration of the forces and stresses generated. For example, cell-sized synthetic microspheres with well-characterized mechanical properties might be used as reference materials; some candidates that come to mind are commercially-available polystyrene or hollow silica microspheres. This type of measurement would increase the precision of estimating σ , which has been calculated analytically in the present work (Eq. (7) and Appendix 2).

ED requires the use of low- κ media to maximize σ , which depends on the differential polarizability of cells and media (Appendix 1). In the present experiments, this was accomplished by reducing salt concentrations to sub-physiological values. ED experiments were always performed for less than 10 minutes and the effects of low salt concentrations on U937 or CHO metabolism was not considered; future improvement of low- κ media for long-term culture of cells is expected to benefit DEP and ED methods.

In deriving our expression for σ (Eq. (7)), we simplified E by defining a normalized average value of electric field non-uniformity (Eq. (5b)) and assumed that σ was normal to the cell-surface. It is also worth noting that Eq. 7 results in an expression for γ (Eq. (2)), which is similar to the following expression reported previously by others for the case of ED (28, 38):

$$\gamma = CKE^2, \quad (12)$$

where C accounts for cell compliance, and is related to J in our model by: $C = n\epsilon_m J$. Electrically-induced stresses of comparable magnitude to those estimated using Eq. (7) can exist at the cell/medium interface, even if E is initially uniform (see Appendix 2). Although theoretical work has been developed by others to explain deformation of liquid drops in (initially uniform) E-fields (58), further work seems appropriate to clearly identify all sources of electrical stresses in the case of complex dielectric objects such as cells.

More realistic modelling of cell mechanics is also required: Although the SLS and PL models were useful for rapid characterization of the investigated cell-types, we must acknowledge that they oversimplify cell structure. Finite-element modelling (FEM) can potentially alleviate some of these problems, since more realistic cell- and electrode geometries can be simulated within dynamic environments (17, 53). Although we have used FEM to simulate the distribution of E, in the future we also plan to use FEM to study the distribution of σ and to model cell deformation dynamically.

The maximum average σ values, applied to cells by ED, were calculated to be $\sigma \sim 20$ Pa, using the maximum available U (10 V peak-to-peak, into a 50 Ω load at 5 MHz). It would be relatively simple to increase these values, because σ scales with the square of U (Eq. (7)), and the true limits to σ are therefore presently unknown. Threshold values of σ required to stretch cells have been reported in the range of 10 Pa to 100 Pa (20, 21), and increasing U while maintaining small inter-electrode distances (50 μm in the present case) would therefore increase the number of cell-types and synthetic materials which could be studied by ED.



Figure 7. Planar electrode array micro-fabricated on a transparent insulating (flexible) polymer substrate.

Our ED devices were micro-fabricated directly on microscope slides to permit observation by optical microscopy during ED; improved imaging methods can therefore be used to study the mechanics of sub-cellular structures such as the cytoskeleton. It may also be possible to include imaging arrays directly in an ED device for increased portability. So-called “cell-on-chip” micro-fluidic devices, which permit multimodal analysis and manipulation of cells (54, 55), can be readily made to incorporate micro-electrodes for ED-based mechanical measurements. Using the “low-temperature” micro-fabrication methods described here, we have fabricated ED test-devices on transparent plastic (polymer) substrates (figure 7), but in order to resist the 125 °C substrate temperature during PECVD (see above), clear polymers with high glass-transition temperatures are required, for example cyclic polyolefin or poly(sulfone) (44). Based on the above, we therefore expect diverse future implementations of the methods we have described in this article.

5. Conclusions

Electrical stresses, generated by planar microelectrodes with relatively low values of applied potential ($U < 10$ V), have been used to electro-deform CHO and U937 cells in suspension. Our electrode geometry and ED methodology have permitted biomechanical characterizations of individual cells of both these cell-types. Electrode structures required for novel ED implementations can readily be micro-fabricated and included within micro-fluidic devices, for increased automation of measurements in computer-controlled biochips. The results presented here therefore suggest that ED should become an increasingly-favoured technique for biomechanical measurements.

Acknowledgements

This work was supported by the Natural Sciences and Engineering Research Council of Canada (NSERC), and by the Canadian Institutes of Health Research (CIHR). The authors thank the staff of the Micro-fabrication Laboratories (LMF) for their help and expertise, in particular Dr. Souleymane Bah for his assistance with photolithography and fabrication of electrodes.

Appendix 1: The Clausius-Mosotti factor

The complex Clausius-Mosotti factor of a (“spherical”) cell driven at a frequency, f , is given by:

$$K(f) = \frac{\varepsilon_c^* - \varepsilon_m^*}{\varepsilon_c^* + 2\varepsilon_m^*}, \quad (\text{A.1})$$

where $\varepsilon^* = \varepsilon - i(\kappa/2\pi f)$ is the complex permittivity, ε is the dielectric permittivity, κ is the electrical conductivity, $i = \sqrt{-1}$, and the subscripts, c and m , refer to the cell and medium, respectively. Values of K are bounded by $-0.5 < K < 1$, and are maximized ($K > 0$) for ED experiments, by appropriate choice of f and κ . We selected $f = 5 \times 10^6$ Hz and $\kappa = 15$ mS/m to assure “positive” DEP forces ($K > 0$), which can be calculated in the quasi-electrostatic regime (25, 27, 32). We have previously described the f -dependence of K for U937 cells (43).

Appendix 2: The Maxwell-stress on a dielectric sphere in a uniform applied electric field

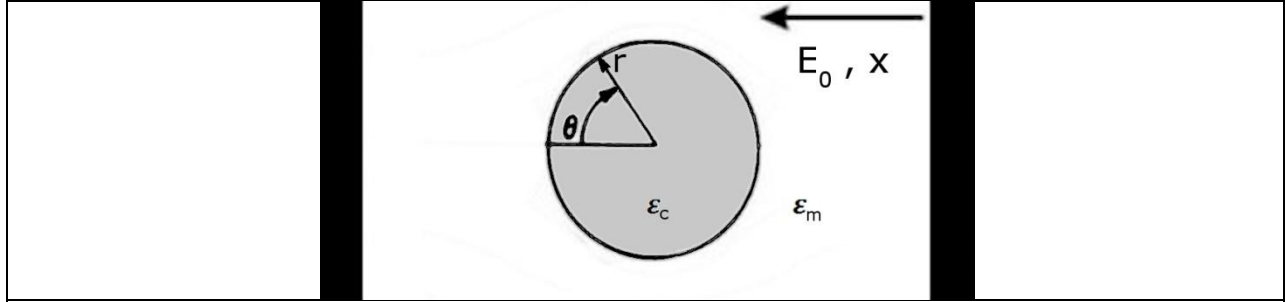


Figure A1. Cross-section of an ideal sphere between two planar electrodes; the arrow points in the positive x-direction (in the direction of the applied electric field, E_0).

A dielectric sphere of radius, r_c , and dielectric permittivity, ϵ_c , is placed within a medium with dielectric permittivity, ϵ_m , and a uniform electric field, E_0 , is applied in the positive x-direction (figure A1). Using polar coordinates, (r, θ) , with $r = 0$ at the center and $r = r_c$ at the surface, the electric fields induced inside, \mathbf{E}_{in} , and outside, \mathbf{E}_{out} , the sphere can be obtained by solving Laplace's equation. They are found to be (56, 57):

$$\mathbf{E}_{in} = \frac{3\epsilon_m}{\epsilon_c + 2\epsilon_m} E_0 (\cos\theta \hat{r} - \sin\theta \hat{\theta}), \quad (\text{A.2})$$

$$\mathbf{E}_{out} = E_0 (\cos\theta \hat{r} - \sin\theta \hat{\theta}) + \frac{\epsilon_c - \epsilon_m}{\epsilon_c + 2\epsilon_m} \frac{r_c^3}{r^3} E_0 (2\cos\theta \hat{r} + \sin\theta \hat{\theta}) \quad (\text{A.3})$$

Equations (A.2) and (A.3) apply when the driving potential is sinusoidal, with the dielectric permittivities, ϵ_c and ϵ_m , replaced by their respective complex permittivities, ϵ_c^* and ϵ_m^* . We define the factors: $K_1 = 3\epsilon_m/(\epsilon_c + 2\epsilon_m)$ and $K_2 = (\epsilon_c - \epsilon_m)/(\epsilon_c + 2\epsilon_m)$, where $K_1 + K_2 = 1$; values of K_1 and K_2 are bounded by $0 < K_1 < 1.5$, and $-0.5 < K_2 < 1$, respectively. The radial components of the electric fields can then be written as:

$$\mathbf{E}_{in} \cdot \mathbf{n} = K_1 E_r = (1 - K_2) E_r, \quad (\text{A.4})$$

$$\mathbf{E}_{out} \cdot \mathbf{n} = (1 + 2K_2) E_r, \quad (\text{A.5})$$

where \mathbf{n} is the local outer normal, and $E_r = E_0 \cos\theta$.

The net Maxwell-stress, σ^M , at a sharp boundary has the normal and tangential components (58):

$$[\sigma^M \cdot \mathbf{n}] \cdot \mathbf{n} = \frac{1}{2} \|\epsilon(\mathbf{E} \cdot \mathbf{n})^2 - \epsilon(\mathbf{E} \cdot \mathbf{t}_1)^2 - \epsilon(\mathbf{E} \cdot \mathbf{t}_2)^2\|$$

$$[\sigma^M \cdot \mathbf{n}] \cdot \mathbf{t}_i = \sigma_u \mathbf{E} \cdot \mathbf{t}_i, \quad (\text{A.6})$$

where $\|(\cdot)\|$ denotes the jump, "outside-inside", of (\cdot) across the boundary, \mathbf{t}_i represents either of two orthogonal tangent vectors embedded in the surface, and σ_u is the free surface charge per unit area.

In the intermediate frequency regime (described in section 2.3), cells have high effective conductivities and the tangential components of \mathbf{E} in Eq. (A.6) become negligible, owing to reduced charge accumulation at the interface (58). Using Eqs. (A.4 and A.5) in Eq. (A.6), the normal component of Eq. (A.6) is then given by:

$$\sigma^M \cdot n = \frac{\varepsilon_m}{2} (1 + 4K_2 + 4K_2^2)(E_0 \cos\theta)^2 - \frac{\varepsilon_c}{2} (1 - 2K_2 + K_2^2)(E_0 \cos\theta)^2, \quad (\text{A.7})$$

which, for $K_2 \sim 1$, reduces further to:

$$\sigma^M \cdot n \sim \frac{9}{2} \varepsilon_m (E_0 \cos\theta)^2. \quad (\text{A.8})$$

The stress given by Eq. (A.8) has a maximum value of $\sigma^M \sim 127$ Pa at the cell's poles, and it is zero at the equator. For a sinusoidal (time-varying) applied potential, E_0 is replaced by the rms-value of $\sim 0.7E_0$ in Eq. (A.8), and the resulting maximum stress is reduced to $\sigma^M \sim 63$ Pa. The Maxwell-stress at the cell-surface, therefore, varies with $\cos^2\theta$, pulling the cell in opposite directions at its poles, and deformation can occur even if the initial E was uniform and the net force is zero.

References

- [1] Worthen G S, Schwab B, Elson E L, Downey G P 1989 Mechanics of stimulated neutrofiles: cell stiffening induces retension in capillaries *Science* **14** 183-186
- [2] Redenbach D M, English D, Hogg J C 1997 The nature of leukocyte shape changes in the pulmonary capillaries *Am. J. Physiol. Lung Cell. Mol. Physiol.* **273** L733-L740
- [3] Rosenbluth M J, Lam W A, Fletcher D A 2006 Force microscopy of nonadherent cells: A comparison of leukocyte cell deformability *Biophys. J.* **90** 2994-3003
- [4] Fung Y C 1993 *Biomechanics: Mechanical Properties of Living Tissues*, 2nd edition (New York: Springer-Verlag)
- [5] Suresh S 2007 Biomechanics and biophysics of cancer cells *Acta Biomaterialia* **3** 413-438
- [6] Ozturk S S 2006 *Cell culture technology for pharmaceutical and cell-based therapies*, ed S S Ozturk and W-S Hu (New York: Taylor & Francis) chapter 1
- [7] Jayapal K P, Wlaschin K F, Yap M G S, Hu W-S 2007 Recombinant protein therapeutics from CHO cells - 20 years and counting *Chem. Eng. Prog* **103** 40-47
- [8] Hammond T G, Hammond J M 2001 Optimized suspension culture: the rotating-wall vessel. *Am. J. Physiol. Renal Physiol* **281** F12-F25
- [9] Ma N, Koelling K W, Chalmers J J 2002 Fabrication and use of a transient contractional flow device to quantify the sensitivity of mammalian and insect cells to hydrodynamic forces *Biotechnol. Bioeng.* **80** 428-437
- [10] Senger R S, Karim M N 2003 Effect of shear stress on intrinsic CHO culture state and glycosylation of recombinant tissue-type plasminogen activator protein *Biotechnol. Prog.* **19** 1199-1209
- [11] Ma N, Mollet M, Chalmers J J 2006 *Cell culture technology for pharmaceutical and cell-based therapies*, ed S S Ozturk and W-S. Hu (New York: Taylor & Francis) p237
- [12] Keane J T, Ryan D, Gray P P 2002 Effect of shear stress on expression of recombinant protein by Chinese hamster ovary cells *Bioengineering* **81** 211-220
- [13] Gigout A, Buschmann M D, Jolicoeur M 2009 Chondrocytes cultured in stirred suspension with serum-free medium containing pluronic-68 aggregate and proliferate while maintaining their differentiated phenotype *Tissue Eng.: Part A* **15** 2237-2248
- [14] Svoboda K, Block S M 1994 Biological applications of optical forces *Annu. Rev. Biophys. Biomol. Struct.* **23** 247-285
- [15] Ashkin A 1997 Optical trapping and manipulation of neutral particles using lasers *Proc. Natl. Acad. Sci. USA* **94** 4853-4860

- [16] Guck J, Ananthakrishnan R, Mahmoodi H, Moon T J, Cunningham C C, Käs J 2001 The optical stretcher: A novel laser tool to micromanipulate cells *Biophys. J.* **81** 767-784
- [17] Ananthakrishnan R, Guck J, Wottawah F, Schinkinger S, Lincoln B, Romeyke M, Moon T, Käs J 2006 Quantifying the contribution of actin networks to the elastic strength of fibroblasts *J. Theor. Biol.* **242** 502-516
- [18] Suresh S 2007 Biomechanics and biophysics of cancer cells *Acta Biomaterialia* **3** 413-438.
- [19] Schmid-Schoenbein G W, Sung K-L P, Toezere H 1981 Passive mechanical properties of human leukocytes *Biophys. J.* **36** 243-256
- [20] Sung K-L P, Dong C, Schmid-Schoenbein G W, Chien S, Shalak R 1988 Leukocyte relaxation properties *Biophys. J.* **54** 331-336
- [21] Evans E, Yeung A 1989 Apparent viscosity and cortical tension of blood granulocytes determined by micropipet aspiration *Biophys. J.* **56** 151-160
- [22] Hochmuth R M 2000 Micropipette aspiration of living cells *J. Biomech.* **33** 15-22
- [23] Guilak F, Erickson G R, Ping Ting-Beall H 2002 The effects of osmotic stress on the viscoelastic and physical properties of articular chondrocytes *Biophys. J.* **82** 720-727
- [24] Darling E M, Topel M, Zauscher S, Vail T P, Guilak F 2008 Viscoelastic properties of human mesenchymally-derived stem cells, primary osteoblasts, chondrocytes, and adipocytes *J. Biomech.* **41** 454-464
- [25] Engelhardt H, Sackmann E 1988 On the measurement of shear elastic moduli and viscosities of erythrocyte plasma membranes by transient deformation in high frequency electric fields *Biophys. J.* **54** 495-508
- [26] Pawlowski P, Fikus M 1989 Bioelectrorheological model of the cell. 1. Analysis of stresses and deformations *J. Theor. Biol.* **137** 321-337
- [27] Krueger M, Thom F 1997 Deformability and stability of erythrocytes in high-frequency electric fields down to subzero temperatures *Biophys. J.* **73** 2653-2666
- [28] Sukhorukov V, Zimmermann U 1998 The effect of electrical deformation forces on the electropermeabilization of erythrocyte membranes in low- and high-conductivity media *J. Membrane Biol.* **163** 235-245
- [29] Lim C T, Zhou E H, Quek S T 2006 Mechanical models for living cells – a review *J. Biomech.* **39** 195-216
- [30] Kononenko V L, Shimkus J K 2000 Stationary deformations of erythrocytes by high-frequency electric field *Bioelectrochemistry* **52** 187-96
- [31] Thom F 2009 Mechanical properties of the human red blood cell membrane at -15 °C *Cryobiology* **59** 24-27
- [32] Pohl H A 1978 *Dielectrophoresis* (Cambridge: Cambridge University Press)

- [33] Fuhr G, Zimmermann U, Shirley S G 1996 *Electromanipulation of Cells*, ed U Zimmermann and G A Neil (Boca Raton: CRC press) chapter 5
- [34] Friend A W, Finch E D, Schwan H P 1975 Low-frequency electric-field induced changes in shape and motility of amoebas *Science* **187** 357–359
- [35] Hughes M P 2002 *Nanoelectromechanics in Engineering and Biology* (Boca Raton: CRC Press)
- [36] Morgan H and Green N G 2003 *AC Electrokinetics: Colloids and Nanoparticles* (Baldock: Research Studies Press)
- [37] Voldman J 2006 Electrical forces for microscale cell manipulation *Annu. Rev. Biomed. Eng.* **8** 425-454
- [38] Wong P K, Tan W, Ho C-M 2005 Cell relaxation after electrodeformation: effect of latrunculin A on cytoskeletal actin *J. Biomech.* **38** 529-535
- [39] Puck T, Cieciura S, Robinson A 1958 Genetics of somatic mammalian cells III: Long-term cultivation of euploid cells from human and animal subjects *J. Exp. Med.* **108** 945-956
- [40] Sundstrom C, Nilsson K 1976 Establishment and characterization of a human histiocytic lymphoma cell line (U-937) *Int. J. Cancer* **17** 565-577.
- [41] Bertram C, von Neuhoff N, Skawran B, Steinemann D, Schlegelberger B, Hass R 2008 The differentiation/retrodifferentiation program of human U937 leukemia cells is accompanied by changes of VCP/p97 *BMC Cell Biol.* **9:12**
- [42] Girard-Lauriault P-L, Truica-Marasescu F, Petit A, Wang H T, Desjardins P, Antoniou J, Mwale F, Wertheimer M R 2009 Adhesion of Human U937 Monocytes to Nitrogen-rich Organic Films: Novel Insights into the Mechanism of Cellular Adhesion *Macromol. Biosci.* **9** 911-921
- [43] MacQueen L A, Buschmann M D, Wertheimer M R 2008 Gene delivery by electroproation after dielectrophoretic positioning of cells in a non-uniform electric field *Bioelectrochemistry* **72** 141–148
- [44] MacQueen L A, Zikovsky J, Dennler G, Latreche M, Czeremuszkina G, Wertheimer M R 2006 PECVD of nanocrystalline Si layers on high-T_g polymer substrates *Plasma Processes and Polymers* **3** 58-65
- [45] Jackson J D 1999 *Classical Electrodynamics*, 3rd edition (New York: John Wiley and Sons)
- [46] Ferry J D 1980 *Viscoelastic Properties of Polymers*, 3rd edition (New York: John Wiley and Sons)
- [47] Jones T B 1995 *Electromechanics of Particles* (Cambridge: Cambridge University Press) section 2.4(C), equation 2.46
- [48] Schmid-Schoenbein et al. 1981 equation 12
- [49] Fung Y C 1993 section 2.11, equation 12

- [50] Desprat N, Richert A, Simeon J, Asnacios A 2005 Creep function of a single living cell *Biophys. J.* **88** 2224-2233
- [51] Fung Y C 1993 section 2.11, equation 8
- [52] Shieh A C, Athanasiou K A 2006 Biomechanics of single zonal chondrocytes *J. Biomech.* **39** 1595-1602
- [53] Liu Y, Liu W-K, Belytschko T, Patankar N, To A-C, Kopacz A, Chung J-H 2007 Immersed electrokinetic finite element method *Int. J. Numer. Meth. Engng.* **71** 379-405
- [54] El-Alil J, Sorger P K, Jensen K F 2006 Cells on chips *Nature* **442** 403-411
- [55] Sims C E, Allbritton N L 2007 *Lab Chip* **7** 423-440
- [56] Stratton J A 1941 *Electromagnetic Theory* (New York: McGraw-Hill) section 3.4
- [57] Grodzinsky A J *Fields Forces and Flows in Biological Tissues and Membranes*, Massachusetts Institute of Technology Course Notes: BE.430J, section 4.4
- [58] Saville D A 1997 ELECTROHYDRODYNAMICS: The Taylor-Melcher Leaky Dielectric Model *Annu. Rev. Fluid Mech.* **29** 27-64